A Theoretical and Numerical Procedure for Predicting Sailing Yacht Lift and Drag

by

Claudio Cairoli

M.S., University of Virginia, 2000
M.S., Massachusetts Institute of Technology, 2002

Submitted to the Department of Mechanical Engineering
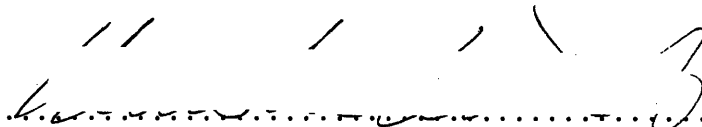in partial fulfillment of the requirements for the degree of

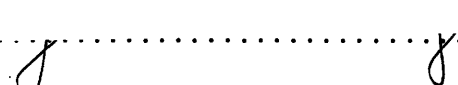Doctor of Philosophy in Naval Architecture and Marine Engineering
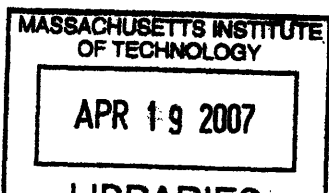
at the

MASSACHUSETTS INSTITUTE OF TECHNOLOGY

February 2007

Author . . . .
Department of Mechanical Engineering
January 10, 2007

Certified by . . . .
Jerome H. Milgram
Professor of Ocean and Mechanical Engineering
Thesis Supervisor

Accepted by . . . .
Lallit Anand
Chairman, Department Committee on Graduate Students

A Theoretical and Numerical Procedure for Predicting Sailing Yacht Lift and Drag

by

Claudio Cairoli

Submitted to the Department of Mechanical Engineering
on January 10, 2007, in partial fulfillment of the
requirements for the degree of
Doctor of Philosophy in Naval Architecture and Marine Engineering

Abstract

In this thesis, a theoretical and numerical procedure for predicting the effects of viscosity on the hydrodynamic forces developed by a sailing yacht hull is presented. A simultaneous viscous/inviscid algorithm is developed by coupling a low order panel method with quasi three-dimensional integral boundary layer equations. A transom condition is used to prevent non-zero wave heights at the stern for a hull with overhangs. The influence of viscosity on the outer inviscid flow is modeled using a wall transpiration boundary condition and an edge velocity formula. The boundary layer edge velocity is expressed as a sum of the inviscid velocities and a correction dependent only on the boundary layer variables, determined by equations developed from the panel method calculation as a distribution of transpiration sources. These are superimposed on the body, including the lifting surfaces, as well as on the potential flow wakes. The boundary layer equations, with the global potential flow effects included via the transpiration source model, are solved by a full Newton's method. Numerical predictions for a sailing yacht hull are compared with experimental results obtained in a towing tank.

Thesis Supervisor: Jerome H. Milgram
Title: Professor of Ocean and Mechanical Engineering

Acknowledgments

This is the end of a very long journey for me, much longer than the four and half years it took me to earn my Doctorate. It started about twenty-five and half years ago when I first set foot in elementary school, I have been a student uninterruptedly since then. As in most long journeys, I met a lot of people along the way that helped me, supported me, befriended me, so I have a lot of people to thank, more than I can thank here.

I would like to start by thanking all the teachers that I had from elementary school through high school, to college. Each one of them contributed with their teachings to make me become who I am today. Of all of them I would like to mention a couple: Prof. Dario Pavesi, my high school math teacher, for giving me my first failing grade in math (Prof. Pavesi, I hope you'll be happy to know it is still the only one I ever got) and for always challenging me beyond what was required. Prof. Antonio Silva, my high school principal, put the bug in me about going to study in the US. I didn't take that chance then, but I surely didn't miss it when it present itself again in college.

In more recent times and in particular in relation to this work, my thank yous go to Prof. Mark Drela for all of his help with the viscous part of the code, for providing me with some of the fundamentals routines and for sitting down with me when I had a problem; and to Prof. Paul Sclavounos for making available to me the source code to SWAN, for acting as my academic advisor during Jerry's sabbatical, and for helping with the inviscid part of the code. Last, but certainly not the least, is my advisor Prof. Jerome Milgram. Jerry has been a great pleasure to work with, always with my best interest in mind, he made my stay at MIT a great experience. He never asked the unreasonable which meant I could still have a social life outside of MIT. Thanks to him I had the opportunity to do some of the best sailing in my life and to participate in exciting projects outside of MIT. He was always available whenever I had a problem and always went out of his way to help me solve it. I am very much looking forward to teaching the sailing yacht design course with him next semester, and I hope I will get the chance to keep working with him, even after I leave MIT.

My friends have also been a great support system and played a very important role in keeping me from going insane over the last couple of months by patiently listening to all my complaints, problems and worries and contrasting my usual pessimistic view of things with their much more optimistic one. So thank you Cleo, Jackie, Gabe, Sue, Sharon, Benedetta, Christian, Steven, Christy and all the others.

None of this could have happened without my family: my sister and my parents. My sister is finishing a doctorate in chemistry in Italy, so she was the one that at times could offer the best support and advise since she was going through the same thing. She was always my biggest fan, as I am of her, together with my parents. I am very thankful to my mom and my dad, not only for the material help that they gave me throughout my scholastic career, but because they never stopped believing in me, and when I was ready to quit they kept encouraging me. It's only because of them that I was able to end this endeavour successfully. I hope this result makes them as happy as it makes me.

Contents

List of Figures

11

List of Tables

Chapter 1

Introduction

"Olin J. Stephens II is considered by most to be the greatest yacht designer of this century, perhaps ever. Since 1929, yachts shaped by this humble, even shy, man have written the creative and competitive history of the sport, and defined excellence in the profession of naval architecture. Olin's record of six victories in the America's Cup: Ranger in 1937, which he co-designed with Starling Burgess; Columbia in 58; Constellation, 64; Intrepid, 67; Courageous, 74 and Freedom, 80, is unlikely ever to be met, and his roster of ocean racers yields a list of legends - yachts such as Dorade, Stormy Weather, Edlu, Finisterre, Bolero, Bay Bea, Running Tide, Dora IV (aka Tenacious), two Kialoas, four Dynas, four Palawans and four Morning Clouds."

This is how the New York Yacht Club [4] describes "Mr. America's Cup" Olin Stephens. When he was recently asked what the most important advance in yacht design was during his lifetime, he answered the Velocity Prediction Program (VPP) because "that is yacht design by the numbers".

1.1   Thesis Objective

Velocity prediction programs are the foundations of several handicapping racing rating systems, such as the International Measurement System (IMS) or the newly devel-

oped Offshore Racing Rule (ORR). While in the latter the details of the VPP are kept secret, the formulation of the former is public, and in particular the hydrodynamic models are published in [3]. The hydrodynamic forces are modeled using regression formulae based on characteristic parameters of the hull and appendages. Yacht designers quickly figured out how to beat the rule, how to design so that their hull shape was rated slow by the VPP, when in fact it is faster. A first attempt to curb this trend was implemented by the Offshore Racing Association (ORA), the governing body for the ORR, by keeping the details of the formulations inside the VPP hidden. However, this has partly failed too, as designers started to submit systematic variations of a design to find the sensitivity of the hydrodynamic force models to the different parameters.

All of these problems would be greatly mitigated by using actual flow simulations instead of regression models for the computation of the hydrodynamic forces as this would provide the real performance. It is believed that if it were possible to evaluate the performance of a hull shape based on an actual flow simulation, it would be a lot harder for designers to "beat" the rule and the handicapping system would become more fair.

The objective of this thesis is the initial development of a theoretical and numerical method for the computation of the complete hydrodynamic forces on a sailing yacht hull that could ultimately constitute the basis for a simulation-based velocity prediction program. To achieve this objective is necessary that the method of choice is capable of computing not only the pressure resistance but also the viscous resistance and their interactions.

1.2 Research History

Potential flow methods based on panel methods have been used in ship hydrodynamics for three decades now. The application to the solution of a ship wave problem was first introduced in the late 1970's by Gadd [8] and Dawson [5], who proposed to

cover also part of the free surface with Rankine-source panels and to apply linearized free-surface boundary conditions on panels on the free surface itself.

Since these two pioneering works, many different panel-method based, free surface flow solvers have been developed over the years. Raven, at the Maritime Research Institute of Netherlands, first developed DAWSON, a linear free-surface solver, which he then turned into RAPID [24], a nonlinear solver based on a raised panel method. RAPID was extended to be able to compute lifting flows by adding a sheet of dipole on the camber plane of the appendages [14]. This solution proved to be not very accurate in the computation of lift. Also, to include the effects of viscosity, Raven switched from a boundary element panel method to a volume method by going to a RANS solver [31]. The reason to use a RANS solver may have been dictated by the fact that he was investigating mostly ship hull forms, which have blunt stern with significant flow separation.

Sclavounos and Nakos [29] presented in 1988 an analysis of the propagation of gravity waves using a Rankine panel method. This work led to the development of a frequency domain formulation for ship motions with a consistent linearization that uses the double-body flow model as the base flow [17]. This solver, known as Ship Wave ANalysis or SWAN, was then converted from the frequency domain to the time domain by Kring [13]. Mantzaris added the capability of computing the flow for sailing yachts using a technique similar to that of Raven, by adding a sheet of dipoles on the camber plane of the lifting surfaces. He also added a viscous 2-D stripping method on the hull to get an approximation of the viscous drag for the canoe body. The most widely used free-surface flow solver based on a panel method for sailing yachts is SPLASH developed by Rosen *et al.* [26]. It began with the work preceeding the 1987 match for the America's Cup and is reported in [1]. SPLASH is a nonlinear free-surface solver for predicting hydrodynamic steady and unsteady inviscid forces. In its latest evolution the coupling with a viscous flow solver is said to be under development [27].

The simultaneous coupling of integral boundary equations with an inviscid flow has been done in the past; Nishida [21] and Milewski [15] have coupled the full

3-dimensional integral boundary layer equations with an inviscid flow solver, and obtained encouraging results for a swept, tapered wing. The methodology they developed was never extended to a flow with a free surface, nor to a geometry more complex than the swept, tapered wing.

The method described in this thesis simultaneously couples a linear free-surface flow solver with quasi three-dimensional integral boundary layer equations. This form of the viscous equations assumes that there is negligible cross-flow, so that the equations can be solved in the mainstream direction only, but they account for the lateral divergence effect. These equations are exact for an axis-symmetric flow and for a 2-D flow. Also through the mass defect influence matrix, the flow at every point in the domain is influenced by the all the points, and not just those upstream of it as it is the case for two-dimensional stripping.

1.3 Overview of the Method

A diagram of the numerical method presented in this thesis is shown in Fig. 1-1. The solution of the linearized, viscous-inviscid coupled, free-surface problem starts with the solution of the inviscid base flow. The base flow is essentially the solution of the double body problem, where the body is mirrored with respect to the free surface and then the latter is removed. This equivalent to imposing no flow across the flat free-surface and it basically becomes an unbounded flow problem that is easily solved using a low order panel method. The solution requires the definition of the body and wake geometries and the operating conditions as input parameters. The solution includes computing the base inviscid velocity on the body and wakes.

The edge velocity in the coupled problem is the sum of the base inviscid velocity plus a correction due to the displacement effect of the boundary layer. The influence coefficients that provide the connection between the boundary layer displacement and the edge velocity, depend only on the geometry of the problem and are calculated next. At this point solving the quasi-3D integral boundary layer equations is possible using a Newton's method. The edge velocity equations, which provide the outer boundary
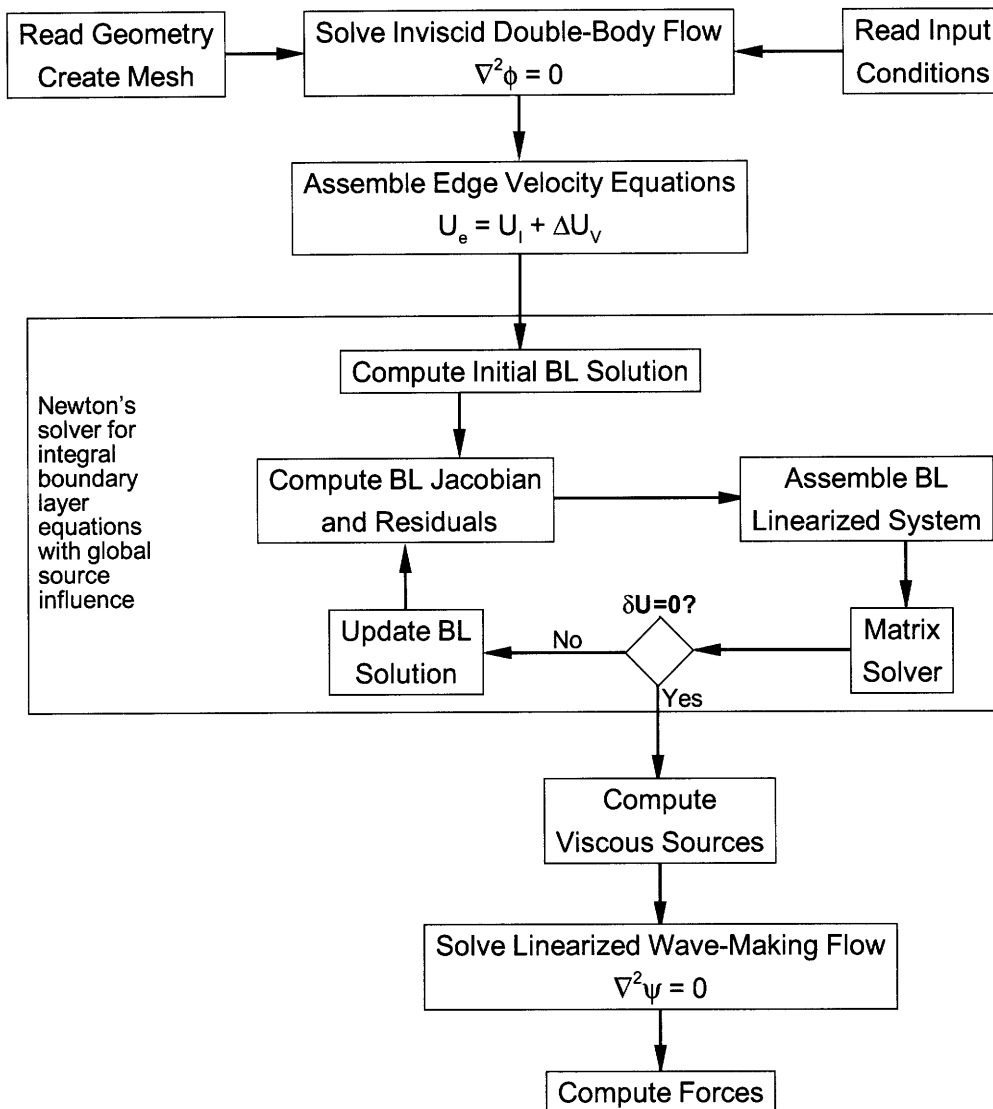
Figure 1-1: Flow diagram of the numerical procedure.

conditions, make the system of equations elliptic, thus providing, in the end, a fully coupled solution. The Newton's method used requires a set of viscous input conditions (Reynolds number, optional transition line location) as well as an initial solution which is computed using the inviscid base velocity and by marching the boundary layer equations in a direct mode.

The output of the coupled problem includes the shear stress coefficient distribution and a set of viscous blowing sources, whose effect on the outer flow is the same as that of the displacement thickness of the boundary layer. These sources are then added to

the double body solution to provide the base solution for the linearized, wave-making flow problem. For the solution of this prblem, the free-surface is reintroduced on the computational domain. The boundary conditions on the free surface are linearized and the system of equations is assembled. The linear system provides equations for two unknowns: the linear perturbation potential, which is unknown everywhere, and the wave elevation on the free surface. The first output allows determination of the pressure field on the body and therefore of the linearized forces.

The computational procedure presented in this thesis is intended to be an evaluation tool for the performance of sailing yachts, by predicting the forces, in particular drag and lift, acting on the hull and appendages. By coupling the viscous boundary layer with the inviscid flow, it is possible to compute not only the wave resistance, but also the effects of the viscosity on it and form drag, and the frictional drag. The procedure starts with an accurate description of the model to be evaluated, which is represented using NURBS surfaces and can be imported into the program directly using an Initial Graphic Exchange Specification (IGES) file that most of the computer aided-design (CAD) programs can provide.

Some of the limitations of the method here presented are: the incapability of capturing highly three-dimensional viscous flows, such as the flows at the tips of the appendages or at the intersections of the appendages with the hull, as well as highly separated flows; because of the linearized nature of the inviscid part of the problem, non-linear free-surface features will not be captured.

Chapter 2

Inviscid Flow

This chapter presents the boundary integral method to describe the flow outside of the boundary layer, where the flow can be modeled as incompressible, potential flow. The resulting equations are then discretized using a low order panel method.

2.1   Potential Flow Boundary Integral Equation

Consider a lifting, three-dimensional body immersed in an unbounded fluid moving with constant velocity $\mathbf{V}_B$. Because of the velocity being constant, this is equivalent to having a fixed body that sees a constant inflow velocity $\mathbf{U} = -\mathbf{V}_B$. The fluid volume $\mathcal{V}$ is enclosed by the body surface S_B, and the free-surface S_{FS}, with respective unit normal vectors $\vec{n}_B$ and $\vec{n}_{FS}$ pointing out of the fluid domain. Inside $\mathcal{V}$ the fluid is considered inviscid and incompressible, and with the possible the exception of thin wakes, S_W, shed from the trailing edges of the lifting surfaces, the fluid can also be assumed irrotational. These assumptions allow the definition of the fluid velocity field as the gradient of the velocity potential

$$\mathbf{U} = \nabla \Phi \tag{2.1}$$

which substituted into the continuity equation gives the Laplace's equation

$$\nabla^2 \Phi = 0 \qquad (2.2)$$

By splitting the potential into two terms, a component due to the free stream, ϕ_∞, and a perturbation due to the presence of the body, ϕ, Laplace's equation can be rewritten into a boundary integral equation using Green's third identity

$$
\begin{aligned}
4T\pi\Phi(\xi) \quad + \quad & \int\int_{S_B} \Phi(\mathbf{x})\frac{\partial G(\mathbf{x};\xi)}{\partial n} - G(\mathbf{x};\xi)\frac{\partial \Phi(\mathbf{x})}{\partial n}dS_x + \\
+ \quad & \int\int_{S_{FS}} \Phi(\mathbf{x})\frac{\partial G(\mathbf{x};\xi)}{\partial n} - G(\mathbf{x};\xi)\frac{\partial \Phi(\mathbf{x})}{\partial n}dS_x + \\
+ \quad & \int\int_{S_W} \Delta\Phi(\mathbf{x})\frac{\partial G(\mathbf{x};\xi)}{\partial n}dS_x = 0 \qquad (2.3)
\end{aligned}
$$

where $T = 0$, $1/2$, or 1 for points that are respectively outside, on the boundary, or inside the domain $\mathbf{V}$. The Green's function is defined as

$$G(\mathbf{x};\xi) = -\frac{1}{|\mathbf{x} - \xi|} \qquad (2.4)$$

The first two integrals in Eq. 2.3 represents the potential induced at a point ξ due to a continuous dipole distribution of strength $\Phi(\mathbf{x})$ and a source distribution of strength $\nabla\Phi \cdot \vec{n}$ on both the body S_B and free surface S_{FS}. The third integral, instead, represents the potential induced at a point ξ due to a continuous dipole distribution on the inviscid wake S_W with a strength equal to the potential jump across it

$$\Delta\Phi = \Phi_{S_W^+} - \Phi_{S_W^-} \qquad (2.5)$$

More details of this derivation can be found in [11] and [19].

2.1.1 Boundary Conditions

Eq. 2.3 is an integral boundary equation, and for the associated integral boundary value problem to be well defined, conditions need to be specified on all the boundary

surfaces.

Body Conditions

The hull and appendages are considered impermeable for the solution of the inviscid problem. A transpiration velocity will be superimposed later to account for the presence of the boundary layer. The body impermeability is imposed by equating the normal component on the surface of fluid to the normal component of the body velocity

$$\nabla\Phi \cdot \vec{n}_B = \mathbf{V}_B \cdot \vec{n}_B \tag{2.6}$$

Outer Surface Conditions

The outer surface is a control surface used to create a closed domain. The condition is that the perturbation velocity due to the presence of the body goes to zero on this surface, provided that it is at an infinite distance

$$\nabla\Phi \to 0, \qquad \text{as} \qquad S_\infty \to 0 \tag{2.7}$$

Wake Surface Conditions

The wake surface is in reality composed by two surfaces, S_W^+ and S_W^-, separated by a very small distance, that bound the part of the fluid volume that in a three-dimensional lifting body problem contains the vorticity. Using mass and momentum conservation at the interface, it has been shown that the surface S_W is force-free. Therefore the pressure jump across it needs to be zero

$$\Delta p = 0 \tag{2.8}$$

Lifting Surface Condition

To insure that the flow will detach smoothly from the trailing edge of the lifting surfaces, a Kutta condition is necessary. Because the shed vorticity is convected along the wake S_W, the potential jump along wake streamlines is therefore constant

in a steady flow

$$\Delta\Phi_{T.E.} = \Delta\Phi_W \tag{2.9}$$

Aft End of Waterline Condition

Most sailing yachts are designed with sterns that have a significant overhang. When sailing, the water flow raises along the overhang, past the end of the static waterline, and detaches at a position that depends primarily on the speed. The nature of the linearized solution of the free-surface problem is such that the flow does not see any part of the body that is above the static waterline. Because of this the solution for the wave elevation right at the stern can be non-zero. It is necessary to impose conditions that prevent this and make the solution reasonable for vessels with overhangs. The conditions chosen are

$$\begin{cases} \zeta(\mathbf{x}_T) = 0 \\ \left.\frac{\partial\zeta}{\partial x}\right|_{\mathbf{x}=\mathbf{x}_T} = \left.\frac{\partial z}{\partial x}\right|_{\mathbf{x}=\mathbf{x}_T} \end{cases} \tag{2.10}$$

where $\mathbf{x}_T = (x_T, y_T)$ represents a point on the transom, and ζ is the wave elevation.

2.2   The Double-Body Flow

The second integral in Eq. 2.3 is to be taken on the free-surface, however the location of this boundary is unknown a priori. The solution procedure needs to start with the choice of an initial free surface approximation and velocity distribution on it. The choice for the free surface is to use a flat surface, while the initial approximation for the velocity field is obtained by solving the double-body problem.

In this problem the real body is mirrored about the free surface, S_{FS} that corresponds to the horizontal plane $z = 0$, creating an image of it, S_I. The x axis is parallel to the velocity vector of the vessel, with the positive direction being from the stern to the bow; the y axis runs across the vessel, with the positive direction to port (Fig. 2-1); the z axis is therefore vertical and with the positive direction pointing upward.
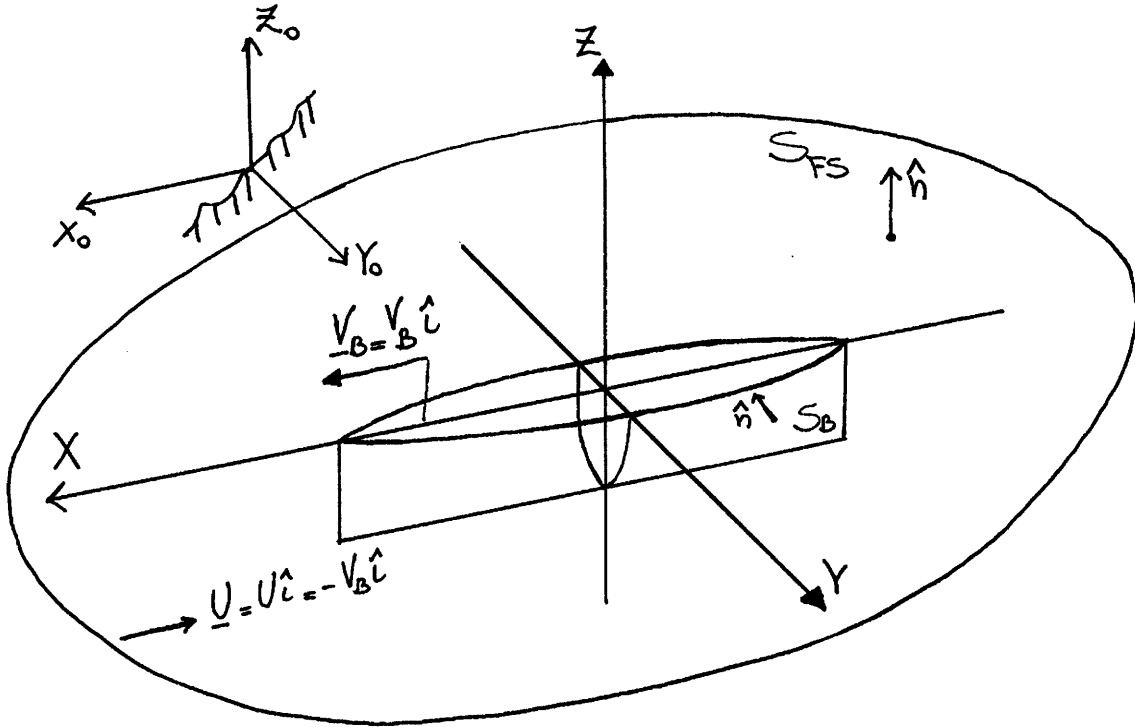
Figure 2-1: Reference system.

Singularities are distributed over both the real body and its image, collectively defined as the double-body, and the potential is first found on it.

The total perturbation potential Φ can be decomposed into two terms: the first one is the double-body perturbation, the second the linear wavemaking perturbation potential

$$\Phi = \phi + \psi \tag{2.11}$$

Substituting the above decomposition into Eq. 2.3 and solving the problem for ϕ, the Green's Theorem then becomes

$$2\pi\phi(\xi) \quad + \quad \int_{S_B \cup S_I} \phi(\mathbf{x}) \frac{\partial G(\mathbf{x}; \xi)}{\partial n} dS_x$$

$$+ \quad \int_{S_W} \Delta\phi(\mathbf{x}) \frac{\partial G(\mathbf{x}; \xi)}{\partial n} dS_x = \int_{S_B \cup S_I} G(\mathbf{x}; \xi)(-U\hat{\mathbf{i}} \cdot \mathbf{n}) dS_x \tag{2.12}$$

where in the last term the body boundary condition has been used

$$\frac{\partial \phi}{\partial n} = U_B \hat{\mathbf{i}} \cdot \mathbf{n} = -U \hat{\mathbf{i}} \cdot \mathbf{n} \tag{2.13}$$

The solution of the Green's problem in Eq. 2.12 added to the freestream potential gives the double-body potential ϕ_{DB}.

$$\phi_{DB} = \phi + \phi_\infty \tag{2.14}$$

Once the potential is known on the body, then Eq. 2.12 can be used to find it on the wake and free surface by taking the point ξ to be on them.

2.3   The Flow Linearized about the $z = 0$ Plane

The second step is to solve the linearized problem on the flat free surface. Write

$$\Phi = \phi + \psi \tag{2.15}$$

where Φ is the total disturbance potential, ϕ the double-body perturbation potential, solution of Eq. 2.12, and ψ the wave potential. The total potential Ψ is then given by

$$\Psi = \Phi + Ux \tag{2.16}$$

Assume that $\phi = O(1)$, while $\psi = O(\varepsilon)$, where $\varepsilon \ll 1$. Assume also small wave elevation, that is $\zeta = O(\varepsilon)$. In the body-fixed reference frame Φ represents the flow about a mean velocity field $\mathbf{V}_B = U_B \hat{\mathbf{i}} + V_B \hat{\mathbf{j}}$, where U_B is the forward speed of the vessel and V_B is the slip speed. In the inertial frame Φ is the total potential, so that the fluid velocity in the inertial frame is given by

$$\mathbf{V}_F = \nabla \Phi \tag{2.17}$$

2.3.1 Free-surface Boundary Conditions

Consider the free surface to be a single-valued surface, which means that breaking waves, sprays and capillary waves are neglected. The kinematic and dynamic condition imposed on the elevated surface $z = \zeta(x, y, t)$ specify its position and motion. The former states that a Lagrangian particle at the free surface must stay at the free surface for all time, that is

$$\left(\frac{d}{dt} + \nabla\Phi \cdot \nabla\right)[z - \zeta(x, y, t)] = 0, \quad \text{on } z = \zeta(x, y, t) \tag{2.18}$$

The latter condition, instead, states that the fluid pressure on the free surface must equal the atmospheric pressure, so using Bernoulli's equation

$$p - p_a = 0 = -\rho\left(\frac{d\Phi}{dt} + \frac{1}{2}\nabla\Phi \cdot \nabla\Phi + gz\right), \quad \text{on } z = \zeta(x, y, t) \tag{2.19}$$

To reformulate these relations in the body-fixed reference frame we can use the Galilean transformation

$$\frac{d}{dt} = \frac{\partial}{\partial t} - \mathbf{V}_B \cdot \nabla \tag{2.20}$$

Applying this to Eq. 2.18 and Eq. 2.19, they become

$$\left(\frac{\partial}{\partial t} - (\mathbf{V}_B - \nabla\Phi) \cdot \nabla\right)[z - \zeta(x, y, t)] = 0, \quad \text{on } z = \zeta(x, y, t) \tag{2.21}$$

$$\frac{\partial\Phi}{\partial t} - \mathbf{V}_B \cdot \nabla\Phi = -\frac{1}{2}\nabla\Phi \cdot \nabla\Phi - g\zeta, \quad \text{on } z = \zeta(x, y, t) \tag{2.22}$$

Now, using Eq. 2.15, and dropping terms that are of order $O(\varepsilon^2)$, the two free-surface boundary condition are rewritten in linearized form

$$\frac{\partial\zeta}{\partial t} - (\mathbf{V}_B - \nabla\phi) \cdot \nabla\zeta = \frac{\partial\phi}{\partial z} + \frac{\partial\psi}{\partial z}, \quad \text{on } z = \zeta(x, y, t) \tag{2.23}$$

$$\frac{\partial\psi}{\partial t} - (\mathbf{V}_B - \nabla\phi) \cdot \nabla\psi = -g\zeta + \mathbf{V}_B \cdot \nabla\phi - \frac{1}{2}\nabla\phi \cdot \nabla\phi, \quad \text{on } z = \zeta(x, y, t) \tag{2.24}$$

To be able to impose these boundary conditions, it is necessary to transfer them from the actual elevated surface $z = \zeta(x, y, t)$ to the mathematical surface $z = 0$. To do that we apply a Taylor expansions for small ζ about $z = 0$, and remembering that $\frac{\partial \phi}{\partial z} = 0$, we obtain

$$\frac{\partial \zeta}{\partial t} - (\mathbf{V}_B - \nabla \phi) \cdot \nabla \zeta = \frac{\partial^2 \phi}{\partial z^2} \zeta + \frac{\partial \psi}{\partial z}, \quad \text{on } z = 0 \qquad (2.25)$$

$$\frac{\partial \psi}{\partial t} - (\mathbf{V}_B - \nabla \phi) \cdot \nabla \psi = -g\zeta + \mathbf{V}_B \cdot \nabla \phi - \frac{1}{2} \nabla \phi \cdot \nabla \phi, \quad \text{on } z = 0 \qquad (2.26)$$

The solution we are looking for is the steady-state limit, so $\frac{\partial}{\partial t} \equiv 0$, for forward speed only, $V_B = 0$. This reduces the conditions to

$$\left(\frac{\partial \phi}{\partial x} - U_B \right) \frac{\partial \zeta}{\partial x} + \frac{\partial \phi}{\partial y} \frac{\partial \zeta}{\partial y} = \frac{\partial^2 \phi}{\partial z^2} \zeta + \frac{\partial \psi}{\partial z}, \quad \text{on } z = 0 \qquad (2.27)$$

$$\left(\frac{\partial \phi}{\partial x} - U_B \right) \frac{\partial \psi}{\partial x} + \frac{\partial \phi}{\partial y} \frac{\partial \psi}{\partial y} = -g\zeta + U_B \frac{\partial \phi}{\partial x} - \frac{1}{2} \nabla \phi \cdot \nabla \phi, \quad \text{on } z = 0 \qquad (2.28)$$

Equations 2.27 and 2.28 are the steady-state equivalent of the time-dependent free-surface boundary conditions derived by Kring [13] in his work.

2.3.2 Green's Identity

The Green's Theorem for this step is written as follows

$$2\pi \Phi(\xi) + \int_{S_B} \Phi(\mathbf{x}) \frac{\partial G(\mathbf{x}; \xi)}{\partial n} - G(\mathbf{x}; \xi) \frac{\partial \Phi(\mathbf{x})}{\partial n} \, dS_x +$$

$$+ \int_{z=0} \Phi(\mathbf{x}) \frac{\partial G(\mathbf{x}; \xi)}{\partial n} - G(\mathbf{x}; \xi) \frac{\partial \Phi(\mathbf{x})}{\partial z} \, dS_x$$

$$+ \int_{S_W} \Delta \psi(\mathbf{x}) \frac{\partial G(\mathbf{x}; \xi)}{\partial n} dS_x = 0 \qquad (2.29)$$

Now substituting Eq. 2.15 into Eq. 2.29 and using Eq. 2.12, the Green's problem can be reduced to

$$2\pi\psi(\xi) + \int_{S_B \cup z=0} \psi(\mathbf{x})\frac{\partial G(\mathbf{x};\xi)}{\partial n}\,dS_x$$

$$+ \int_{S_W} \Delta\psi(\mathbf{x})\frac{\partial G(\mathbf{x};\xi)}{\partial n}dS_x = \int_{z=0} G(\mathbf{x};\xi)\frac{\partial\psi(\mathbf{x})}{\partial z}\,dS_x \qquad (2.30)$$

The second term in the integral over the body surface is zero because of the body boundary condition. In fact if we subtract Eq. 2.13 from Eq. 2.6 we obtain

$$\frac{\partial\psi}{\partial n} = 0 \qquad (2.31)$$

The left hand side of Eq. 2.30 contains the unknown perturbation potential ψ while the right hand side contains its z-derivative. However the derivative can be expressed in term of the perturbation potential ψ and the wave elevation ζ by using the boundary conditions 2.27 and 2.28.

2.4   Numerical Solution

The inviscid flow problem is solved by using a low order panel method. This requires the creation of panels over all the geometry surfaces.

2.4.1   Geometry

Modern computer design programs for naval architecture use non-uniform rational B-spline, or NURBS, surfaces to define hull and appendage shape. A NURBS surfaces is a biparametric representation of a surface defined with spline transformation between a paramter space (u, v) and the three-dimensional space (x, y, z). The main three-components that define a NURBS surface of degree (p, q) are: a set of basis functions $N_{i,p}$ and $N_{j,q}$, a set of weights $w_{i,j}$ and a (m, n) net of control points $\mathbf{P}_{i,j}$. The points $\mathbf{P}_{i,j}$ determine the three-dimansional coordinate system, therefore are represented in Cartesian coordinates. The general equation for a NURBS surface is given by

$$S(u, v) = \frac{\sum_{i=0}^{m}\sum_{j=0}^{n} N_{i,p}(u)N_{j,q}(v)w_{i,j}\mathbf{P}_{i,j}}{\sum_{i=0}^{m}\sum_{j=0}^{n} N_{i,p}(u)N_{j,q}(v)w_{i,j}} \qquad (2.32)$$

31
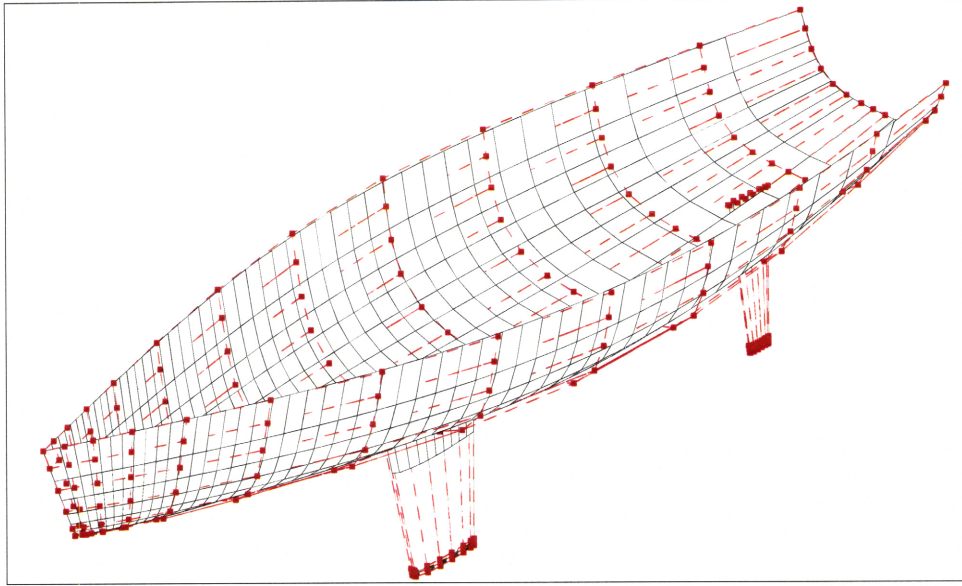
Figure 2-2: Imported geometry: the red squares connected by dashed lines represent the control net, while the grey mesh represents the surfaces after the first evaluation. Note the top of the rudder surface still coming through the hull.

The basis functions $N_{i,p}(u)$ and $N_{j,q}(v)$ are nomalized function in the direction of the parameters u and v, which are assumed to be orthogonal to one another.

The i-th normalized basis function of order p, $N_{i,p}$, is defined using a recursive relation known as the Cox-deBoor algorithm. The first step defines the basis function of order one

$$N_{1,p}(u) = \begin{cases} 1 & \text{if } t_i \leq u < t_{i+1} \\ 0 & \text{otherwise} \end{cases} \tag{2.33}$$

and the one of order p is defined by

$$N_{i,p}(u) = \frac{(u - t_i)\, N_{i,k-1}(u)}{t_{i+k-1} - t_i} + \frac{(t_{i+k} - u)\, N_{i+1,k-1}(u)}{t_{i+k} - t_{i+1}} \tag{2.34}$$

where $\mathbf{t} = \{t_i\}$ is the knot vector ofthe direction u. A more detailed description of the characteristics of the NURBS surfaces and of the numerical procedure to evaluate the basis functions and the surfaces themselves are found in [12] and in [25].

The geometry hull and appendage is imported from a CAD program using a standard exchange file format called IGES (Initial Graphics Exchange Specification). An

32
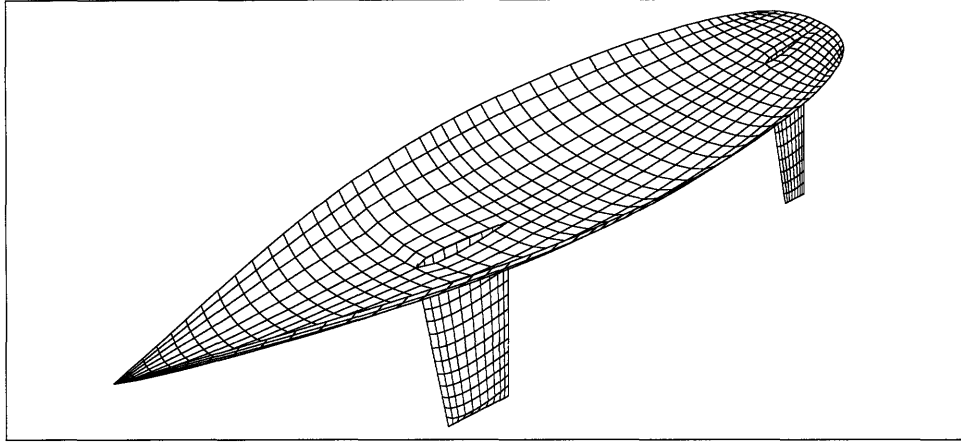
Figure 2-3: Imported geometry: the surfaces after having been trimmed and divided in the desired number of panels.

example of an IGES file is given in Appendix A. This file contains all the necessary characteristic and geometric information to evaluate the surfaces. Fig. 2-2 shows the control net of the imported geometry and the mesh after the first evaluation. The computational mesh, before the free-surface and wakes are added, is shown in Fig. 2-3.

The geometry is first evaluated by computing each of the NURBS surfaces at a number of points input by the user at constant intervals of the parameters u and v. Then the intersection between the appendage surfaces and the hull are computed and the excess is trimmed off. At this point all the surfaces are rotated into the final position according to the desired leeway, heel, and rudder angle, input by the user. Then the intersection between the hull and the unperturbed free surface is computed and the part of the hull above it is discarded.

2.4.2 Inviscid Computational Mesh

Once the surfaces that bound the fluid domain are found, they are divided into the desired number of intervals in each direction to make a quadrilateral mesh (see Fig. 2-4).

Each part of the boat (hull, keel, and rudder) is made up of two surfaces, a port and a starboard one. The user control the number of panels that each surface is divided into

33

in both the longitudinal and the tranverse/vertical direction. The number of panels in the port and starboard surface are intended to be the same, with the exception of the hull surface, where the transverse number of panel can be different in order to keep the panel size similar on the two halves when the boat is heeled over and the starboard surface is much larger than the port (Fig. 2-5). The user can also decide the type of spacing of the panels in each direction between three choices: "constant", all panels have the same length in the specified direction; "cosine", the dimensions of the panels are set as a cosine distribution; "geometric", the dimension of the panels is a geometric progression with small panels at the end and bigger in the center. The "cosine" spacing is used in the longitudinal direction on the appendages, while the vertical spacing is geometric. For the hull, the longitudinal spacing is geometric, with the transverse set to constant. On the hull the user can also decide how many panels are used at the intersection of the appendages. A sample file with all the input information necessary to generate the geometry is shown in Appendix B.

The inviscid wakes are built from the trailing edges of the keel and rudder and are carried downstream in the x-direction, the same direction as the freestream velocity. Along their entire length they maintain the same span, i.e. no roll-up. The keel wake, even in the case with no leeway is carried aft with an angle such that it misses the rudder by twice the rudder thickness. The top of the top row of panels is attached to the hull and the free surface at the same points as the rudder wake, so to have only one discontinuity in a known location.

The free surface is discretized using a polar mesh, which combines the benefits of covering a large area with a smaller number of panels than a rectangular mesh, and of grouping the panels closer to the hull for increased accuracy. It attaches to the hull at the static waterline, so the number of panels in the direction around the hull is determined by the longitudinal number of panels on the hull plus the tranverse number of panels in the stern. The number of panels in the radial direction is input by the user. The outer edge of the free surface is an ellipse, and the mesh is first created by linear interpolation. It is then run through an elliptic grid generator to make neighbor panels as close in dimensions as possible.
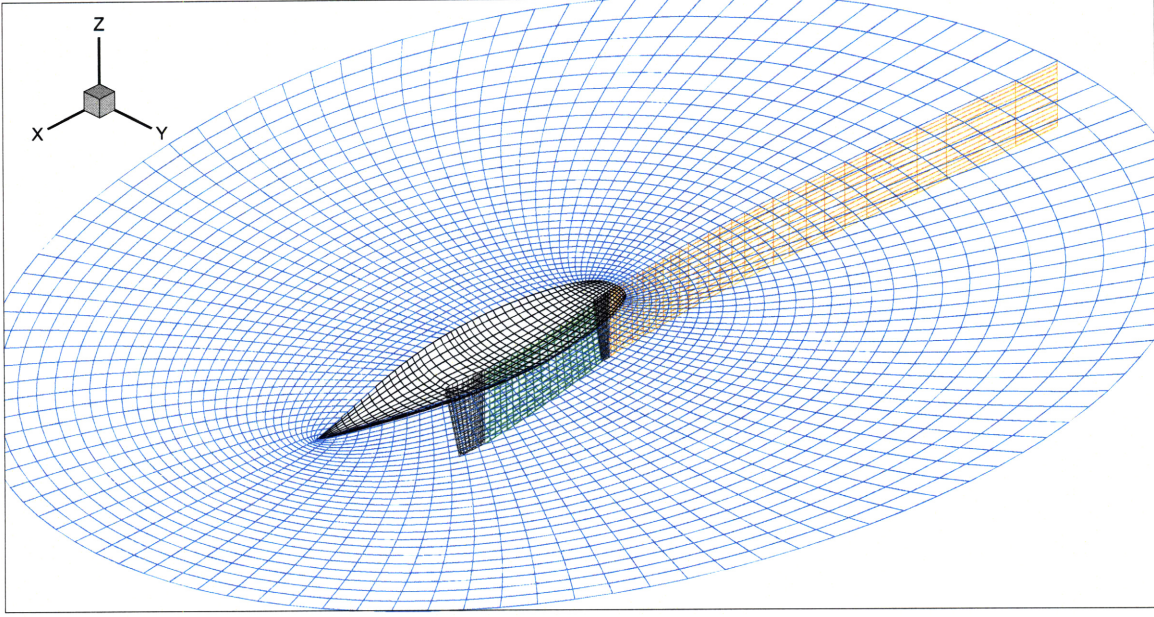
Figure 2-4: Computational mesh for the inviscid problem.

2.4.3 Discretized Equations

In order to discretize the equation, let ξ_i be the centroid of panel i, and assume that the potential $\phi(\xi_i)$ and its normal derivative $\partial\phi(\xi_i)/\partial n$ are constant over the entire panel i. Writing the integral over each surface as the summation of the integrals over each panel on the surfaces, then $\phi(\xi_i)$ and $\partial\phi(\xi_i)/\partial n$ can be taken outside of the integral signs and the Eq. 2.12 can be recast as

$$2\pi\phi(\xi_i) + \sum_{j=1}^{NB} \hat{A}_{i,j}\phi(\xi_j) + \sum_{j=1}^{M} C_{i,m}\Delta\phi(\xi_m) = \sum_{j=1}^{NB} S_{i,j}(-U\hat{\mathbf{i}} \cdot \mathbf{n}_j) \qquad (2.35)$$

NB is the total number of panels on the body and on the image, while M is the number of dipole strips on S_W. And

$$\tilde{A}_{i,j} = \int_{\text{Panel}_j} \frac{\partial G(\mathbf{x}; \xi_i)}{\partial n} dS_x \qquad (2.36)$$

$$S_{i,j} = \int_{\text{Panel}_j} G(\mathbf{x}; \xi_i) dS_x \qquad (2.37)$$

$$C_{i,m} = \int_{\text{Panel}_m} \frac{\partial G(\mathbf{x}; \xi_i)}{\partial n} dS_x \qquad (2.38)$$

35
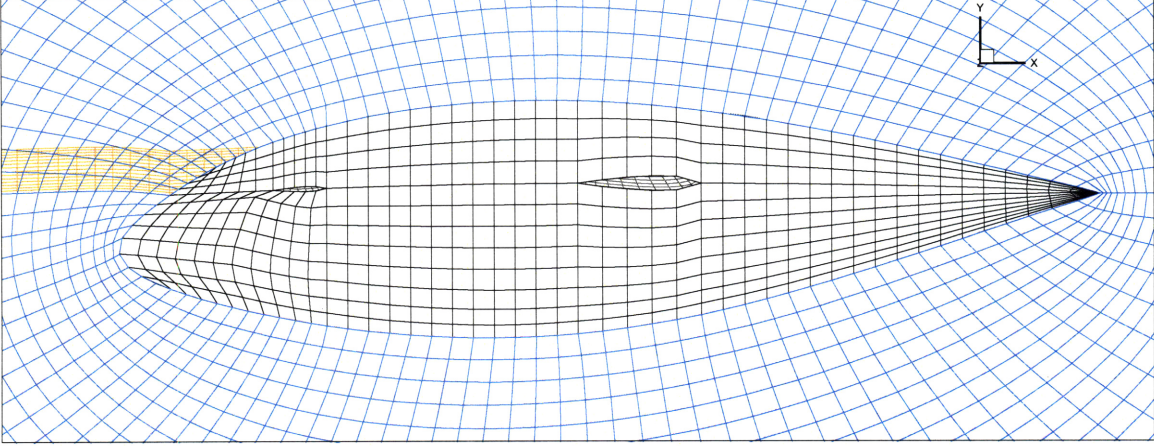
Figure 2-5: Detail of the computational mesh: the starboard side has 8 panels in the transverse direction, while the port has 4.

These influence coefficients, which depend only on the body, wake, and free-surface geometry, are evaluated using RPAN [20]. $\Delta\phi(\xi_j)$, which represents the jump in potential across the wake, can be related to the value of the potential on either side of the trailing edge of the surface shedding the wake, that is to the potential on the double-body. Therefore the three terms on the left hand side of Eq. 2.35 can be rewritten as a single summation

$$\sum_{j=1}^{\text{NB}} A_{i,j}\phi(\xi_j) = \sum_{j=1}^{\text{NB}} S_{i,j}(-U\hat{\mathbf{i}}\cdot\mathbf{n}_j) \tag{2.39}$$

Because Eq. 2.39 can be written for the centroid of each panel on the body (i =1,...,NB), it forms a system of NB linear equation in NB unknowns. The solution for the perturbation potential is then

$$\phi(\xi_i) = \sum_{j=1}^{\text{NB}} \left[\sum_{k=1}^{\text{NB}} A_{i,k}^{-1} S_{k,j} \right] (-U\hat{\mathbf{i}}\cdot\mathbf{n}_j), \quad \text{for } i = 1,...,\text{NB} \tag{2.40}$$

With the potential known on the body and its image, using Green's Theorem again, it is possible to compute the potential on the wake ϕ^W and on the free surface ϕ^{FS}, which is necessary for the linear solution.

$$\phi_i^W = -\sum_{j=1}^{\text{NB}} \tilde{A}_{i,j}^W \phi(\xi_j) - \sum_{j=1}^{\text{NW}} C_{i,j}\Delta\phi(\xi_j) + \sum_{j=1}^{\text{NB}} S_{i,j}^W(-U\hat{\mathbf{i}}\cdot\mathbf{n}_j) \tag{2.41}$$

36

$$\phi_i^{FS} = -\sum_{j=1}^{NB} \tilde{A}_{i,j}^{FS}\phi(\xi_j) - \sum_{j=1}^{NW} C_{i,j}\Delta\phi(\xi_j) + \sum_{j=1}^{NB} S_{i,j}^{FS}(-U\hat{\mathbf{i}}\cdot\mathbf{n}_j) \qquad (2.42)$$

Similarly to Eq. 2.39 the first two terms in the right hand side of each of the above equations can be collapsed into a single one.

$$\phi_i^{W} = -\sum_{j=1}^{NB} A_{i,j}^{W}\phi(\xi_j) + \sum_{j=1}^{NB} S_{i,j}^{W}(-U\hat{\mathbf{i}}\cdot\mathbf{n}_j), \quad \text{for } i = \text{NB}+1, ..., \text{NB}+\text{NW} \quad (2.43)$$

$$\phi_i^{FS} = -\sum_{j=1}^{NB} A_{i,j}^{FS}\phi(\xi_j) + \sum_{j=1}^{NB} S_{i,j}^{FS}(-U\hat{\mathbf{i}}\cdot\mathbf{n}_j), \quad \text{for } i = \text{NB}+\text{NW}+1, ..., \text{NT} \quad (2.44)$$

where NFS is the number of panels on the free surface, NT is the total number of panels in the domain.

The terms in the left hand side of Eq. 2.30 is discretized in a similar way as above. Using the assumption that $\partial\psi(\mathbf{x})/\partial z$ can be considered constant over each panel, it can be taken outside the integral sign, and the equation can be rewritten as

$$2\pi\psi(\xi_i) + \sum_{j=1}^{NT} \hat{A}_{i,j}\psi(\xi_j) + \sum_{j=1}^{M} C_{i,m}\Delta\psi(\xi_m) = \sum_{j=1}^{NFS} S_{i,j}\frac{\partial\psi_j(\mathbf{x})}{\partial z} \qquad (2.45)$$

$\partial\psi_j(\mathbf{x})/\partial z$ is obtained from the discretization of the free-surface boundary conditions.

2.4.4   Discretized Boundary Conditions

Eqs. 2.27 and 2.28 have partial derivatives taken with respect to the main Cartesian axis, however, because the free-surface grid is an O-type grid, these have to be written as a function of the derivatives along the radial and circumferential lines. Calling these directions p and s, the x and y-derivatives can be written

$$\frac{\partial f}{\partial x} = \frac{1}{J}\left(\frac{\partial y}{\partial s}\frac{\partial f}{\partial p} - \frac{\partial y}{\partial p}\frac{\partial f}{\partial s}\right) \qquad (2.46)$$

$$\frac{\partial f}{\partial y} = \frac{1}{J}\left(-\frac{\partial x}{\partial s}\frac{\partial f}{\partial p} + \frac{\partial x}{\partial p}\frac{\partial f}{\partial s}\right) \qquad (2.47)$$

where J is the Jacobian

$$J = \frac{\partial y}{\partial s}\frac{\partial x}{\partial p} - \frac{\partial y}{\partial p}\frac{\partial x}{\partial s} \tag{2.48}$$

The p and s-derivatives are then approximated using finite differences. A second order, centered differencing scheme is used for the approximation of the y-derivative, and instead a 4-point upwind differencing scheme is used for the x-derivatives. This scheme was first implemented by C.W. Dawson in [5], and was found to be the most effective.

Chapter 3

Boundary Layer Flow

The viscous flow inside the boundary layer is solved using integral boundary layer equations. These are solved on the hull, the keel, and the rudder and their respective wakes. On the hull the boundary layer starts at the bow and moves downstream to the stern and then onto the wake, somewhere transitioning from laminar to turbulent. On the keel and rudder, the boundary layer is computed on both the port and starboard surfaces, then combined into one on the wake. The attachment line here is not known a priori; it is initially take as the inviscid leading-edge stagnation line, but its location is then adjusted as the boundary layer solution converges.

3.1   Governing Equations

The simultaneous coupling of integral boundary equations with an inviscid flow has been done in the past; Nishida ([21]) and Milewski ([15]) have coupled the full 3-dimensional integral boundary layer equations with an inviscid flow solver, and obtained encouraging results for a swept, tapered wing. Neither of them has tried the coupling for a free-surface flow, nor for a geometry more complicated than a swept wing. Mantzaris directly coupled instead a 2-dimensional viscous solution with a Rankine panel method solver for free-surface flows. The approach taken here lays somewhere in between: quasi-3D integral equations are simultaneously coupled with a free-surface flow solver for a sailing yacht with lifting surfaces. It is a quasi-3D for-

mulation because the equations are solved only in the streamwise direction, and the crossflow is assumed to be zero, however they are not simply 2-dimensional because a term is added which takes into account the separation between the computational lines, and whether they are converging or diverging. Moreover in two dimensions the boundary layer is only affected by the points upstream on the same line; in this method instead, the edge velocity at any single point depends on the mass defects at every point in the computational domain.

The boundary layers in this type of problem, at high Reynolds number, are generally thin compared to a characteristic length of the geometry (be that the waterline length for the hull or the average chord length for the lifting surfaces). Under these assumptions, the pressure can be taken as constant through the boundary layer thickness and the Navier-Stokes equations can be simplified into the thin shear layer equations [30]. The integral equations are derived from these through the integration in the direction perpendicular to the wall of linear combinations of the continuity equation and the thin shear layer momentum equation. Because the fluid is incompressible the density is dropped from the formulation, and the equations are solved in non-dimensional form (a complete derivation is found in [16])

Momentum Equation

$$\frac{1}{b}\frac{db}{ds} + \frac{d\theta}{ds} + (2 + H)\frac{\theta}{U_e}\frac{dU_e}{ds} = \frac{C_f}{2} \tag{3.1}$$

Kinetic Energy Equation

$$\frac{\theta}{H^*}\frac{dH^*}{ds} + (1 - H)\frac{\theta}{U_e}\frac{dU_e}{ds} = 2\frac{C_D}{H^*} - \frac{C_f}{2} \tag{3.2}$$

Shear Stress Lag Equation

$$\frac{\delta}{C_\tau}\frac{dC_\tau}{ds} = K_C \left(C_{\tau,Eq}^{1/2} - C_\tau^{1/2} \right) \tag{3.3}$$

The transport equation for the maximum shear stress coefficient C_τ, Eq. 3.3, is used when the viscous flow has transitioned to turbulent regime. In the laminar regions,

it is substituted with an equation which calculates the amplitude growth of the most amplified Tollmien-Schlichting wave

$$\frac{d\tilde{n}}{ds} = \frac{d\tilde{n}\left(H_k\right)}{dRe_\theta}\frac{dRe_\theta\left(H_k, \theta\right)}{ds} \tag{3.4}$$

The first term on the right end side of (3.4) is an empirical correlation of the spatial growth rates from the Orr-Sommerfeld equation [6]; the second is derived from the properties of the Falkner-Skan profile family. When $\tilde{n}$ goes above $\tilde{n}_{crit}$ transition is reached and the shear stress lag equation is used.

Equations 3.1 and 3.2 represent the streamwise momentum conservation and the kinetic energy conservation. b in the first term of the momentum equation is separation between computational lines, while U_e is the edge velocity. The momentum thickness shape parameter H, the kinetic energy shape parameter H^*, the skin friction coefficient C_f, the dissipation coefficient C_D and the shear stress equilibrium coefficient $C_f^{1/2}$ are defined in Appendix C. The coefficient K_C is an empirical constant taken to be equal to 5.6 (value suggested by Green [9] and used by Milewski [15]).

3.2 Domain and Coordinate System

The governing equations given above are written in curvilinear coordinates, where s is meant to be the streamwise direction. The assumption used is that the cross-flow is negligible and therefore no equations are necessary in that direction. However in this work, s is not computed from the inviscid flow solution, but rather taken as the best estimate of what the inviscid streamlines would look like, and the grid is built to approximate those at best. This was found to work very well on most of the domain with the exception of a small area around each corner of the stern, where the angle between the grid line and the inviscid velocity vector becomes larger.

The boundary layer computational domain is shown in Fig. 3-1. This is largely based on the inviscid domain: the panels on all the hull surfaces are exactly the same. The appendage wakes are not carried as far downstream as the inviscid wake, but only
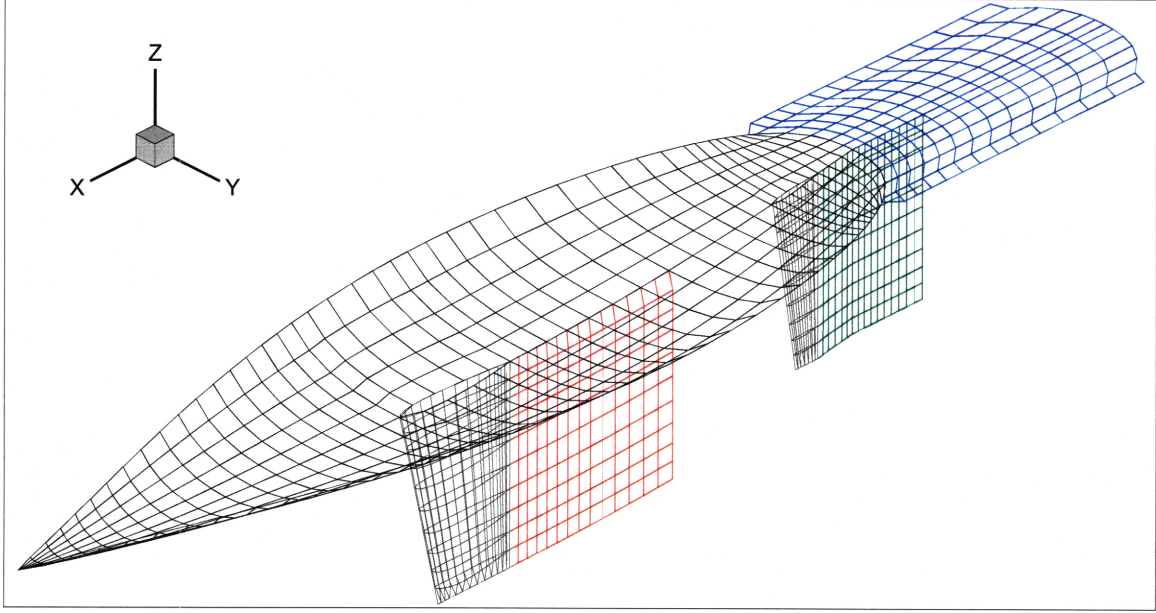
Figure 3-1: The boundary layer flow domain.

for about two appendage chordlengths. The hull wake is new and simply carries the computational lines from the stern of the boat straight downstream.

3.3   Primary Variables

The presence of three boundary layer governing equations requires the choice of three primary variables. In this work these are taken to be m, the mass defect, θ, the momentum thickness, and, depending on the regime of the individual point, $\tilde{n}$, the amplitude growth, for the laminar regions, or $C_\tau^{1/2}$, the square root of the maximum shear stress coefficient.

The mass defect m is related to the mass displacement thickness δ^* and the edge velocity U_e

$$m = \delta^* U_e \qquad (3.5)$$

U_e and δ^* are not primary variables and must be referred to m. In section 3.4.2 expressions for the edge velocity as function of the mass defect only are derived. Using these expressions, then δ^* is easily found from 3.5.

42

All the other variables present in equations 3.1-3.3 are written as functions of the primary variables; closure formulae are given in Appendix C.

3.4 Wall Transpiration Model

The effect of the boundary layer are introduced into the potential formulation by means of a wall transpiration model. In this model, blowing sources of unknown strength, called viscous sources, are added to the panels on the body, wake, and free surface. The effect of the viscous sources is to displace the potential flow away from the body, and to create a component of velocity normal to the body. This Equivalent Inviscid Flow (EIF) has the same velocity at the edge of the boundary layer as the real flow (see Fig. 3-2). The governing equation for the EIF is derived from Eq. 2.3, where one extra term is added

$$
\begin{aligned}
4T\pi\tilde{\Phi}(\xi) + \int\int_{S_B} \tilde{\Phi}(\mathbf{x})\frac{\partial G(\mathbf{x};\xi)}{\partial n} - G(\mathbf{x};\xi)\frac{\partial\tilde{\Phi}(\mathbf{x})}{\partial n}dS_x + \\
+ \int\int_{S_{FS}} \tilde{\Phi}(\mathbf{x})\frac{\partial G(\mathbf{x};\xi)}{\partial n} - G(\mathbf{x};\xi)\frac{\partial\tilde{\Phi}(\mathbf{x})}{\partial n}dS_x + \\
+ \int\int_{S_W} \Delta\tilde{\Phi}(\mathbf{x})\frac{\partial G(\mathbf{x};\xi)}{\partial n}dS_x \\
+ \int\int_{S_B\cup S_{FS}\cup S_W} G(\mathbf{x};\xi)\sigma^v(\mathbf{x})dS_x = 0
\end{aligned}
\tag{3.6}
$$

Both the potential $\tilde{\Phi}$ and the viscous sources σ^v are unknown in this equation. The potential and boundary layer equations are coupled through the edge velocity, which depends on the viscous sources. The edge velocity at each panel node is given by an inviscid term and a term depending on the unknown blowing sources through the mass defect m by

$$
U_{e_i} = U_{inv_i} + \sum_{j=1}^{N} D_{i,j}m_j, \quad 1 \le i \le N
\tag{3.7}
$$
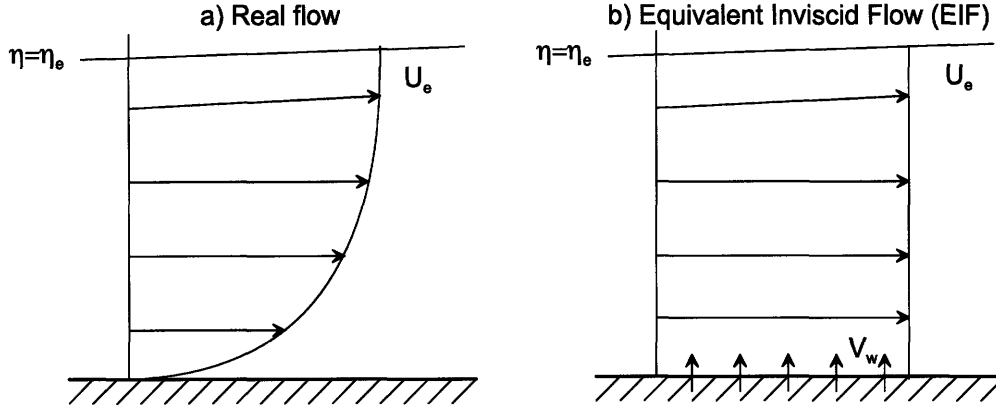
Figure 3-2: Velocity profiles for the real and equivalent inviscid flows.

N is the total number of nodes in the domain. The mass defect is directly related to the strength of the viscous sources σ^v by

$$\sigma_i^v = \frac{dm_i}{ds} \tag{3.8}$$

d/ds is the derivative with respect to the curvilinear coordinate in the streamwise direction.

3.4.1 "Viscous" Potential

The viscous sources are added to the equation in a manner similar to the potential sources. Using the same assumptions and simplifications as in the case of the double body flow, Eq. 3.6 can be discretized as

$$\sum_{j=1}^{NB} A_{i,j} \tilde{\phi}(\xi_j) = \sum_{j=1}^{NB} S_{i,j}(-U\hat{\mathbf{i}} \cdot \mathbf{n}_j) + \sum_{j=1}^{NP} B_{i,j} \sigma_j^v \tag{3.9}$$

where $\tilde{\phi}$ is the sum of the double-body inviscid perturbation potential and the potential due to the viscous sources (which will be referred to as the "viscous" potential), and NP is the total number of panels carrying a viscous source.

$$\tilde{\phi} = \phi + \phi_{vis} \tag{3.10}$$

44

On the free surface, however, only few σ_j^v directly astern of the vessel will have non-zero value. From Eq. 3.9 the perturbation potential can still be found by inverting $A_{i,j}$

$$\tilde{\phi}(\xi_i) = \sum_{j=1}^{NB} \left[\sum_{k=1}^{NB} A_{i,k}^{-1} S_{k,j} \right] (-U\hat{\mathbf{i}} \cdot \mathbf{n}_j) + \sum_{j=1}^{NB} \left[\sum_{k=1}^{NB} A_{i,k}^{-1} B_{k,j} \right] \sigma_j^v, \quad 1 \le i \le NB \quad (3.11)$$

The total potential $\tilde{\Phi}$ is obtained by adding the freestream potential ϕ_∞, and can be written as the summation of an inviscid part and a "viscous" part dependent only on the viscous blowing sources

$$\tilde{\Phi} = \Phi_i + \sum_{j=1}^{NP} H_{i,j}^P \sigma_j^v, \quad 1 \le i \le NB \quad (3.12)$$

Φ_i is the total inviscid potential, ϕ_i the solution of the inviscid problem

$$\Phi_i = \phi_i + \phi_\infty = \phi_\infty + \sum_{j=1}^{NB} \left[\sum_{k=1}^{NB} A_{i,k}^{-1} S_{k,j} \right] (-U\hat{\mathbf{i}} \cdot \mathbf{n}_j) \quad (3.13)$$

$H_{i,j}^P$ is an influence coefficient computed by solving NB systems of linear equations, where the right end side vectors are given by the columns of the source influence matrix $B_{i,j}$, and it represents the potential at the centroid of panel i due to a unit source at panel j.

$$H_{i,j}^P = \sum_{k=1}^{NB} A_{i,k}^{-1} B_{k,j} \quad (3.14)$$

$\mathbf{H}^P$ depends on the discretization of the body and wake geometries, but it is independent of the flow, therefore needs to be computed only once.

A similar approach is used for the off-body points, and the potential on the wake is , $NB + 1 \le i \le NB + NW$, first written as

$$\tilde{\phi}_i^W = \phi_i^W + \sum_{j=1}^{NP} H_{i,j}^P \sigma_j^v \quad (3.15)$$

then, starting from

$$\tilde{\phi}_i^W = -\sum_{j=1}^{NB} A_{i,j}^W \tilde{\phi}(\xi_j) + \sum_{j=1}^{NB} S_{i,j}^W (-U\hat{\mathbf{i}} \cdot \mathbf{n}_j) + \sum_{j=1}^{NP} B_{i,j}^W \sigma_j^v \qquad (3.16)$$

and substituting Eq. 3.11 into it, we find that

$$\phi_i^W = -\sum_{j=1}^{NB} A_{i,j}^W \left\{ \sum_{j=1}^{NB} \left[\sum_{k=1}^{NB} A_{i,k}^{-1} S_{k,j} \right] (-U\hat{\mathbf{i}} \cdot \mathbf{n}_j) \right\} + \sum_{j=1}^{NB} S_{i,j}^W (-U\hat{\mathbf{i}} \cdot \mathbf{n}_j) \quad (3.17)$$

which gives

$$H_{i,j}^P = \sum_{k=1}^{NB} \left[\sum_{l=1}^{NB} A_{i,l}^W A_{l,k}^{-1} \right] B_{k,j} + B_{i,j}^W \qquad (3.18)$$

In this case the influence coefficient $H_{i,j}^P$ is comprised of two terms: the first represents the change in the body dipole strengths due to the presence of the blowing sources, while the second is the direct contribution of the blowing sources.

With the same procedure, the solution for the points on the free surface $NB + NW + 1 \leq i \leq NT$ is found by

$$\tilde{\phi}_i^{FS} = \phi_i^{FS} + \sum_{j=1}^{N} H_{i,j}^P \sigma_j^v \qquad (3.19)$$

$$\phi_i^{FS} = -\sum_{j=1}^{NB} A_{i,j}^{FS} \left\{ \sum_{j=1}^{NB} \left[\sum_{k=1}^{NB} A_{i,k}^{-1} S_{k,j} \right] (-U\hat{\mathbf{i}} \cdot \mathbf{n}_j) \right\} + \sum_{j=1}^{NB} S_{i,j}^{FS} (-U\hat{\mathbf{i}} \cdot \mathbf{n}_j) \quad (3.20)$$

$$H_{i,j}^P = \sum_{k=1}^{NB} \left[\sum_{l=1}^{NB} A_{i,l}^{FS} A_{l,k}^{-1} \right] B_{k,j} + B_{i,j}^{FS} \sigma_j^v \qquad (3.21)$$

3.4.2 Edge Velocity Equations

Now, the potential is everywhere expressed as the sum of a inviscid term and one depending on the viscous sources

$$\tilde{\Phi}_i = \Phi_i + \sum_{j=1}^{NP} H_{i,j}^P \sigma_j^v, \quad 1 \leq i \leq NP \qquad (3.22)$$

46

However what we need is an expression of the edge velocity as function of the mass defect, as to have a complete set of equations which solve the boundary layer problem. It is possible to find the edge velocity by differentiating Eq. 3.22 with respect to the curvilinear streamwise coordinate. Because the boundary layer is solved at the panel nodes instead of the centroids, the edge velocity is computed at the nodes

$$
\begin{aligned}
U_{e_i} &= \frac{d\tilde{\tilde{\Phi}}_i}{ds} \\
&= \frac{d\Phi_i}{ds} + \frac{d}{ds}\left(\sum_{j=1}^{NP} H_{i,j}^P \sigma_j\right) \\
&= U_{inv_i} + \sum_{j=1}^{NP} H_{i,j}^V \sigma_j^v \qquad 1 \le i \le N
\end{aligned}
\tag{3.23}
$$

Then applying the wall transpiration model (3.8), we finally find

$$
U_{e_i} = U_{inv_i} + \sum_{j=1}^{N} D_{i,j} m_j \quad 1 \le i \le N
\tag{3.24}
$$

where, again, the blowing sources σ_j^v are panel quantities expressed at the centroids, while the mass defects m_j are nodal quantities.

Fig. 3-3 shows the contribution to the potential over the domain due to a unit strength source distribution on a generic panel. This is equal to plotting the column of matrix $\mathbf{H}^P$ corresponding to such panel. Fig. 3-4 is, instead, a plot of a generic n-th column of the mass defect influence matrix $\mathbf{D}$, and represents the contribution to the edge velocity of a unit mass defect at the node n. This has the same shape as a doublet placed on the same node and the reason is because a unit mass defect is equivalent to having to pairs of sources and sinks on the four adjacent panels.

3.5 Integration with the Inviscid Problem

We have now developed all the necessary equations to solve the coupled inviscid-viscous problem. Chapter 4 gives the details of how the solution is actually found. This section describes how the solution of the coupled problem affects the linear flow

47
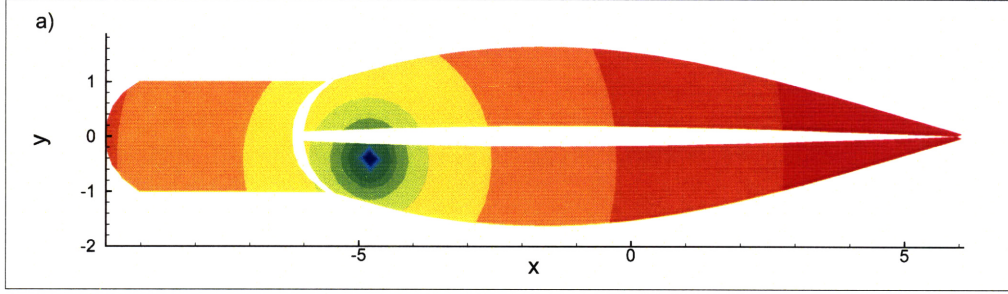
Figure 3-3: Plot of a column of $\mathbf{H}^P$
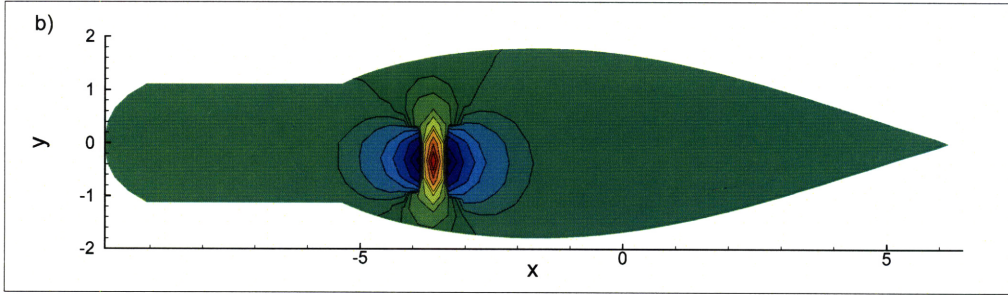
Figure 3-4: Plot of a column of $\mathbf{D}$.

problem.

Once the converged values for the mass defect m are obtained, using Eq. 3.8 combined with Eq. 3.22 a value for the "viscous" perturbation potential ϕ_{vis} is found. This is added to the double-body perturbation potential to give the base potential used in the solution of the linearized flow problem, so that now the total perturbation potential is given by

$$\tilde{\Phi} = \tilde{\phi} + \psi \tag{3.25}$$

It is the linearized flow which has ship waves and wave resistance. Using the same procedure as in section 2.3.2, it is found that the governing equation for the linear perturbation potential ψ (Eq. 2.30) is left unchanged. The body boundary condition used is still the one given in Eq. 2.31, therefore allowing the viscous sources to give rise a transpiration velocity.

Finally, the free-surface boundary conditions are obtained from Eqs. 2.27-2.28 by

48

simply substituting ϕ with $\tilde{\phi}$ to give

$$\left(\frac{\partial \tilde{\phi}}{\partial x} - U_B\right)\frac{\partial \zeta}{\partial x} + \frac{\partial \tilde{\phi}}{\partial y}\frac{\partial \zeta}{\partial y} = \frac{\partial^2 \tilde{\phi}}{\partial z^2}\zeta + \frac{\partial \psi}{\partial z}, \quad \text{on } z = 0 \qquad (3.26)$$

$$\left(\frac{\partial \tilde{\phi}}{\partial x} - U_B\right)\frac{\partial \psi}{\partial x} + \frac{\partial \tilde{\phi}}{\partial y}\frac{\partial \psi}{\partial y} = -g\zeta + U_B\frac{\partial \tilde{\phi}}{\partial x} - \frac{1}{2}\nabla\tilde{\phi}\cdot\nabla\tilde{\phi}, \quad \text{on } z = 0 \qquad (3.27)$$

Chapter 4

Solution of the Coupled Problem

The boundary layer's governing equations (3.1)-(3.3), together with the definition of the mass defect (3.5) and the equation for the edge velocity (3.24) form the closed system of equations for the problem. The system is elliptic in nature because of the global influence of the mass defect m on the edge velocities U_e. The solution is found using a Newton iterative solver.

This procedure provides a simultaneous solution for all points.

4.1   Solution by Newton's Method

Newton's method is commonly used to solve a system of nonlinear equations

$$\mathbf{F}(\mathbf{X}) = 0 \tag{4.1}$$

Given an estimate solution $\mathbf{X}_0$, generally this will not satisfy the system, and a correction $\delta\mathbf{X}$ has to be applied to the initial guess to find the exact solution

$$\mathbf{X} = \mathbf{X}_0 + \delta\mathbf{X} \tag{4.2}$$

The system of equations can be rewritten as

$$\mathbf{F(X)} = \mathbf{F(X_0 + \delta X)}$$
$$= \mathbf{F(X_0)} + \frac{\partial \mathbf{F}}{\partial \mathbf{X}}\delta \mathbf{X} + \frac{\partial^2 \mathbf{F}}{\partial \mathbf{X}^2}\delta \mathbf{X}^2 + ... \tag{4.3}$$

For small corrections all the terms beyond the linear one can be ignored, and $\delta \mathbf{X}$ is then computed as

$$\delta \mathbf{X_1} = -\left[\frac{\partial \mathbf{F}}{\partial \mathbf{X}}\right] \mathbf{F(X_0)} \tag{4.4}$$

where $\frac{\partial \mathbf{F}}{\partial \mathbf{X}}$ is the Jacobian $\mathbf{J}_{i,j}$ of the system. The correction is then added to the initial estimate to find a new estimate $\mathbf{X_1} = \mathbf{X_0} + \delta \mathbf{X_1}$. This procedure can be repeated iteratively until the correction $\delta \mathbf{X}_n$ at the n-th iteration becomes smaller than a set tolerance.

4.2 Assembly of the Newton System Matrix

The form of the Newton system is

$$[\mathbf{J}_{i,j}]\left\{ \begin{array}{c} \delta C_\tau \\ \delta \theta_j \\ \delta m_j \end{array} \right\} = \{\mathbf{R}_i\} \quad 1 \le i \le N \tag{4.5}$$

where $\mathbf{J}_{i,j}$ is a 3x3 matrix and the residual vector $\mathbf{R}_i$ is 3x1 array.

Each 3x3 Jacobian assumes three different forms depending on the position in the global Newton matrix, but none of them are all zero, therefore making the global matrix a square matrix. Consider a single computational line, where the nodes are numbered with an index that increases as it moves downstream. Then:

Case 1: $j = i$

$$\mathbf{J}_{i,i} = \begin{bmatrix} \frac{\partial F_i^M}{\partial C_{\tau_i}} & \frac{\partial F_i^M}{\partial \theta_i} & \frac{\partial F_i^M}{\partial m_i} \\ \frac{\partial F_i^K}{\partial C_{\tau_i}} & \frac{\partial F_i^K}{\partial \theta_i} & \frac{\partial F_i^K}{\partial m_i} \\ \frac{\partial F_i^S}{\partial C_{\tau_i}} & \frac{\partial F_i^S}{\partial \theta_i} & \frac{\partial F_i^S}{\partial m_i} \end{bmatrix} \tag{4.6}$$

Case 2: $j = i - 1$

$$\mathbf{J}_{i,i} = \begin{bmatrix} \frac{\partial F_i^M}{\partial C_{\tau_{i-1}}} & \frac{\partial F_i^M}{\partial \theta_{i-1}} & \frac{\partial F_i^M}{\partial m_{i-1}} \\ \frac{\partial F_i^K}{\partial C_{\tau_{i-1}}} & \frac{\partial F_i^K}{\partial \theta_{i-1}} & \frac{\partial F_i^K}{\partial m_{i-1}} \\ \frac{\partial F_i^S}{\partial C_{\tau_{i-1}}} & \frac{\partial F_i^S}{\partial \theta_{i-1}} & \frac{\partial F_i^S}{\partial m_{i-1}} \end{bmatrix} \tag{4.7}$$

Case 3: $j \neq i, i - 1$

$$\mathbf{J}_{i,i} = \begin{bmatrix} 0 & 0 & \frac{\partial F_i^M}{\partial m_j} \\ 0 & 0 & \frac{\partial F_i^K}{\partial m_j} \\ 0 & 0 & \frac{\partial F_i^S}{\partial m_j} \end{bmatrix} \tag{4.8}$$

The generic residual vector is instead given by

$$\mathbf{R}_i = \begin{Bmatrix} F_i^M \\ F_i^K \\ F_i^S \end{Bmatrix} \tag{4.9}$$

where F^M, F^K, and F^S identify the three boundary layer governing equations (3.1)-(3.3).

The mass defect m does not appear directly in the equations, making it non-trivial to compute the Jacobian with respect to m. Instead the derivatives are taken with respect to the edge velocity U_e and to the mass defect thickness δ^* and these are use to construct the derivative with respect to m

$$\frac{\partial \mathbf{R}_i}{\partial m_j} = \frac{\partial \mathbf{R}_i}{\partial \delta^*_{i-1}} \left(\frac{\delta_{i-1,j}}{U_{e_{i-1}}} - \frac{m_{i-1}}{U^2_{e_{i-1}}} D_{i-1,j} \right) + \frac{\partial \mathbf{R}_i}{\partial \delta^*_i} \left(\frac{\delta_{i,j}}{U_{e_i}} - \frac{m_i}{U^2_{e_i}} D_{i,j} \right) +$$
$$+ \frac{\partial \mathbf{R}_i}{\partial U_{e_{i-1}}} D_{i-1,j} + \frac{\partial \mathbf{R}_i}{\partial U_{e_i}} D_{i,j} \qquad (4.10)$$

$\delta_{i,j}$ is the Dirac delta function.

4.2.1 System Solution

The boundary layer linearized system matrix is assembled for the entire domain. However, the off-diagonal influence terms in the matrix corresponding to points in the areas near the intersections of the appendages with the hull can results in a ill-conditioned system that can preclude convergence. The boundary layer formulation as it is used here is not able to resolve highly three-dimensional flows, like the ones that happen at the appendage-hull juctions, so it was decided to solve the linearized system in three separate patches: hull and its wake, keel and its wake and rudder and its wake. This way the influence terms between patches are ignored. The global influence is mantained when computing the equivalent inviscid potential due to the viscous sources, once the solution of the boundary layer equations has converged.

4.3 Initial Conditions

In 4.2 it is shown how the discretized equations at any point depend on the values at the point itself and at its upstream neighbor. However the values of all primary variables need to be initialized at the first point on the computational line. Because the routine that calculates the initial guess as well as the Jacobian and residual during the iterative process uses the edge velocity U_e and the mass defect thickness δ^* as inputs instead of the mass defect m, initial conditions for former two are used. If the computational line is on the body, and the attachment point of the boundary layer is on either the leading edge of an appendage or on the bow, then the boundary layer

variables are determined using a 2-D Falkner-Skan similarity solution, therefore

$$C_\tau^{1/2} = C_{tr} \exp\left(-n_{crit}\right) \tag{4.11}$$

$$\theta = 0.38574\sqrt{\frac{s}{Re_\infty U_e}} \tag{4.12}$$

$$\delta^* = \frac{0.90694}{U_e}\sqrt{\frac{s}{Re_\infty U_e}} \tag{4.13}$$

$$U_e = U_{INV} \tag{4.14}$$

where $U(s)$ is the local streamwise velocity and C_{tr} is the threshold value for the TS wave amplitude for transitioning to the turbulent regime and is taken to be equal to 0.01.

On the wakes instead the values of the boundary layer variables are determined by their values at either the stern or on the trailing edges of the appendages. At the stern of boat there are two computational points that represent the same physical point, then the values on the body are copied onto the wake

$$U_{e_\text{stern}} = U_{e_\text{wake}} \tag{4.15}$$

$$C_{\tau_\text{stern}}^{1/2} = C_{\tau_\text{wake}}^{1/2} \tag{4.16}$$

$$\delta^*_\text{stern} = \delta^*_\text{wake} \tag{4.17}$$

$$\theta_\text{stern} = \theta_\text{wake} \tag{4.18}$$

At the trailing edge of the appendages, the convergence of two separate boundary layers, one from the port surface, and one from the starboard one, must be considered. However the wake boundary layer is computed as a single viscous layer that is convected downstream in the direction of the velocity vector. Therefore the two layers need to be combined into one. At the trailing edge there are three computational points representing the same physical position (see Fig. 4-1). The primary variables are updated as follows

$$C_\tau^{1/2W} = \frac{C_\tau^{1/2P}\theta^P + C_\tau^{1/2S}\theta^S}{\theta^P + \theta^S} \tag{4.19}$$
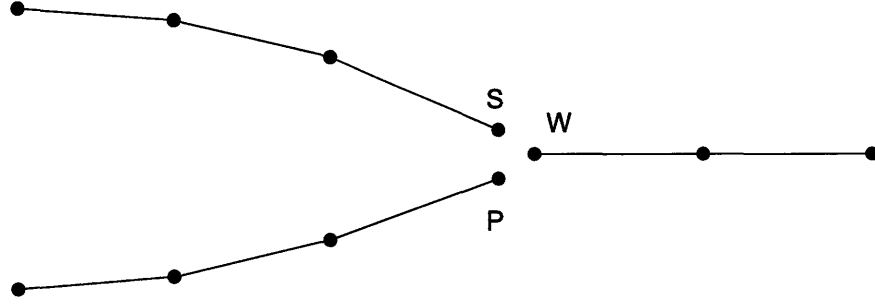
Figure 4-1: Computational point arrangement at the TE.

$$\theta^W = \theta^P + \theta^S \tag{4.20}$$

$$m^W = m^P + m^S \tag{4.21}$$

The last equation above needs to be transformed into equations for the mass defect thickness and for the edge velocity as the Jacobian and residual computation require these latter quantities to be used instead of the mass defect. Eq. 4.21 is equivalent to

$$\delta^{*W} = \delta^{*P} + \delta^{*S} \tag{4.22}$$

$$U_e^W = \frac{U_e^P \delta^{*P} + U_e^S \delta^{*S}}{\delta^{*P} + \delta^{*S}} \tag{4.23}$$

4.4   Solution Update

The iterative solution starts with an initial guess. The boundary layer is first marched in a standard "direct" mode with the prescribed edge velocity, taken to be the inviscid velocity from the double body flow solution. In case separation were to occur, a plausible value of the kinematic shape parameter H_k is prescribed until reattachment occurs. The accuracy of this initial solution influences the speed at which the method will converge. However, often for the first few iterations the solution needs to be under-relaxed to prevent oscillations, or even divergence, in the solution. Once the linear system is solved, the computed correction is compared to the current values of the variables, and the relaxation factor is calculated. The maximum correction allowed is 50% of the current value. With the relaxed values found, the solution is updated. However, before going to the next iteration, values of the variables are

56
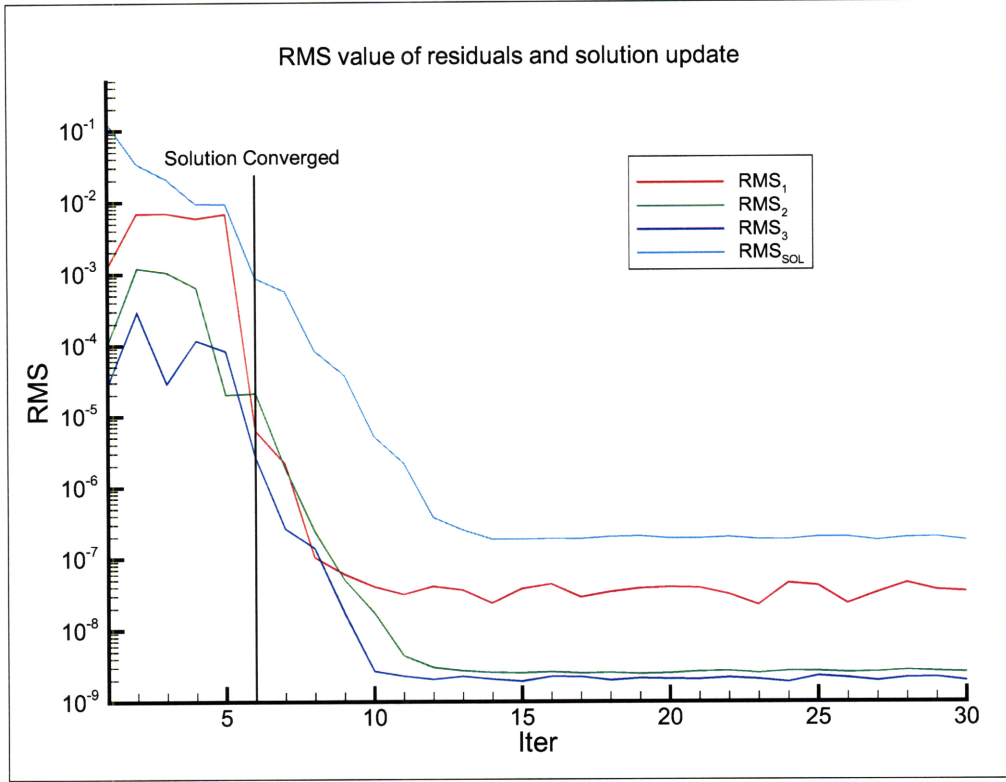
Figure 4-2: RMS values for the residuals and the change in solution after each iteration.

checked to make sure they are reasonable: the displacement thickness is limited by the value of the momentum thickness, so that the shape parameter H is above unity. After this check is done the mass defect values are updated using the definition (Eq. 3.5).

4.5   Solution Convergence

In all iterative processes a criterion needs to be established that defines when the solution has converged. During the update step of the iteration the root mean square (RMS) value of the relative change of the primary variables is computed. This is defined as

$$RMS_{Sol} = \sqrt{\sum_{i=1}^{4} dN_i^2 / NT} \qquad (4.24)$$

57
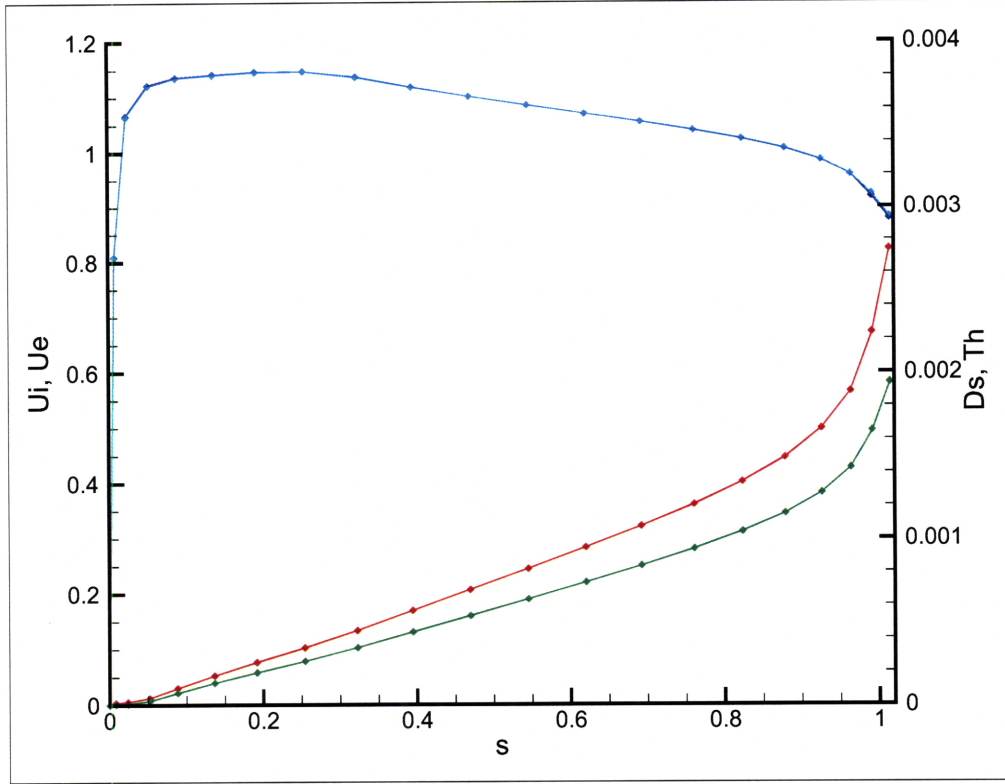
Figure 4-3: Streamline solution after 6 (symbols) and after 30 iterations (lines).

and

$$dN_1 = \begin{cases} \frac{\Delta C_\tau}{10.0} & s < s_{tr} \\[2mm] \frac{\Delta C_\tau}{C_\tau} & s \geq s_{tr} \end{cases} \tag{4.25}$$

$$dN_2 = \frac{\Delta \delta^*}{\delta^*} \tag{4.26}$$

$$dN_3 = \frac{\Delta \theta}{\theta} \tag{4.27}$$

$$dN_4 = \frac{\Delta U_e}{4 U_\infty} \tag{4.28}$$

where s_{tr} represents the point where the boundary layer transitions from a laminar to a turbulent regime.

To make sure that the implementation of the Newton system had been done correctly, it was first let run for 30 iterations, while monitoring the RMS values of both solution change and residuals. Fig. 4-2 shows that, as expected, the RMS value of the residuals went quickly down to the machine limit, then hovered around the same value for the

remainder of the iterations. RMS_{Sol} follows a very similar behavior, although at a lower speed. A RMS for the solution of 10^{-3} means that the mean square change in the state of the boundary layer quantities is 0.1%. This was found usually to correspond to a RMS value for the residuals of the three equations of the order of 10^{-6}-10^{-7}, so it was accepted as a limit for the solution to be considered converged. Figure 4-3 plots the solution for one computational line after 6 iterations against the solution obtained after 30 iterations: there is no visible difference.

Chapter 5

Numerical Validation

In this chapter numerical results are presented to validate the inviscid flow solution and the boundary layer solution in the current method separately.

5.1 Inviscid Flow Solution

Two geometries were used for the validation of the linear inviscid solution: the first is a Wigley hull, while the second is the canoe body of a sailing yacht (US Sailing Model 5) tested by US Sailing in the towing facility at the then Institute for Marine Dynamics (IMD), now Institute for Offshore Technology (IOT), in St. Johns, NL, Canada [2].

5.1.1 Wigley Hull

The surface of the Wigley hull is defined as

$$y = \pm \frac{1}{2} B \left[1 - \left(\frac{x}{\frac{1}{2}L} \right)^2 \right] \left[1 - \left(\frac{z}{D} \right)^2 \right] \qquad (5.1)$$

where B, L, and D denote respectively the beam, length, and draft of the hull. The values used in the computation for the length-beam ratio and for the length-draft
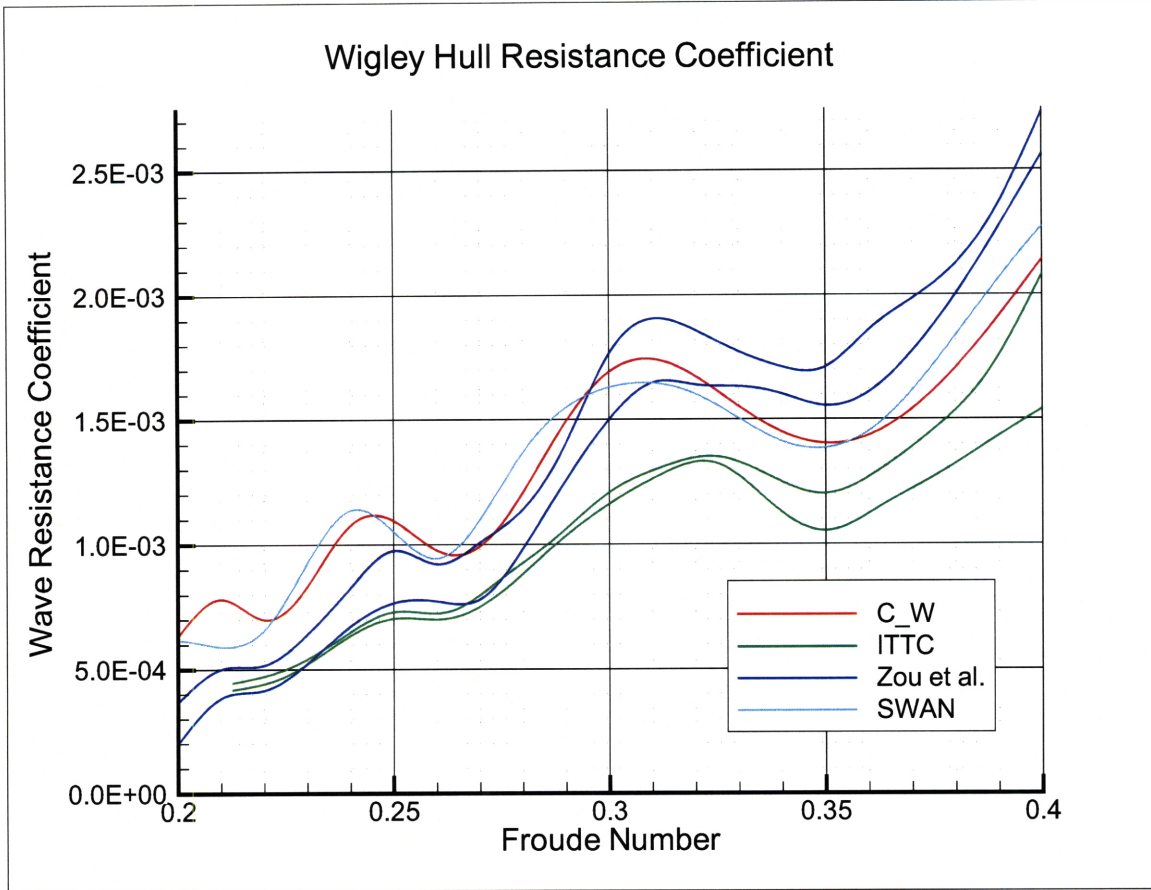
Figure 5-1: Wave resistance coefficient for a Wigley hull.

ratio are

$$\frac{L}{B} = 10$$
$$\frac{L}{D} = 16$$

If S is the static wetted surface and R_W is the wave resistance, the wave resistance coefficient is defined as

$$C_W = \frac{R_W}{\frac{1}{2}\rho U_\infty^2 S} \tag{5.2}$$

The wave resistance, which for on-lifting cases coincides with the pressure resistance, is found by integrating the pressure field on the hull, obtained from the linear inviscid

solution by the use of Bernoulli's equation

$$p = -\rho \left[\frac{1}{2} \nabla \phi_{DB} \cdot \nabla \phi_{DB} - \frac{1}{2} U^2 + gz \right] + \rho \left[\nabla \phi_{DB} \cdot \nabla \psi + \frac{1}{2} \nabla \psi \cdot \nabla \psi \right] \qquad (5.3)$$

In cases where lift is produced, the pressure drag will include not only the wave drag, but also the induced drag and the form drag, the latter when viscous effects are also accounted for. The definition of pressure resistance is not as straightforward as it seems: both Nakos and Sclavounos [18] and Raven [24] give a detailed explanation of how two different and therefore inconsistent definitions of wave resistance can be obtained in the case of the Neumann-Kelvin formulation whether one starts from the pressure integration or from energy balance. Since in the current method the free-surface boundary conditions used are the same Kring developed for SWAN, it was decided to also use the same method for the wave resistance calculation, which is to integrate the pressure over the underbody [28], as this has been extensively tested in SWAN.

The hull was tested in fixed static trim in a range of Froude number between 0.2 and 0.4. Fig. 5-1 shows the results from the current method using a 40 x 6 x 30[1]grid and compares them to the experimental results obtained by Zou et al. [32], with measurements taken by Norrbin [22] for the International Towing Tank Conference, and with computational results obtained by Nakos [18] using SWAN. The solution found with the current method is very similar to the computational results obtained with SWAN, and close to the experimental results of Zou et al..

A grid convergence test was done using three different grids about the same range of forward speeds (Fr = 0.2-0.4): Fig. 5-2 shows that the wave resistance coefficient does not change significantly with grid refinements.

Fig. 5-3 compares the Kelvin wake computed using SWAN and the current method: the two wakes are very similar as for wave length and diverging wave angle.

In [24] Raven publishes a comparison for the wave profile along the Wigley hull for a

---

[1]The first number denotes the number of panels in the longitudinal direction, the second the number of panels in the transverse/vertical direction, and the third the number of panels on the free surface in the radial direction
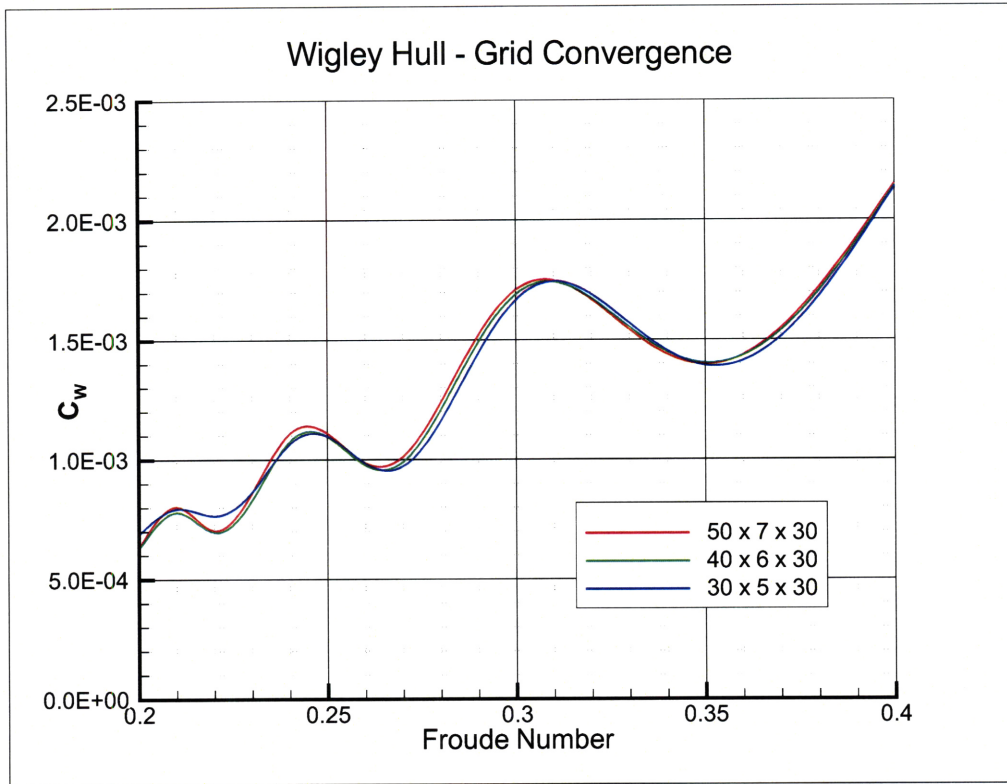
Figure 5-2: Wave resistance coefficient for a Wigley hull using different grids.
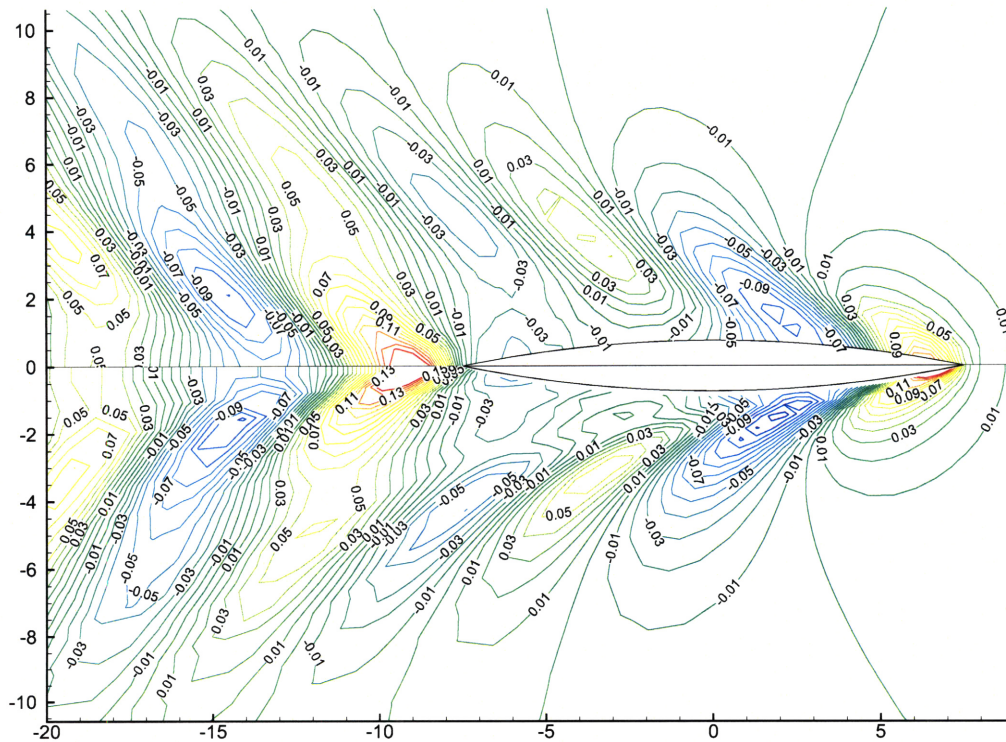
Figure 5-3: Kelvin wakes for a Wigley hull computed with SWAN (top half) and with the current method (bottom half).

	Model 5
Waterline Length, [m]	12.465
Waterline Beam, [m]	3.294
Canoe Body Draft, [m]	0.685
Canoe Displacement, [Kg]	9136
Canoe Wetted Area, [m^2]	38.651
Prismatic Coefficient,	0.543

Table 5.1: Full scale yacht dimensions.

Froude number of 0.316 between experimental measurements and the computational results he obtained using DAWSON, a linear panel method code, and using RAPID, the nonlinear evolution of the first. Two wave profiles computed with the current method are plotted in Fig. 5-4 against Raven's findings: the first is for a finer (F)grid (50 x 7 x 40), and the second for a coarser (C) grid (30 x 5 x 30). Both profiles agree well with the experimental results.

5.1.2   US Sailing Model 5

Model 5 is the parent model of a beam-to-draft variation series of hulls tested by US Sailing in order to acquire experimental data to improve the resistance model in the IMS Velocity Prediction Program, used to determine the racing ratings for sailing yachts. The models tested are all 1:2 scale models, with the main full scale dimensions given in Table 5.1.

Fig. 5-5 shows the computed wave resistance coefficient along with the one calculated from the experimental results for three different grids. The values agree well and are within the uncertainty of the expansion of the tank data.

5.2   Boundary Layer Solution

The boundary layer solution computed with the present method was validated against PAN2D-BL, a two-dimensional code developed by Hufford [10] for the analysis of marine propellers. Two different symmetric airfoil shapes, a NACA 0010 and a NACA
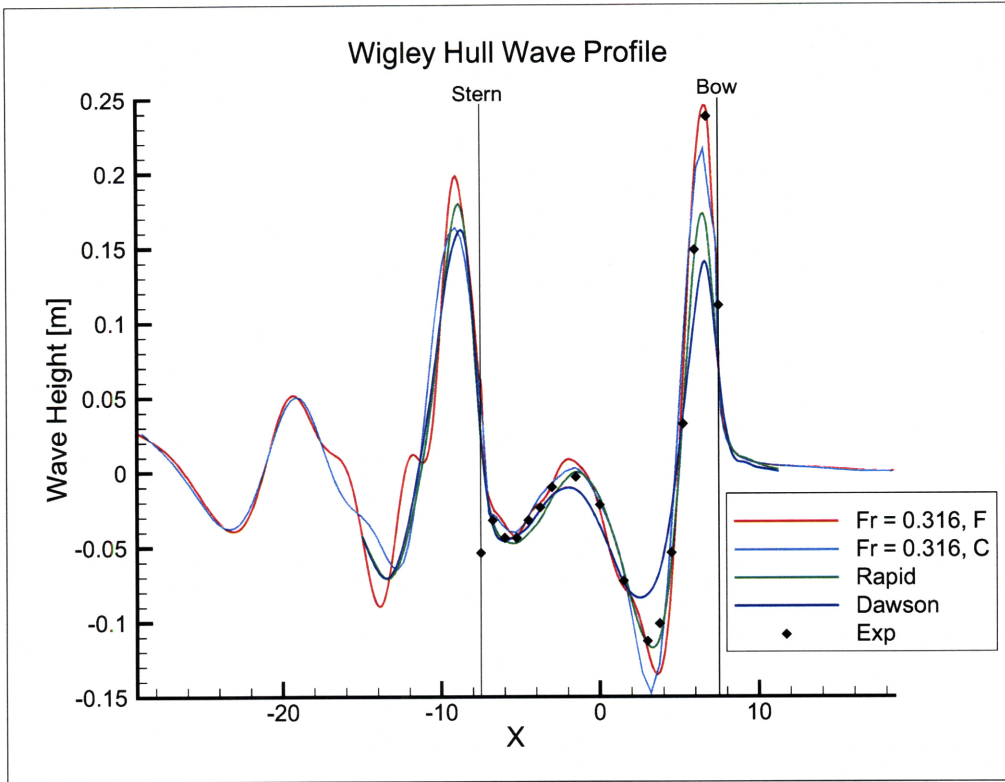
Figure 5-4: Wave profiles for a Wigley hull using a fine (F) and coarse (C) grid.
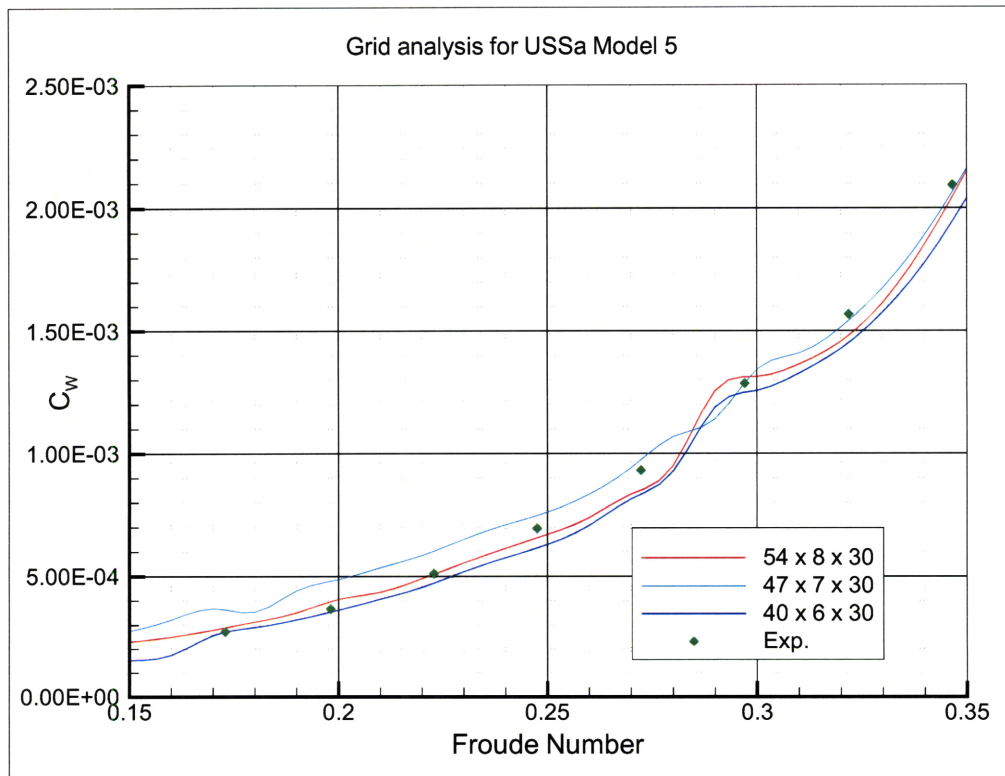
Figure 5-5: Computed and experimental wave resistance coefficient for Model 5.
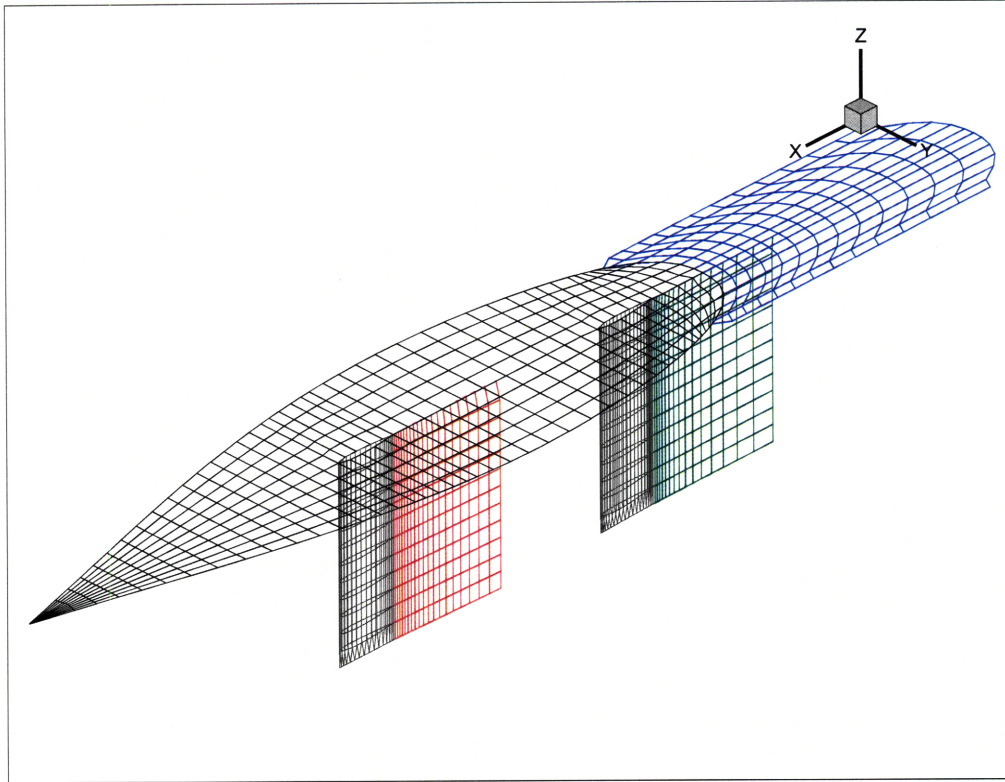
Figure 5-6: Grid used to validate the boundary layer solution.

0015, where run at two different angles of attack each. To come as close as possible to a two-dimensional solution with the present method, a peculiar geometry was developed: the Model 5 hull was scaled down in depth so that the maximum draft is less than 0.001 m, while length and beam are kept constant (see Fig. 5-6). This was done to minimize the effects of the free surface on the solution. Then a keel and rudder with the desired airfoil section are fitted to the hull, both with a chord length of 1.0 m and a span of 3.0 m.

5.2.1 NACA 0010 Airfoil

The choice of symmetric shape was given by the fact that the appendages of sailing yachts are symmetric, except for the rare occasions. A NACA 4-digit series is a very reasonable choice of section for an appendage, either fin keel or spade rudder, and a thickness-chord ratio of 10% is close to the lower end of the range for the thickness of a keel.

The tests were run at unit inflow speed, and with a Reynolds number Re of about 10^9. The transition was forced at $x = 0.1$. The PAN2D-BL geometry had 61 points on the foil and 20 on the wake, while the current method used 61 points on the airfoil and 18 on the wake. The solution at $0°$ of angle of attack reported here is taken at midspan on the keel, while the one at $2°$ is taken on the rudder, with the rudder angle set equal to the desired angle of attack.

For the non-lifting case (Fig. 5-7 top), the velocity profile along the foil matches very well the profile from PAN2D-BL. The small differences near the leading edge were initially thought to be due to the different distribution of the computational points. However it was found that because the two programs generate the geometry in two different ways (PAN2D-BL has an internal NACA 4-digit generator, while the current method generates the geometry from a NURBS surface) there is a small difference in the shape of the foil itself. As Fig. 5-8 shows, the leading edge is more round in PAN2D-BL than in the current method; The difference is even greater for the NACA 0015 airfoil discussed in the next section. This explains the difference in inviscid velocity too. The mass defect thickness δ^* and the momentum thickness θ come in very good agreement between the two programs.

The geometry mismatch magnifies the differences in the lifting case (Fig. 5-7 bottom), although the agreement is still more than satisfactory. Both the inviscid and edge velocity are underestimated near the leading edge on the suction side of the foil, however the boundary layer quantities δ^* and θ computed with the present method fall right on top of those computed with PAN2D-BL.

5.2.2   NACA 0015 Airfoil

A 15% thick airfoil section is often used for rudders with short chordlength, where the thickness is needed in order to fit a strong enough rudder stock. Again the airfoil is tested at two angles of attack, only this time $4°$ is used instead of $2°$. The grid resolution is the same as before as well as the location of the forced transition to turbulent regime.

The top of Fig. 5-9 shows the non-lifting case: the agreement of the velocity profiles
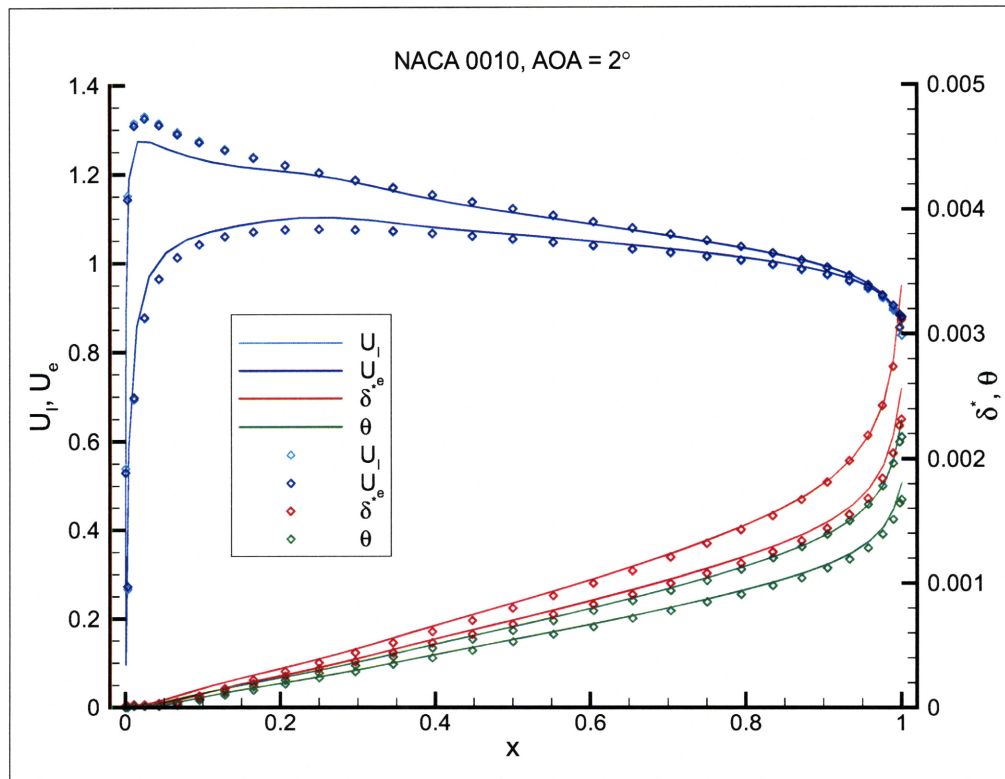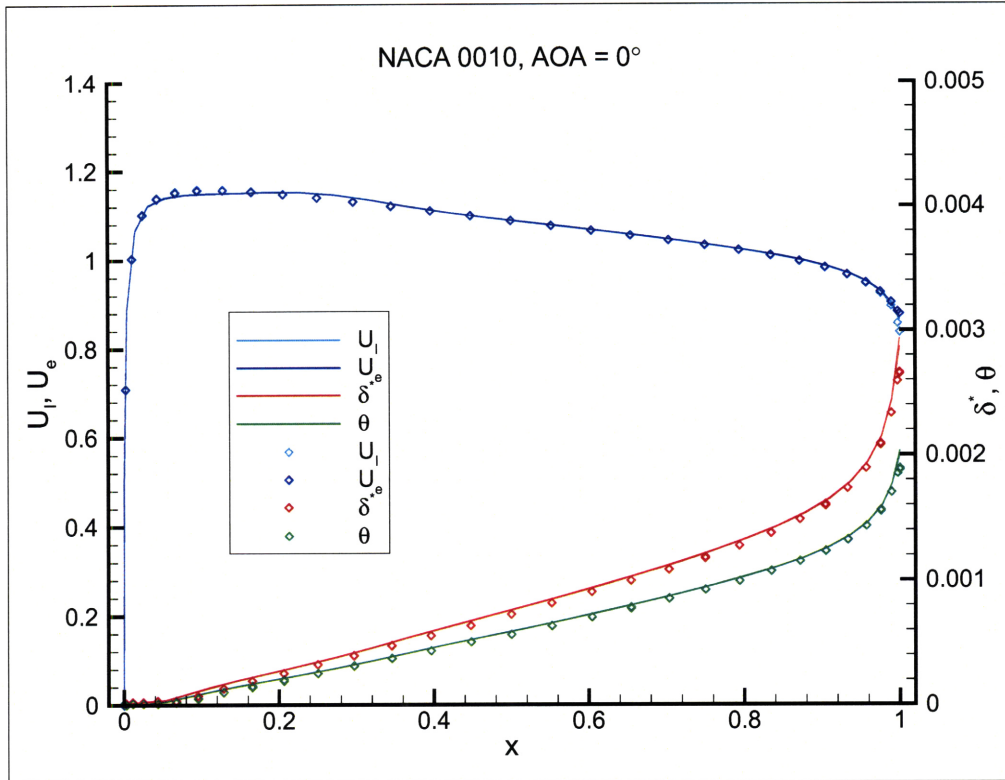
Figure 5-7: Solution comparison between the current method (solid lines) and PAN2D-BL (symbols) for a NACA 0010 airfoil, at an angle of attack of 0° (top) and 2°.
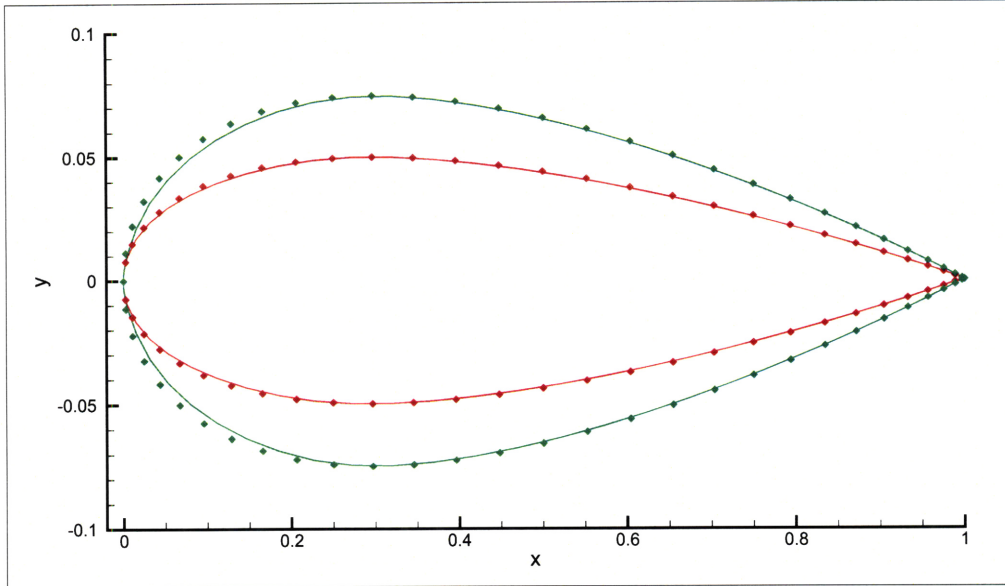
Figure 5-8: Airfoil shape comparison between the current method (solid lines) and PAN2D-BL (symbols) for NACA 0010 and 0015 airfoils

is still reasonably good, considering that for this foil the difference in shape of the nose is more pronounced than in the previous one. The agreement of the boundary quantities is actually very good.

In the lifting case (Fig. 5-9 bottom), the shape mismatch causes the velocity profiles to differ somewhat, in particular near the leading edge on the suction side of the foil. For the pressure side of the foil the results show a better agreement between the two programs. Despite this, the solution for the boundary layer quantities repeats reasonably well.

5.2.3 Resolution Study

The NACA 0010 airfoil was also used to study the effects of the grid resolution on the boundary layer solution. This was done using three different grids: the coarse mesh has 33 total points distributed over the entire foil section, the medium grid has 47 points, while the fine mesh had 61 points. The conditions for the runs were the same as above ($U = 1.0$, $x_t r = 0.1$). As Fig. 5-10 shows, the solutions lay on top of each other over most of the chordlength, with appreciable differences only close to the trailing edge.
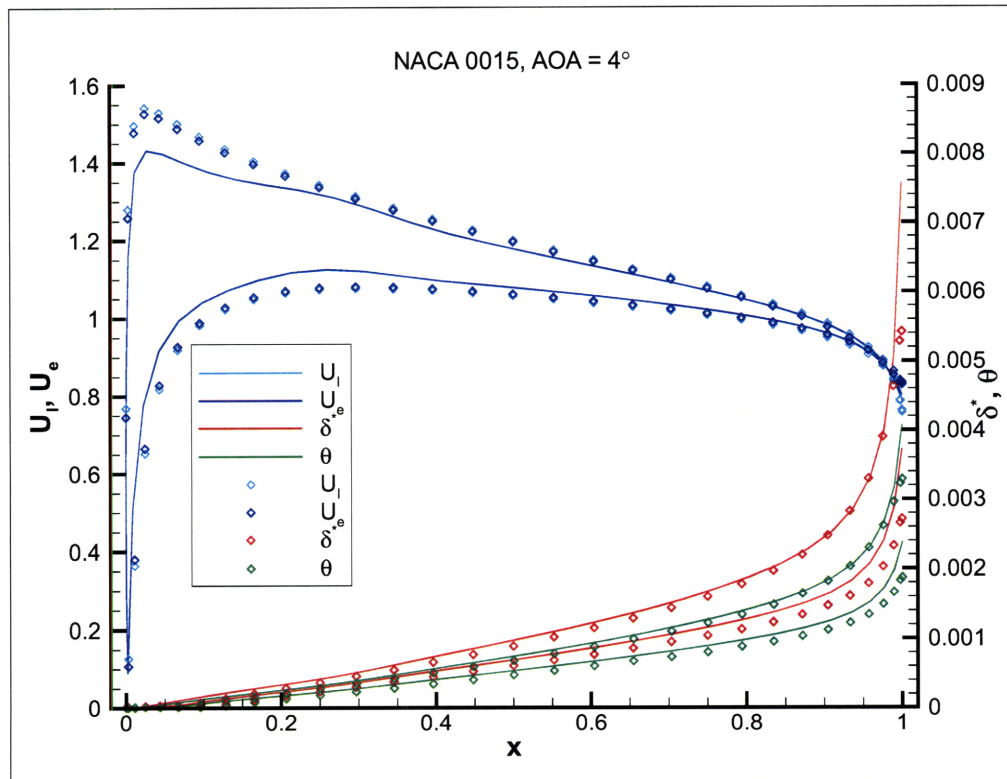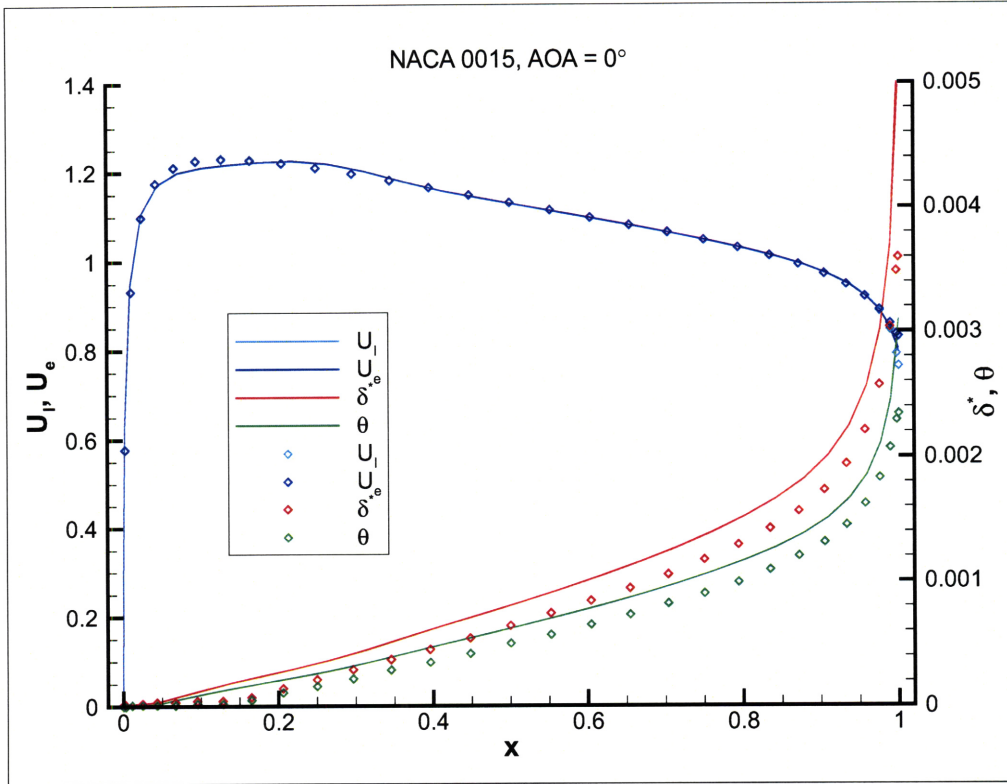
Figure 5-9: Solution comparison between the current method (solid lines) and PAN2D-BL (symbols) for a NACA 0015 airfoil, at an angle of attack of 0° (top) and 4°.
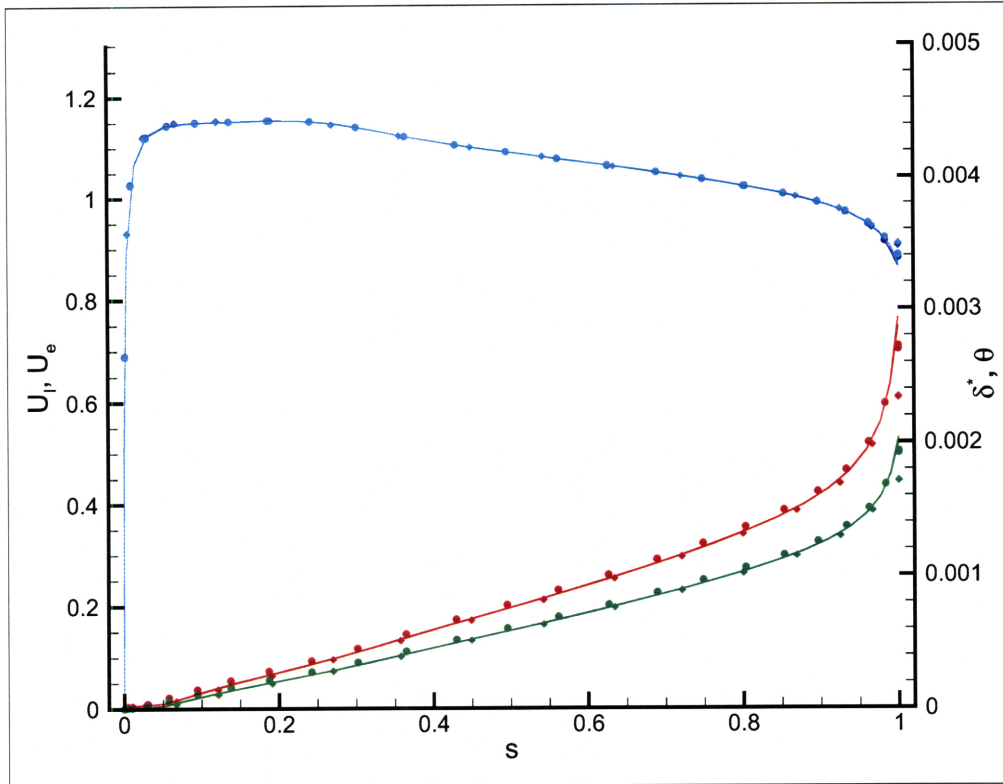
Figure 5-10: Solution comparison between the coarse grid (diamonds), the medium grid (circles) and the fine grid (solid lines).

A second resolution study was conducted using the canoe body of US Sailing Model 5, in order to check the effects on a three-dimensional geometry run at speed and Reynolds number compatible with actual sailing conditions. The hull was run at a speed of 2.75 m/sec, which corresponds to a Froude number of 0.25. The dimensions of the grids used are:

(C): coarse grid with 35 points in the longitudinal direction and 11 in the transverse;

(M): medium grid with 41 points in the longitudinal direction and 13 in the transverse;

(F): fine grid with 47 points in the longitudinal direction and 15 in the transverse;

(VF): very fine grid with 53 points in the longitudinal direction and 17 in the transverse.

Even in the three dimensional cases the results are very similar between all the grids: the finer the grid the better they capture the drop of the inviscid velocity at the stern of the boat. This in turns affects the value of the edge velocity at the stern, and therefore of the mass defect and momentum thicknesses δ^* and θ. However the differences are less pronounced between the (F) and the (VF) grid than they are in the other cases (see Fig. 5-11 to 5-14).
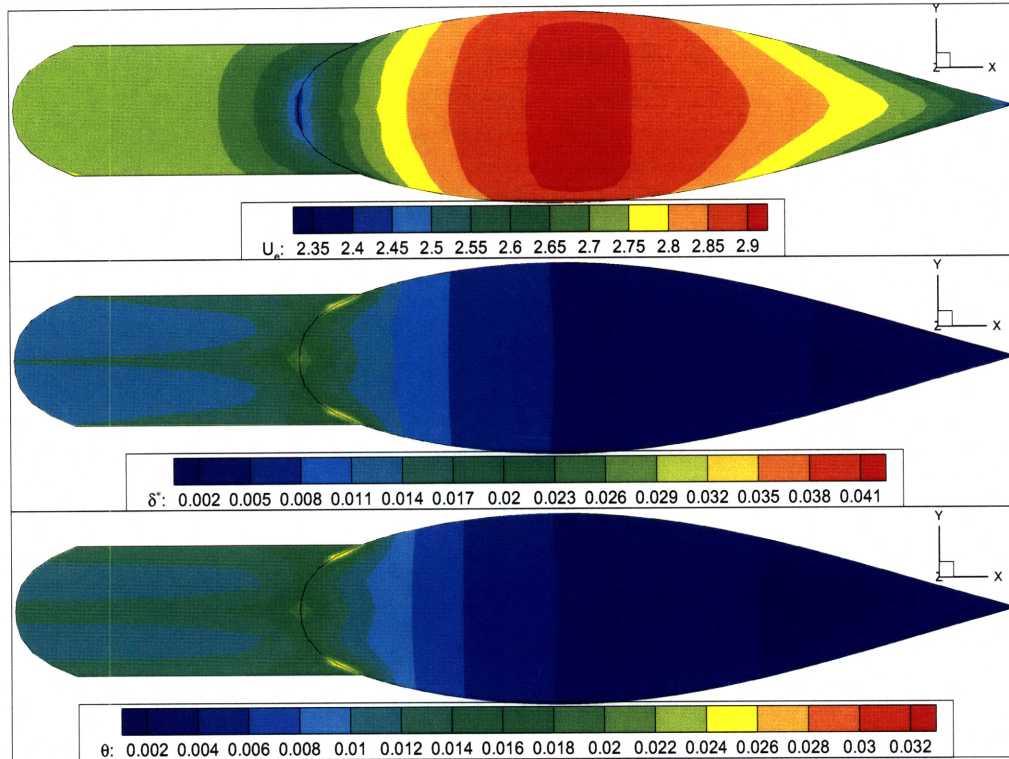
Figure 5-11: Viscous solution for Model 5 on the coarse (C) grid. The top frame is a contour plot of the edge velocity, the middle of δ^*, the bottom of θ.
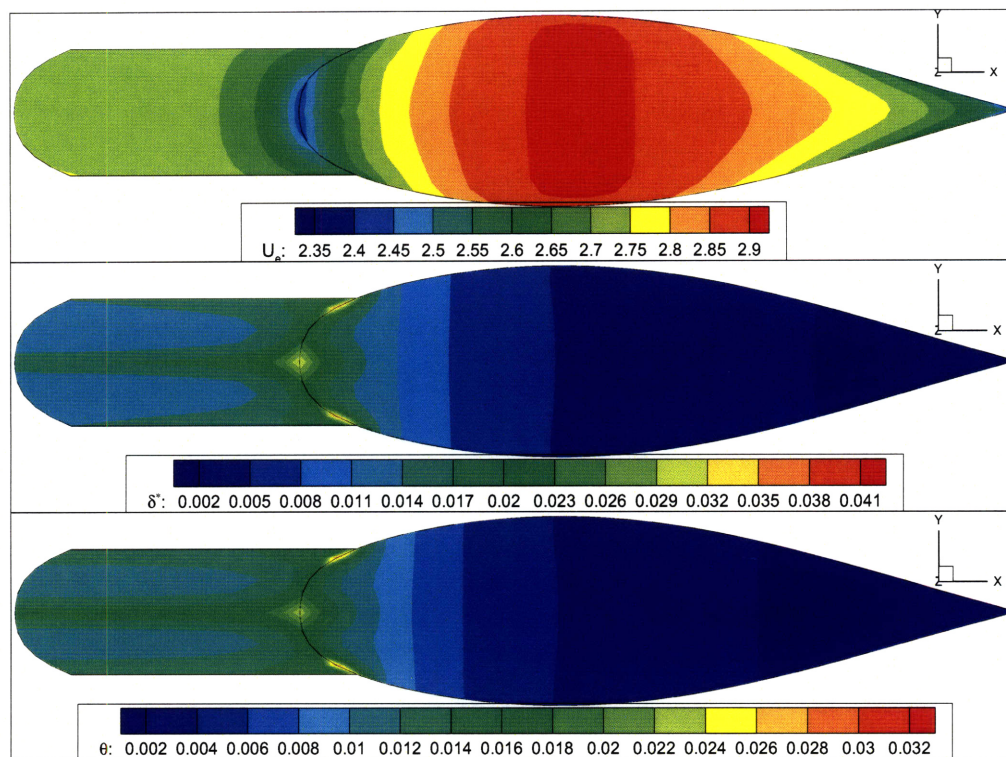
Figure 5-12: Viscous solution for Model 5 on the medium (M) grid.
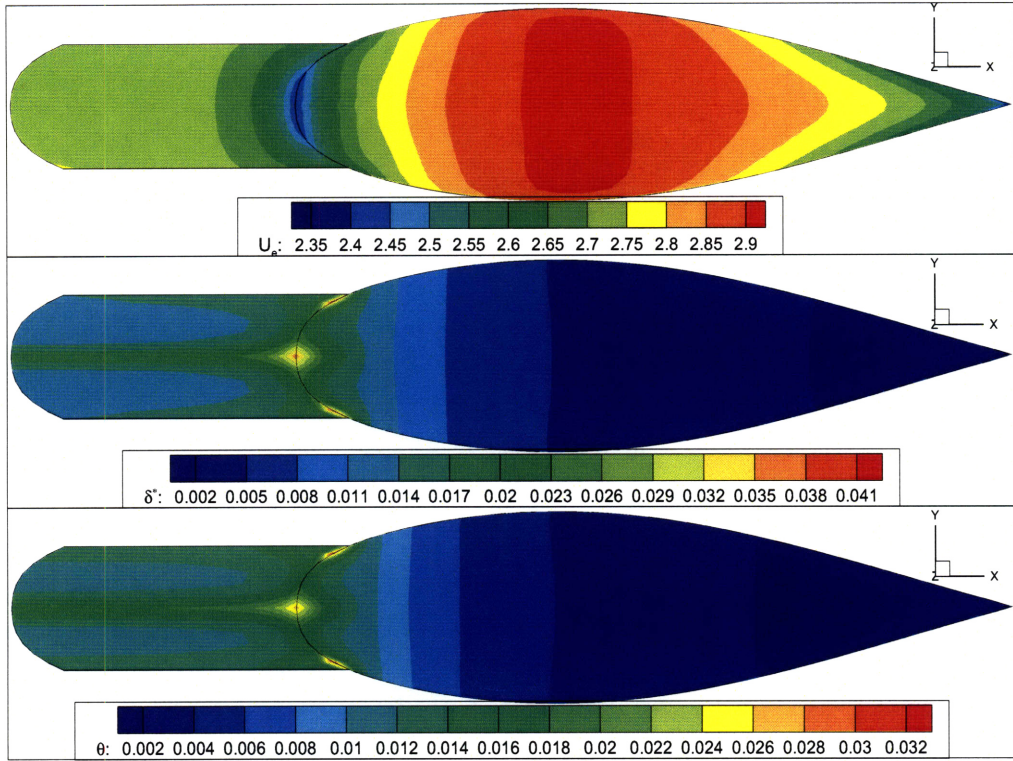
Figure 5-13: Viscous solution for Model 5 on the fine (F) grid.
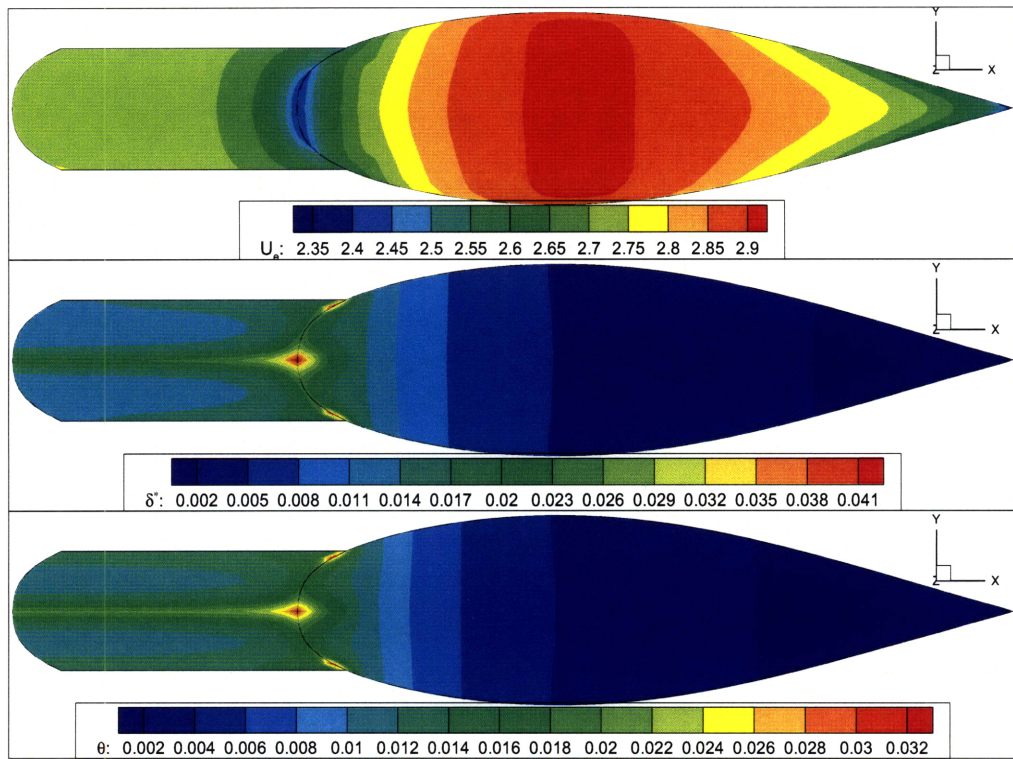
Figure 5-14: Viscous solution for Model 5 on the very fine (VF) grid.

Chapter 6

Results

In this chapter the numerical procedure developed is tested, first using a canoe body without appendages, then using a complete hull, so that predictions of both lift and drag can be verified.

6.1 Experimental Data

The numerical results are compared with experimental data obtain at the towing tank at the Institute for Offshore Technology (IOT) in St. Johns, Newfoundland, Canada. The model data was expended to full scale by the author. The procedure is described full detail in [2]. It estimates the frictional resistance of the model by using a frictional coefficient computed with a Reynolds number based on 70% of the waterline length. This method was used because it is the method used by the IMS VPP, the object of the investigation in [2]. An alternative method uses the frictional coefficient based 100% of the waterline length, and then multiplies the resistance by a form factor. The form factor is usually determined by a Prohaska plot done using the upright runs at low Froude number. This value is then used for all the runs in a test matrix. However the low speed runs are the least reliable in towing tank experiments because of the high probability that the turbulence stimulation on the appendages and on the hull fails.

Method	Frict. Drag [N]	Resid. Drag [N]	Total Drag [N]
70% LWL	624.1	200.9	825.0
$1 + k = 1.00$	600.2	231.4	831.6
$1 + k = 1.05$	620.7	207.3	828.0
$1 + k = 1.10$	641.2	183.3	824.5

Prohaska Plot

$y = 52.394 x + 1.0546$
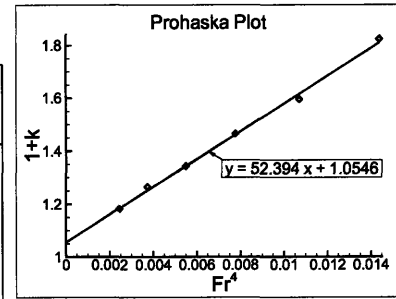
Table 6.1: Prohaska plot and data expansion table.

When model scale data is expanded to full scale, the frictional drag of the model is estimated using one of the method described above and subtracted from the total drag to find the residuary drag. The residuary resistance coefficient is the same for the model and the full scale boat, so the full scale residuary drag can be found. The full scale frictional is estimated using the same method.

The full scale total drag changes only by about 0.8% depending on the method used, however the balance between the frictional and the residuary resistance is greatly affected by the expansion procedure used, so much that the latter has variations up to 23% as shown in Table 6.1. The plot next to the table shows the value of the form factor for Model 5, as it is calculated from the experiments. Therefore for the comparisons with numerical data, the total drag is considered the most important value.

6.2 Model 5 Canoe Body

The canoe body of Model 5 was tested at three different speeds and compared with the experimental results. The computations were done using the same fine grid defined in the previous chapter, a 46 by 14 panel grid, at Froude number of 0.25, 0.30, and 0.35, which correspond to full scale speeds of 2.75, 3.31, and 3.86 m/s. The velocities used are in the range in which a sailing boat of about 40 ft in overall length sails in a medium wind strength. Table 6.2 shows the computed and experimental forces. Although the current method tends to overpredict a little the residuary drag, while

Froude Number	Computation	Experiments
	Total Drag	Total Drag
0.25	356.5 N	391.7 N
0.3	614.9 N	649.9 N
0.35	1091.1 N	1055.2 N

Table 6.2: Numerical and experimental drag for Model 5 canoe body.
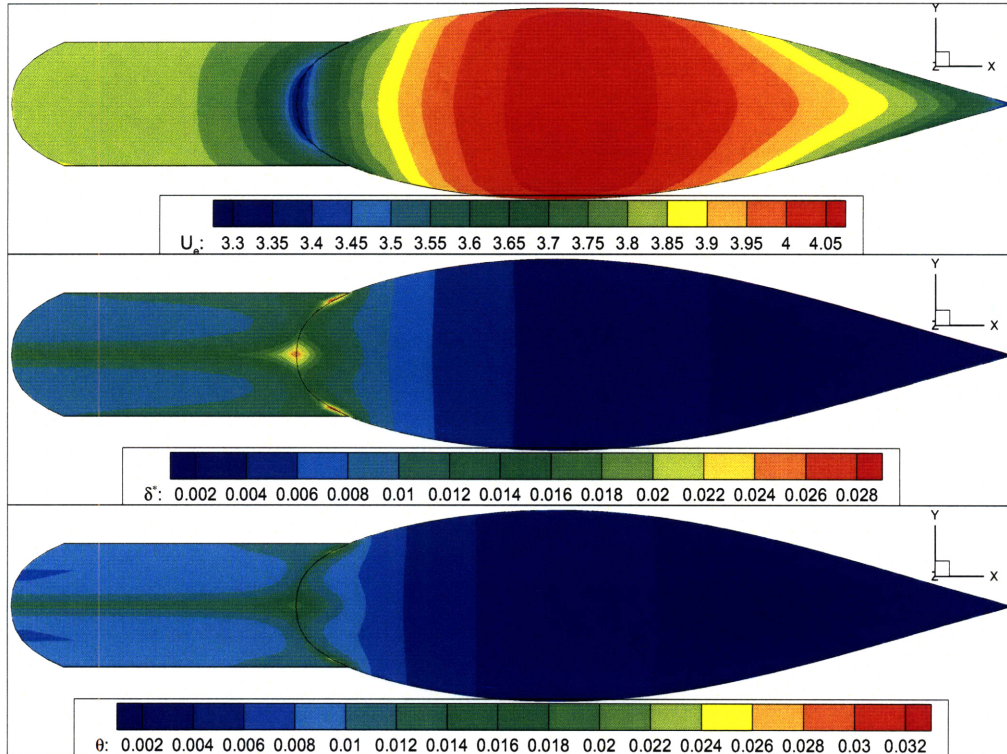
Figure 6-1: Boundary layer solution at $Fr = 0.35$. The top frame is a contour plot of the edge velocity, the middle of δ^*, the bottom of θ.

underpredicting the frictional resistance, in particular at the lower speeds, the total drag computed with the current method compares reasonably well to the experiments.

In all three cases the boundary layer computation converged pretty quickly, using at most 5 iterations. The final viscous solution for the first case was presented in the previous chapter in Fig. 5-13. Here the final solution for the case at $Fr = 0.35$ is shown in Fig. 6-1. It is possible to notice how the boundary layer grows very slowly over the forward half of the hull, where the streamlines are diverging and the velocity is increasing, and but then starts to grow much more quickly near the stern where the hull gets narrow and there is an adverse pressure gradient.
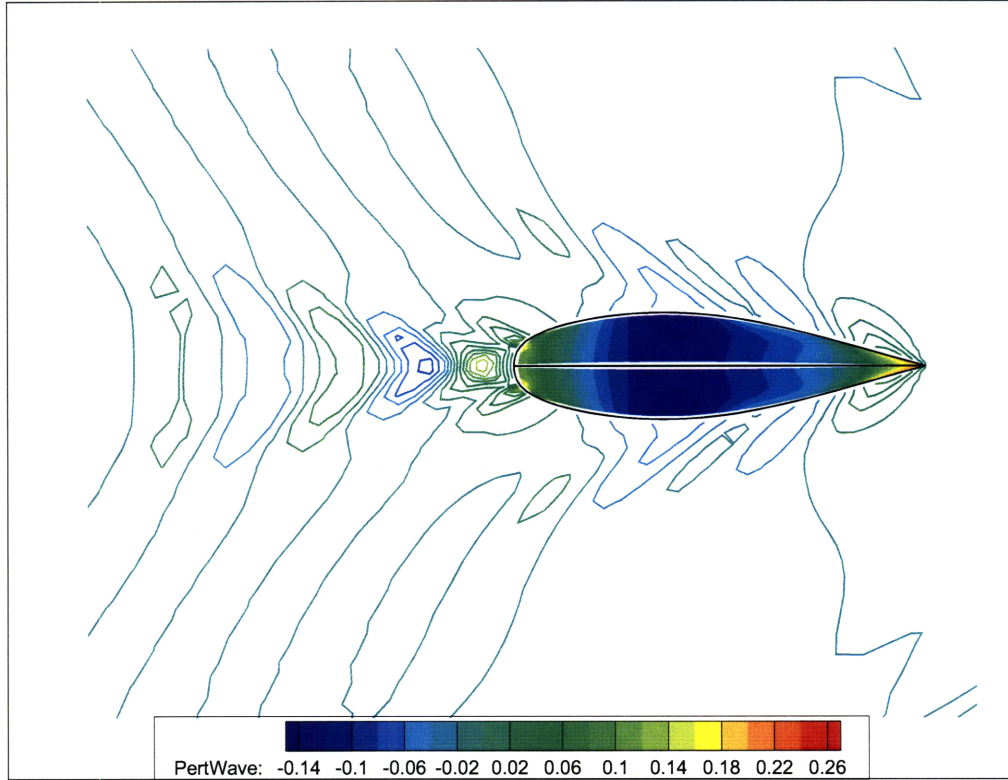
Figure 6-2: Wave pattern and pressure field for the canoe body at $Fr = 0.25$.

Figures 6-2 to 6-4 shows the wave pattern created by the hull. Comparing the three patterns, the increase in wave height and wave length off the waves coming off the stern with increasing Froude number are evident. It also shows how at the lowest speed the waves tend to be more of the transverse kind, while at the highest speed the diverging wave pattern becomes predominant. The contours drawn inside the hull boundary in the figure represent the pressure field computed on the body. Here, the areas of lowest pressure on the hull correspond to a deeper trough on the free surface. The pressure field is integrated to obtain the pressure resistance, also called residuary resistance by naval architects, while the frictional part comes from the integration of the frictional coefficient over the hull surface.

6.3   Aft End of Waterline Condition

As said before, sailing yachts are designed with relatively flat stern overhangs. The linearized flow solution does not have any information regarding the body geometry
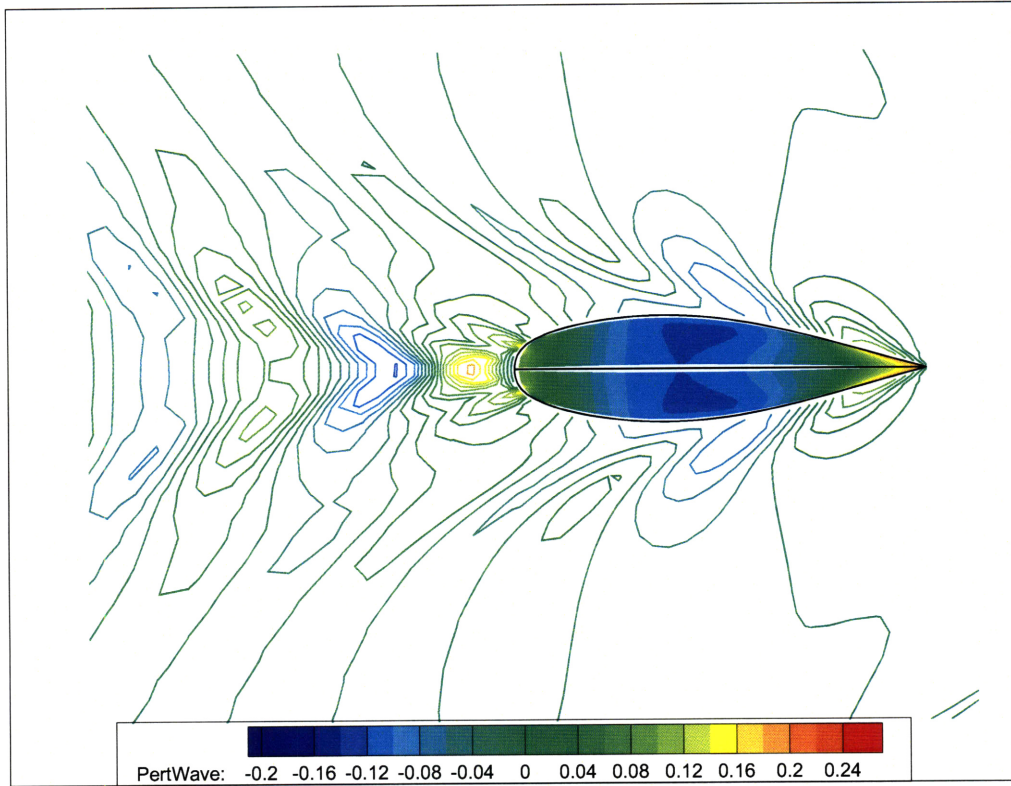
Figure 6-3: Wave pattern and pressure field for the canoe body at $Fr = 0.30$.
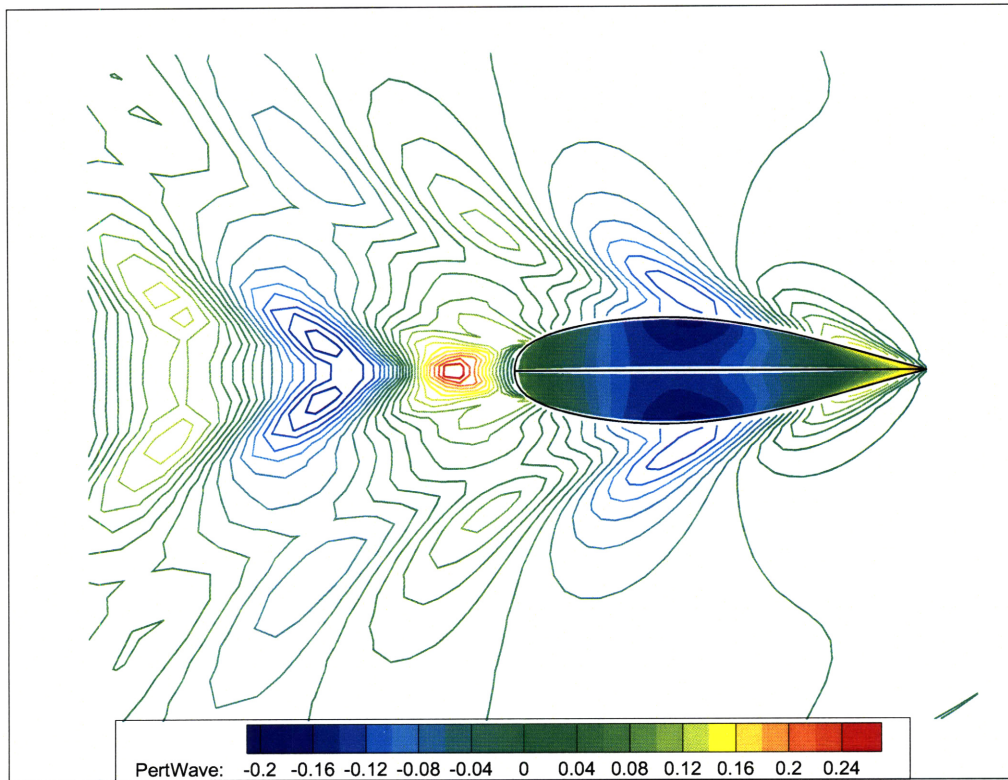
Figure 6-4: Wave pattern and pressure field for the canoe body at $Fr = 0.35$

above the static waterline, therefore it is necessary to impose conditions at the stern end of the waterline that ensure a zero wave height and a smooth detachment from the underbody. This condition is very similar to that used for transom sterns of ships when sailing at high speeds. However, with a sailing yacht the situation is made more complicated by the fact that there are no well defined edges of the "transom" inside of which to apply such conditions.

A criterion to determine these edges of the area of the free surface where the condition is imposed was based on the angle of the tangent to the waterline with respect to the centerline. The limiting angle changes with the speed of the vessel and with the heel angle. The reasoning behind it was that with increasing speed the water flow tends to come off the stern more straight and tends to wrap around the stern less. Also with increasing speed, the wave at the stern affects a wider area. The actual numbers were determined empirically by running a model hull at different speed and heel angles and extending the edge of the "transom" so that no unreasonably high waves formed just outside the edge of the area where the condition was imposed.

Eq. 2.10 gives the analitycal condition to be imposed on the free surface points along the aft end of the waterline. This condition is imposed numerically by setting the wave height on the points on the first two rows of the free surface that are within the limits previously found accordingly to the slope of the overhang. Each point on the free surface has two unknowns, the wave height and the linear perturbation potential, but instead of using two equations to impose both the height and slope of the wave at the first point, setting the wave height at two points was thought easier to implement and also it extends the influence of the overhang a little further aft. This was found to work reasonably well, although the resistance showed some sensitivity to the extent of the area on which the condition was imposed.

6.4   Model 5 Appended

The upright cases of the canoe body show good predictions for the total drag of the model, so the next step involves testing the complete boat. The canoe body was fitted

	Keel	Rudder
Root Chord, [m]	1.585	0.688
Tip Chord, [m]	1.056	0.328
Thickness, %	13.0	13.0
Span, [m]	2.450	2.239

Table 6.3: Model 5 appendage dimensions.

with trapezoidal profile shape keel and rudder. The dimensions of the appendages are given in Table 6.3.

Three series of tests at different sailing conditions were run:

Series A: upright, with no rudder angle, at $Fr = 0.25$, $Fr = 0.30$ and $Fr = 0.35$;

Series B: no heel, yaw and rudder angle equal to 1° and 2°, at $Fr = 0.25$, and equal to 2° at $Fr = 0.325$;

Series C: 10°, 15° heel, yaw and rudder angle equal to 2°, at $Fr = 0.25$.

6.4.1 Series A: Speed Variation

The purpose of this series is to test the prediction of forces as function of speed. Because of the more complicated geometry due to the presence of the keel and rudder, the boundary layer solution is slower in getting to full convergence taking now 11 iterations. The boundary layer on the hull converges almost as quickly as before, however to get the final solution on the appendages the process take more iterations. Fig. 6-5 show the final solution for the momentum thickness θ over the hull and appendages for the lower of the two speeds tested, and Fig. 6-6 shows the final values for the displacement thickness δ^* for the same case. Fig. 6-7 and 6-8 give the solution for the same boundary layer quantities at $Fr = 0.35$. The transition from laminar to turbulent flow occurs naturally on the hull at about 6% of the waterline length, while it is forced at 5% of the chordlength on the appendages. The tank model has turbulence stimulators at station 0.5 and station 1 (5% and 10% of the waterline length), so the transition on the hull probably happens a little upstream than in the model. On the appendages the turbulence stimulators were placed very close to the

		Residuary Drag	Frictional Drag	Total Drag	Error
Computation	$Fr = 0.25$	83.8 N	482.3 N	566.1 N	7.3%
	$Fr = 0.30$	269.0 N	653.9 N	922.9 N	10.6%
	$Fr = 0.35$	505.2 N	872.3 N	1372.5 N	4.6%
Experiments	$Fr = 0.25$	81.4 N	442.5 N	523.9 N	
	$Fr = 0.30$	200.9 N	624.1 N	825.0 N	
	$Fr = 0.35$	473.2 N	835.1 N	1308.3 N	

Table 6.4: Numerical and experimental drag for Model 5 with appendages for the Froude number series.

leading edge, at less than 5% of the chordlength. However, since the transition does not happen immediately, 5% was used in the computations. To check the sensitivity of the solution to the, one of the upright case was repeated with the transition location at 8% of the chordlength, and it was found that the effect on the drag was insignificant. Comparing the wave pattern for the appended boat (Fig. 6-9) at $Fr = 0.25$ with that of the canoe body only, it shows more pronounced waves. The trough near the midship section is deepened by the presence of the keel, which contributes to lowering the pressure in the middle section of the boat. This results in a higher wave at the stern. Fig. 6-9 shows the wave pattern and pressure field at $Fr = 0.35$. Again comparing it to the wave pattern of the canoe body, the waves here are bigger. The computed forces compare reasonably well with the experimental ones in the limit of the linearized problem. At the lower Froude number the pressure resistance compares very well, while the frictional resistance is slightly overpredicted by the current method, which gives a total drag higher than the experiments by 7.3% (see Table 6.4). At the higher Froude number the computational method does better as the difference in total drag is only 4.6%

6.4.2 Serie B: Yaw and Rudder Angle Variation

In this series the model was tested at a different non-zero yaw and rudder angle to compare the prediction of both hydrodynamic lift and drag. The case at the higher yaw and rudder angle was tested also at a second speed.
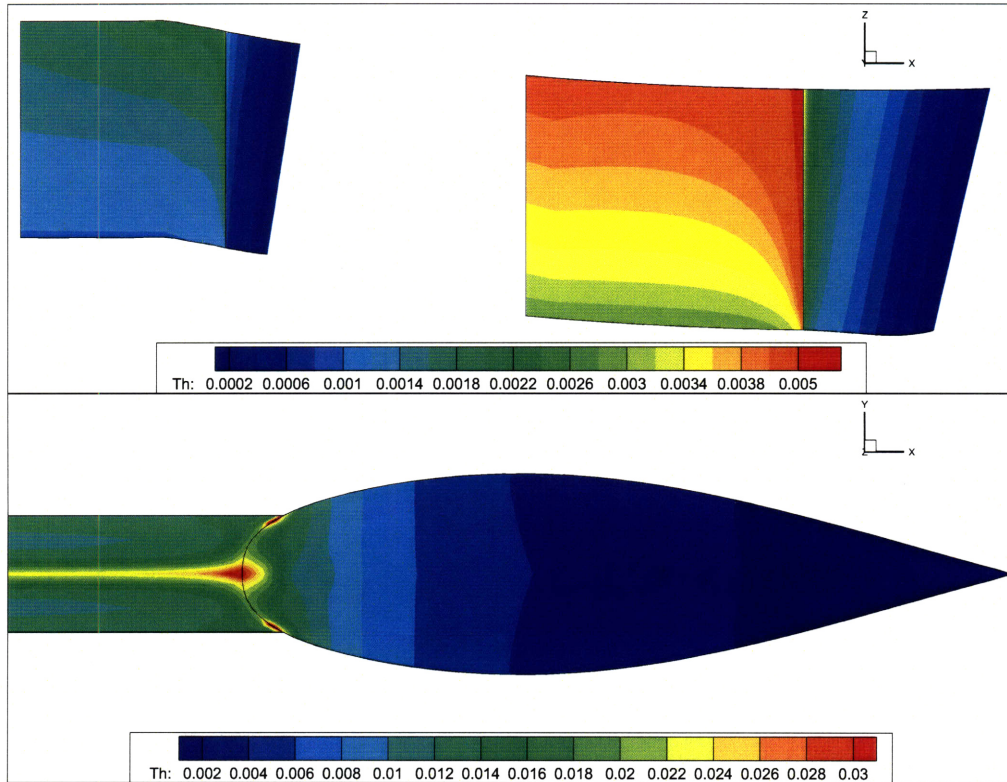
Figure 6-5: Momentum thickness solution θ for Condition A at $Fr = 0.25$.
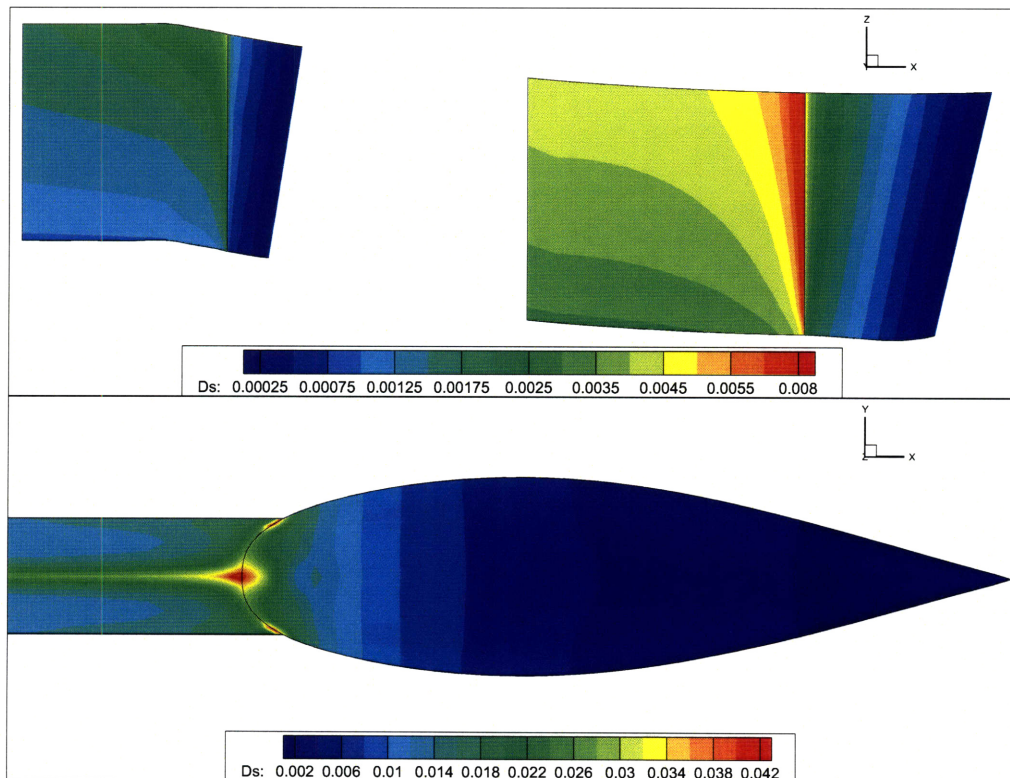
Figure 6-6: Displacement thickness solution δ^* for Condition A at $Fr = 0.25$.
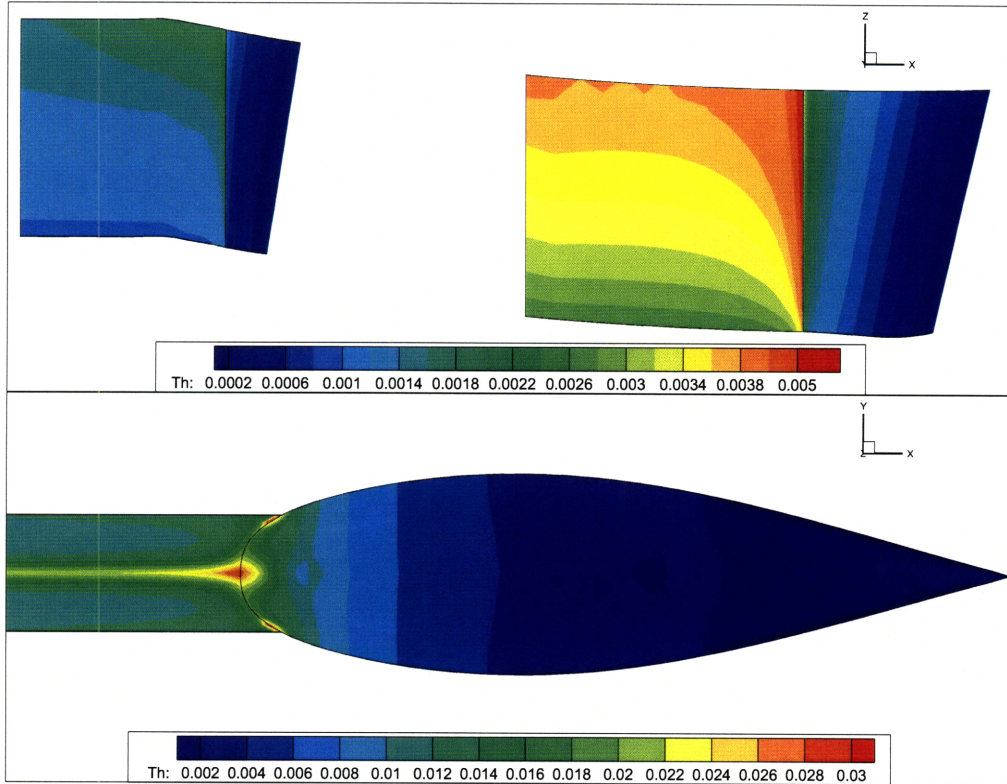
Figure 6-7: Momentum thickness solution θ for Condition A at $Fr = 0.35$.
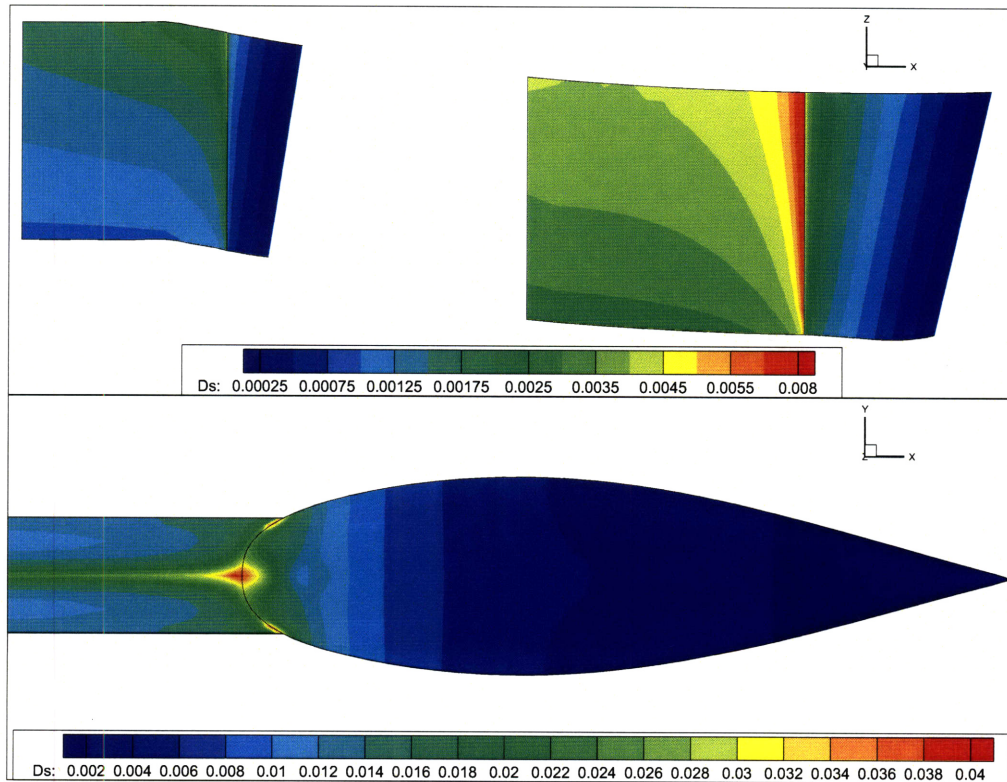
Figure 6-8: Displacement thickness solution δ^* for Condition A at $Fr = 0.35$.
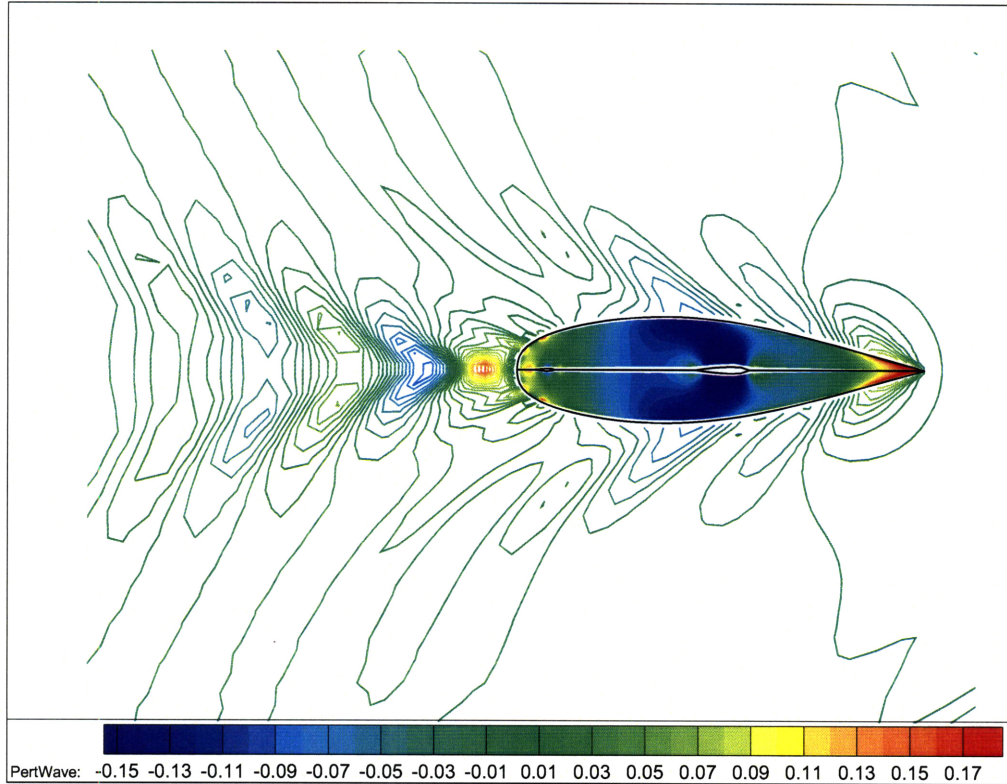
Figure 6-9: Wave pattern and pressure field for Model 5 appended for Condition A at $Fr = 0.25$.

The effects on the flow of the yaw angle and of the rudder angle are shown in the asymmetry of the wave pattern, both at the stern and along side the boat. Fig. 6-11 illustrates that the lower pressure on the suction side of the keel makes the wave trough on the starboard side of the boat deeper and a little more forward than in the port side. Looking at the pressure field drawn inside the hull boundary it is possible to notice also the difference in pressure on the two sides of the rudder. These effects are magnified when the speed is increased to 3.59 m/s, equivalent to a Froude number of 0.325 (see Fig. 6-13).

The total hydrodynamic forces computed by the program compared very well with the experiments. At $Fr = 0.25$ with the yaw and rudder angle equal to 2°, the total resistance in the tank was measured to be 597.3 N, with 155.1 N attributed to be pressure resistance and the remainder 442.2 N being frictional resistance. The computation predicted a total drag of 619.8 N, which is only 3.6% higher than the experiments, and this is divided into 155.1 N of residuary resistance and 464.7 N of
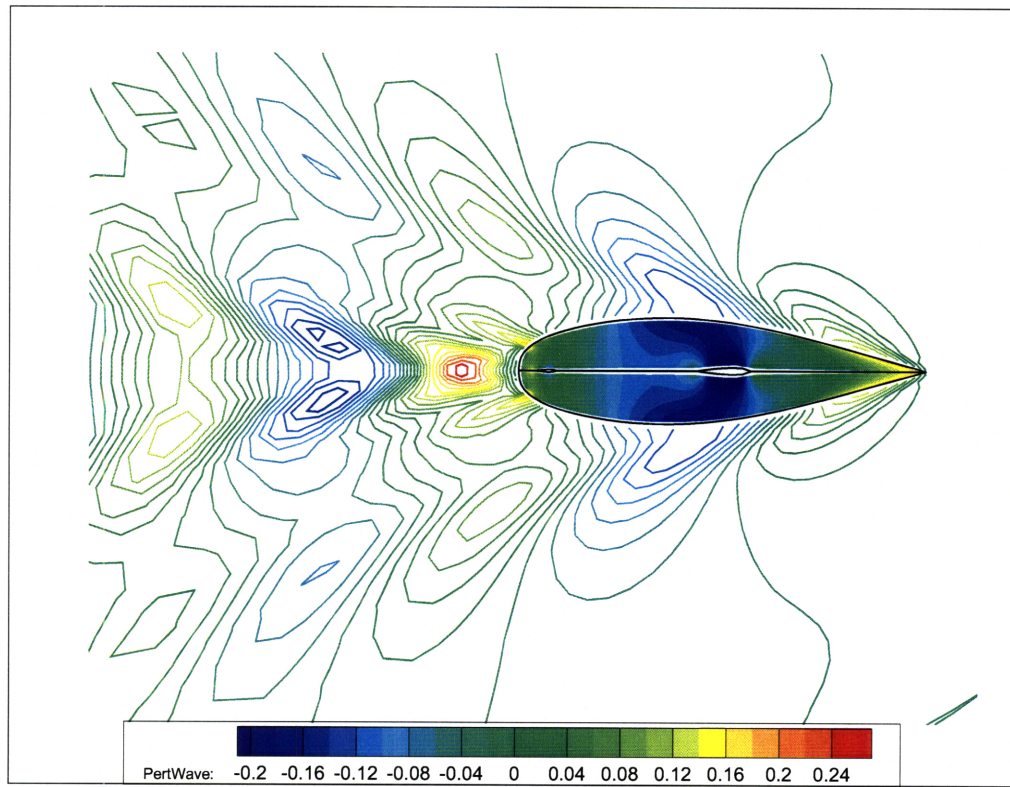
Figure 6-10: Wave pattern and pressure field for Model 5 appended for Condition A at $Fr = 0.35$.

		Residuary Drag [N]	Frictional Drag [N]	Total Drag [N]	Error	Lift [N]	Error
	Y/R = 0°	83.8	482.3	566.1	7.3%		
Computation	Y/R = 1°	111.3	459.3	570.6	5.1%	1647.9	-3.3%
	Y/R = 2°	155.1	464.7	619.8	3.6%	3304.0	1.6%
	Y/R = 0°	81.4	442.5	523.9			
Experiments	Y/R = 1°	99.2	442.3	541.4		1702.5	
	Y/R = 2°	155.1	442.2	597.3		3252.4	

Table 6.5: Numerical and experimental drag for Model 5 appended for the yaw and rudder angle series.

Figure 6-11: Wave pattern and pressure field for Model 5 appended at $Fr = 0.25$, with no heel and 2° of yaw and rudder angles.
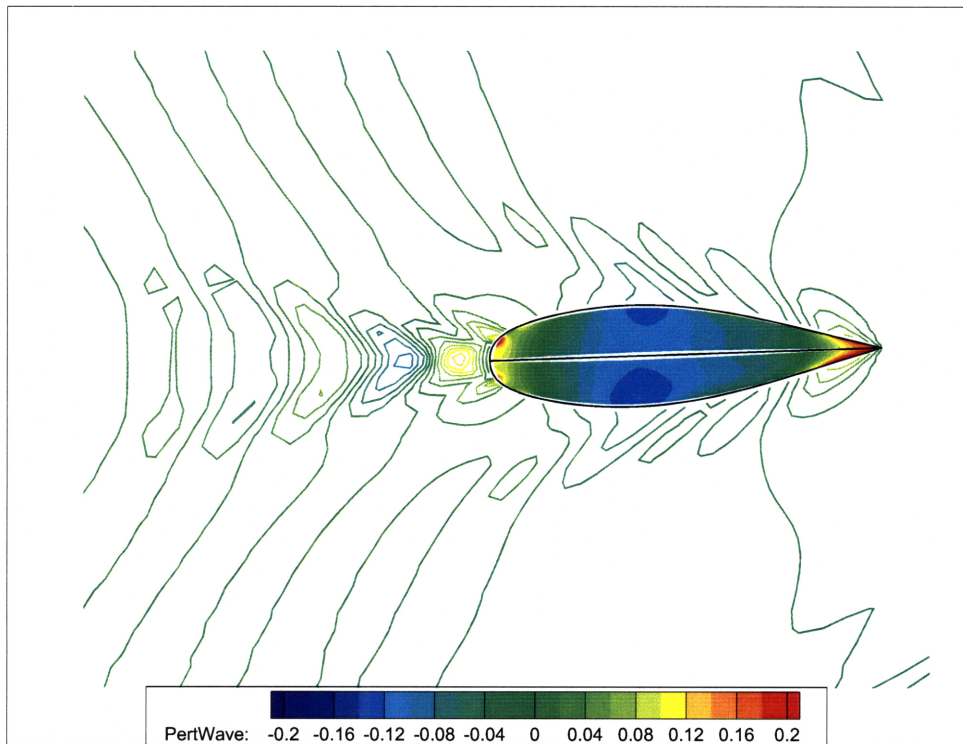
Figure 6-12: Wave pattern and pressure field for Model 5 canoe body at $Fr = 0.25$, with no heel and 2° of yaw angle.
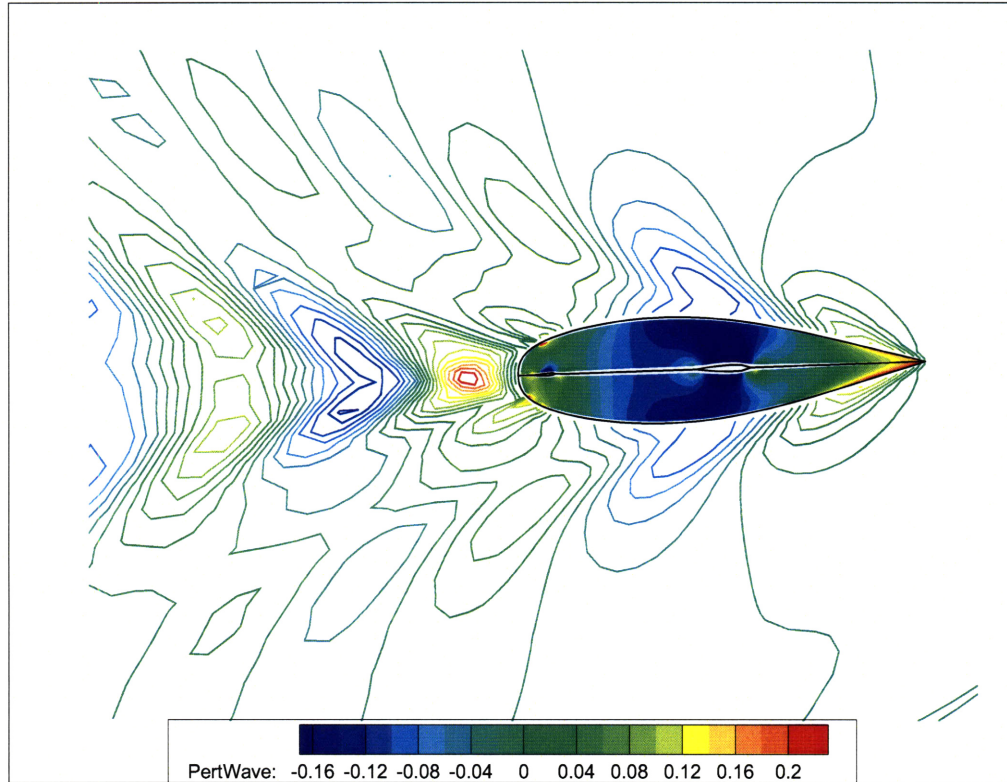
Figure 6-13: Wave pattern and pressure field for Model 5 appended at $Fr = 0.325$, with no heel and 2° of yaw and rudder angles.

frictional resistance. The comparison of the lift is much closer, with the tank predicting a lift of 3252.4 N, and the current method calculating a total lift of 3304.0 N, only 1.6% higher. Because when the same model is tested without appendages at 2° of yaw the computed lift was only 2.2 N, there is a misconception that all the lift in the appended model is generated by the keel and rudder. This is actually not the case: 416.2 N of lift, or 12.6% of the total, is generated by the asymmetric pressure distribution on the hull (Fig. 6-12). The keel and rudder generate respectively 1855.0 N and 1033.8 N, or 56.1% and 31.3%.

Table 6.5 shows the complete results for the yaw and rudder angle series.

At the higher Froude number the current method predicts a pressure resistance of 399.5 N, and a frictional resistance of 761.7 N. The numerical total drag is then 1161.2 N. This value is about 1.8% higher than the experimental value of 1139.9 N. In the experiments the total drag was measured to be composed of 413.7 N of pressure resistance and 726.2 N of frictional resistance.
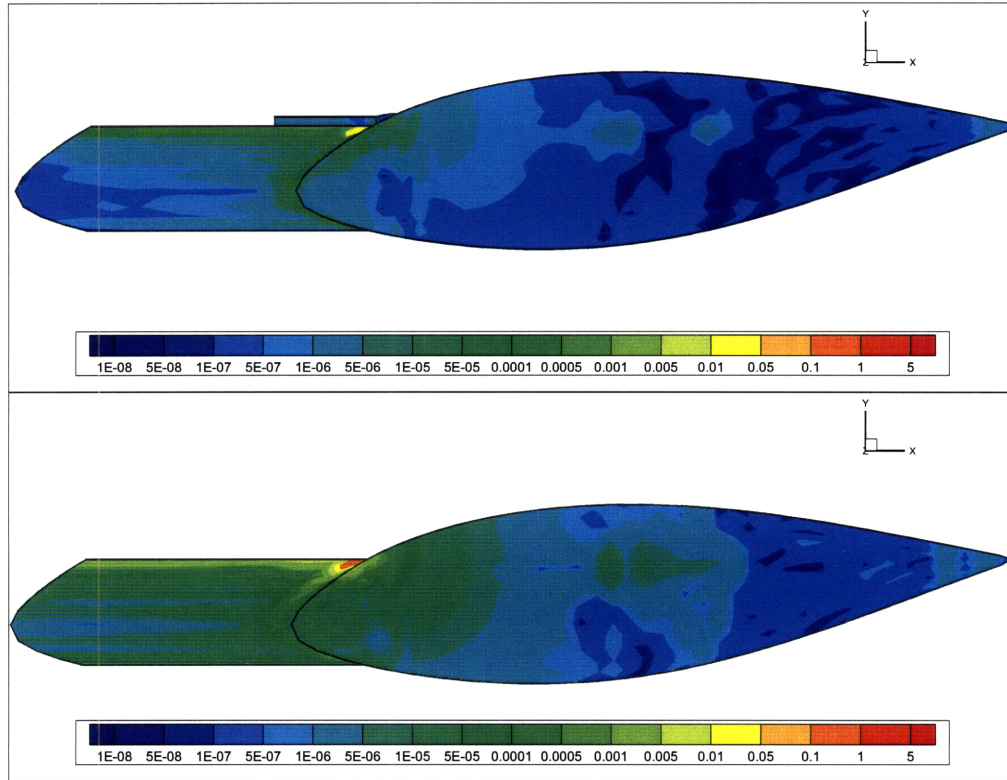
Figure 6-14: Residual values for the momentum and kinetic energy equations after 30 iterations.

The difference in lift between the numerical value of 5562.2 N and the experimental value of 5741.6 N is -3.2%.

6.4.3 Series C: Heel Variation

The last series simulates the most general condition at which a sailing yacht usually sails: heeled over to leeward while making leeway and with a non-zero rudder angle to balance the boat. Unfortunately experimental values are available only for an angle of heel equal to 15°.

At the higher heel angle, however, the boundary layer computation however did not come to full convergence. The iterative process started to converge, but then kept oscillating around the same solution without coming to complete convergence. The trouble area was identified by looking at the residuals of the boundary layer equations after each iteration, and it was found to be a small area on the hull wake right at the
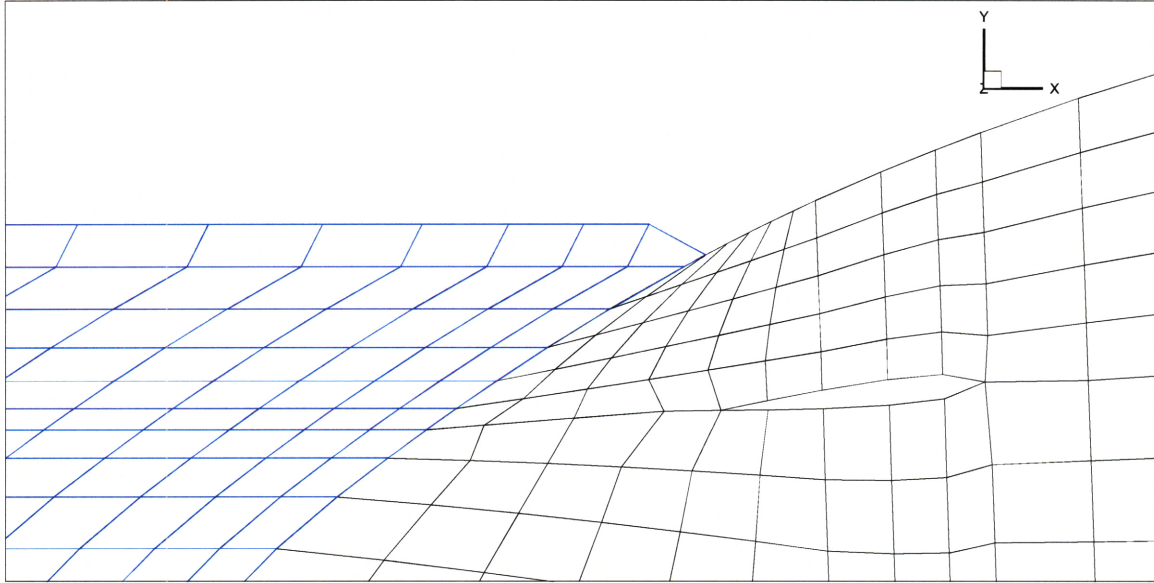
Figure 6-15: Detail of the computational grid on the stern windward corner.

stern on the windward side of the hull. Fig. 6-14 shows the residuals of the momentum equation (top half) and of the kinetic energy equation (bottom half) on the hull and its wake after 30 iterations. The area affected is the small patch in orange-yellow color. The residuals on the appendages were checked, and the values on the keel were generally smaller than 10^{-5}, while those on the top part of the rudder were higher, but still only of the order of 10^{-3}. The reason for the non-convergence was found to be in the geometry of the computational grid. When the hull is heeled over 15°, a portion of the windward half of the hull comes out of the water and gets very narrow near the stern and the grid lines on it become curved. The main assumption in implementing the current formulation for the boundary layer, was that the computational lines would approximate the streamlines, so that the cross-flow would be negligible. It is also necessary that the computational lines are smooth lines, without any hard kinks in them. Unfortunately that is not the case at the corner of the stern, where the grid lines get very close to each other and start going towards the centerline of the hull until they reach the stern and suddenly turn into the direction of the freestream (Fig. 6-15). This causes the influence matrix for the stern area to deteriorate, and in turn the boundary layer iterative process not to converge. Reducing the heel angle to 10° straightens the lines, increases the separation between them, and unskews the
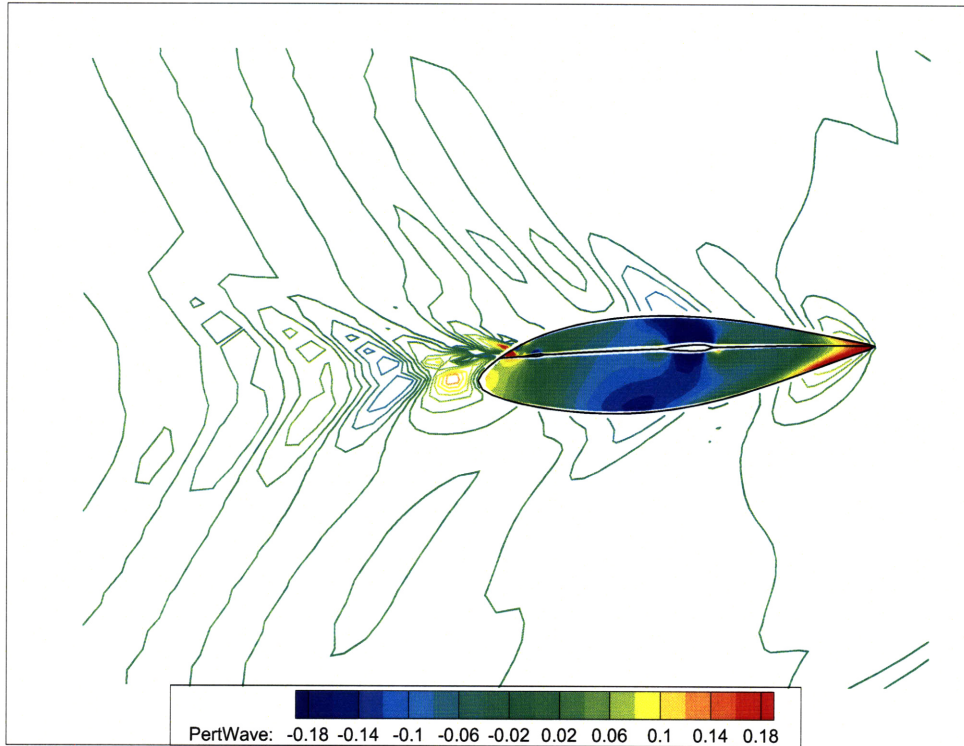
Figure 6-16: Wave pattern and pressure field for Model 5 appended at $Fr = 0.25$, with a heel angle of 15° and a yaw and rudder angles of 2°.
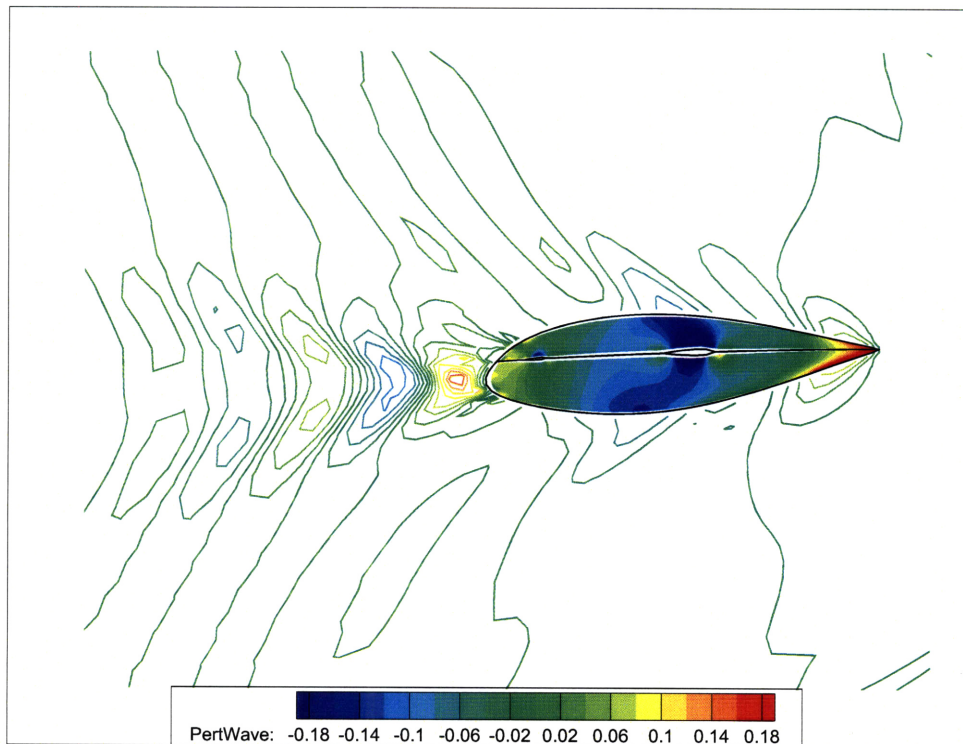
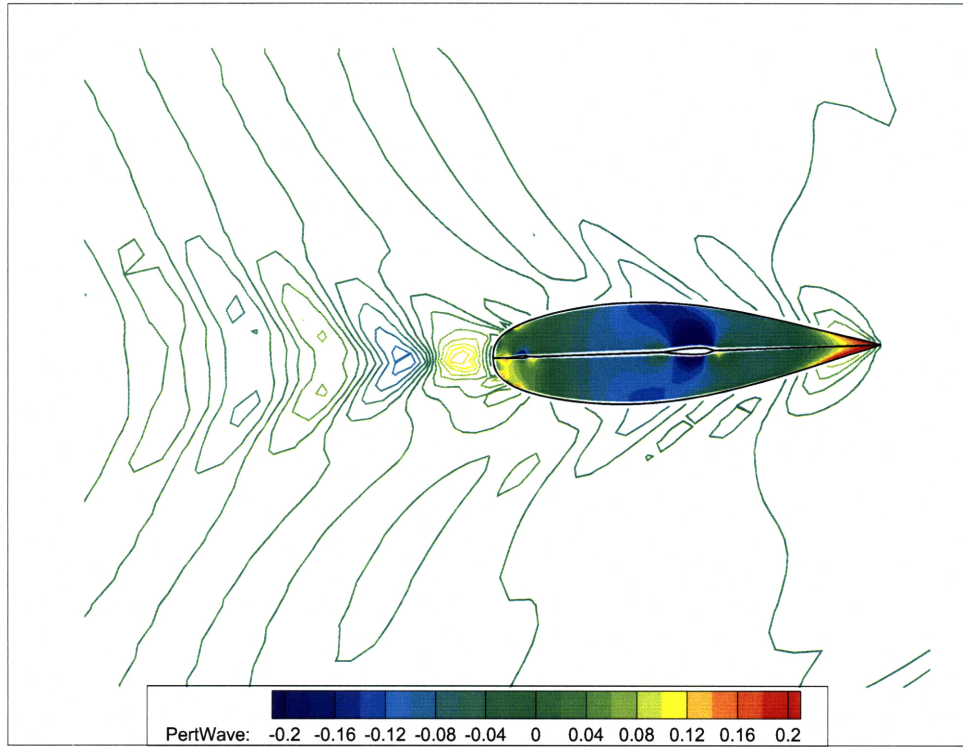
Figure 6-17: Wave pattern and pressure field for Model 5 appended at $Fr = 0.25$, with a heel angle of 10° and a yaw and rudder angles of 2°.

grid enough that the boundary layer solution has no problem converging completely and a complete solution can be computed.

Because the area affected is relatively small, it was decided to stop the boundary layer computation once it stopped making any progress, and use the solution as it was computed, accepting the fact that it had an error component in it. After checking that the boundary layer solution was reasonable, the linearized problem for the ship waves was then solved as usual.

Fig. 6-16 shows the resulting wave pattern and pressure field. The heel angle brought the low pressure on the suction side of the keel closer to the surface which results in a deep wave trough on the windward side of the hull. The computed forces agree reasonably well with the experimental findings. The experimental value of the pressure resistance is 137.0 N, and the total drag has a value of 570.6, which leaves the difference of 432.4 N as frictional resistance. The current method computed a value for the pressure resistance of 130.0 N, and a value of 452.6 N for the frictional resistance, for a total of 582.6 N. This value is 2.0% higher than the experimental one.

The computed sideforce value of 2859.3 N is 3.6% higher than the value of 2756.5 N obtained in the experiments. The sideforce is measured parallel to the y-axis, and it is equal to the lift divided by the cosine of the heel angle.

The wave pattern at 10° degrees of heel is shown in Fig. 6-17. The numerical results are 176.6 N of pressure drag, 457.3 N of frictional drag, for a total of 633.9 N. The computed sideforce is 3063.3 N.

Chapter 7

Conclusions and Recommendations

7.1 Conclusions

7.1.1 Summary of Numerical Implementation

A novel coupled inviscid/viscous algorithm for the prediction of the hydrodynamic forces on sailing yachts is presented in this thesis. The procedure couples a low order, constant strength panel method with a quasi 3-dimensional boundary layer solver by means of a distribution of blowing sources placed on the body and its wake surfaces. The potential flow boundary integral equation is first discretized to solve for the double-body flow. Then edge velocity equations are derived so that the displacement perturbations to the inviscid velocity depend only on viscous quantities and on the influence matrices. The boundary layer equations are then discretized, and the system of equations is closed using the edge velocity equations. The system is solved using Newton's method to find the viscous variables and also a set of blowing sources that provides an inviscid flow that produces effects equivalent to the viscous boundary layer for the double body problem. Once the coupled double body-boundary layer solution is found, the blowing sources are introduced in the solution of the free-surface linearized potential flow problem for determining the ship waves. The velocity field computed from the linearized solution is then used to compute the pressure forces and the frictional coefficient from the boundary layer solution is used to find the frictional

forces.

To ensure the accurate representation of the geometry, the hull and appendages are defined as NURBS surfaces, and are imported using an IGES file, format compatible with the majority of hull definition CAD packages. The geometry is then reconstructed and divided into panels.

7.1.2 Summary of Results

Calculation of both lift and drag were made for a canoe body and an appended hull under different conditions. Results were compared with experimental data obtained from a towing tank facility. The results generally compared reasonably well with the experiments within the limit of the linear method and of the boundary layer method. Differences for the total resistance were generally of the order of 5%, and the values of lift were within 3%.

The linearized free surface solver was compared with another linear, free-surface solver, SWAN, for the simulation of a Wigley hull and with experimental data from the literature: both the computed wave pattern and the wave resistance coefficient showed good agreement, with results that fell within the range of collected data. The wave profile along the hull was checked against experimental and numerical obtained by Raven [24] as part of his work.

The coupled inviscid/viscous solver was validated by running a long-span, straight wing of known section and comparing the results with those obtained using PAN2D-BL, a two-dimensional boundary layer solver.

7.2 Recommendations

The method developed here was successful in the prediction of lift and drag forces for a sailing yacht in a variety of conditions, however some limitations were found that suggest possible improvements.

High heel angle limit

It was found that with the current routine for the geometry discretization the assumption of having computational lines closely approximating the streamlines breaks down when the heel angle is at or above 15°. This causes the boundary layer solution not to converge. Although, even using a partially converged viscous solution the linearized flow problem yield a reasonable solution, it is advisable to improve the panelization routine.

Aft End of the Waterline Condition

As stated before, the smooth detachment of the flow at the stern ending of the waterline is ensured by the imposition of conditions that set the wave height and the wave slope equal to that of the stern overhang of the boat. The points on the free-surface on which this condition was imposed, was here determined empirically, and it has some effects on the wave resistance. However, the only alternative to having to impose a condition at the stern is to solve the fully non-linear free surface problem. The solution of the non-linear problem would allow capturing the increase in sailing length due to the rise of the water along the stern overhang, which would lead to a more accurate evaluation of the wave resistance, by virtue of computing the exact detachment point of the flow, and of the frictional resistance because of a more accurate representation of the actual wetted surface.

Boundary layer solution

As of now the boundary layer is coupled to the double-body flow and the combination of the two provides the base flow for the linearized wave-making solution. The frictional coefficient is computed from the coupled flow and, although integrated using the linear solution velocity, it is not affected by it. A possible improvement would to computed a second boundary layer solution, this time coupled with the linearized flow problem.

Appendix A

IGES File Format

The Initial Graphics Exchange Specification (IGES) defines a neutral data format that allows the digital exchange of information among Computer-aided design (CAD) systems. It was first published in 1980 by the National Bureau of Standards, now National Institute for Standards and Technology, as a technical report that was the result of a project started by a group of CAD users and vendors with the support of NBS.

The IGES file is composed of 80-character ASCII records, divided into 5 sections, marked S, G, D, P, and T in column 72. The first section of the file is the header (lines marked with a G on the right) and contains information about the software that created the file, the date and time of creation, etc.; the next two sections contain the characteristic and geometric information of all the entities, the first one (marked with a D) is two record length directory entry with the basic charateristics of the entity, what they are (128 refers to a NURBS surface, 106 to a NURBS curve, etc.), their order, etc.; the second (marked with a P), in a multiple record length, comma delimited format, contains all the necessary information to evaluate the corrsponding entity, which in the case of a NURBS surface, are the knot vectors, the weights, and the control network point coordinates. More details about the IGES file format can be found in [23].

```
Data transfer to IGES file format                                    S     1
1H,,1H;,7HMaxsurf,11HUssaM4S.igs,3HWin,                              G     1
```

```
11HVersion 6.0,32,38,6,38,15,,1.00000,6,1HM,1,,                          G      2
13H041105.142913,0.0001,14.61259,                                        G      3
9HFormation,32HFormation Design Systems Pty Ltd,6,0                      G      4
       128       1             1       0       0       0      000000000D  1
       128       0       0     113       0            BS SURF        1D   2
       128     114             1       0       0       0      000000000D  3
       128       0       0     113       0            BS SURF        2D   4
128,7,12,4,5,0,0,0,0,0,0.000000e+000,0.000000e+000,                      1P     1
0.000000e+000,0.000000e+000,0.000000e+000,2.500000e-001,                 1P     2
5.000000e-001,7.500000e-001,1.000000e+000,1.000000e+000,                 1P     3
1.000000e+000,1.000000e+000,1.000000e+000,0.000000e+000,                 1P     4
0.000000e+000,0.000000e+000,0.000000e+000,0.000000e+000,                 1P     5
0.000000e+000,1.250000e-001,2.500000e-001,3.750000e-001,                 1P     6
5.000000e-001,6.250000e-001,7.500000e-001,8.750000e-001,                 1P     7
1.000000e+000,1.000000e+000,1.000000e+000,1.000000e+000,                 1P     8
1.000000e+000,1.000000e+000,1.000000e+000,1.000000e+000,                 1P     9
1.000000e+000,1.000000e+000,1.000000e+000,1.000000e+000,                 1P    10
1.000000e+000,1.000000e+000,1.000000e+000,1.000000e+000,                 1P    11
1.000000e+000,1.000000e+000,1.000000e+000,1.000000e+000,                 1P    12
1.000000e+000,1.000000e+000,1.000000e+000,1.000000e+000,                 1P    13
1.000000e+000,1.000000e+000,1.000000e+000,1.000000e+000,                 1P    14
1.000000e+000,1.000000e+000,1.000000e+000,1.000000e+000,                 1P    15
1.000000e+000,1.000000e+000,1.000000e+000,1.000000e+000,                 1P    16
1.000000e+000,1.000000e+000,1.000000e+000,1.000000e+000,                 1P    17
1.000000e+000,1.000000e+000,1.000000e+000,1.000000e+000,                 1P    18
1.000000e+000,1.000000e+000,1.000000e+000,1.000000e+000,                 1P    19
1.000000e+000,1.000000e+000,1.000000e+000,1.000000e+000,                 1P    20
1.000000e+000,1.000000e+000,1.000000e+000,1.000000e+000,                 1P    21
1.000000e+000,1.000000e+000,1.000000e+000,1.000000e+000,                 1P    22
1.000000e+000,1.000000e+000,1.000000e+000,1.000000e+000,                 1P    23
1.000000e+000,1.000000e+000,1.000000e+000,1.000000e+000,                 1P    24
1.000000e+000,1.000000e+000,1.000000e+000,1.000000e+000,                 1P    25
1.000000e+000,1.000000e+000,1.000000e+000,1.000000e+000,                 1P    26
1.000000e+000,1.000000e+000,1.000000e+000,1.000000e+000,                 1P    27
1.000000e+000,1.000000e+000,1.000000e+000,1.000000e+000,                 1P    28
1.000000e+000,1.000000e+000,1.000000e+000,1.000000e+000,                 1P    29
1.000000e+000,1.000000e+000,1.000000e+000,1.000000e+000,                 1P    30
1.000000e+000,1.000000e+000,1.000000e+000,1.000000e+000,                 1P    31
1.000000e+000,1.000000e+000,1.000000e+000,1.000000e+000,                 1P    32
1.000000e+000,1.000000e+000,1.000000e+000,1.000000e+000,                 1P    33
1.000000e+000,1.000000e+000,1.000000e+000,1.000000e+000,                 1P    34
1.000000e+000,1.000000e+000,6.045691e+000,0.000000e+000,                 1P    35
-4.700000e-002,6.170691e+000,0.000000e+000,-1.773000e-002,               1P    36
6.295691e+000,0.000000e+000,1.153000e-002,6.342841e+000,                 1P    37
0.000000e+000,1.330000e-001,6.455401e+000,0.000000e+000,                 1P    38
4.229300e-001,6.595171e+000,0.000000e+000,7.830000e-001,                 1P    39
6.740551e+000,0.000000e+000,1.157480e+000,6.854371e+000,                 1P    40
```

```
0.000000e+000,1.450670e+000,5.955691e+000,0.000000e+000,          1P    41
-7.128000e-002,6.031401e+000,-1.753000e-002,-5.085000e-002,       1P    42
6.130661e+000,-3.032000e-002,-2.267000e-002,6.185121e+000,        1P    43
-3.848000e-002,1.115000e-001,6.270081e+000,-4.926000e-002,        1P    44
4.020700e-001,6.375761e+000,-6.223000e-002,7.637100e-001,         1P    45
6.486041e+000,-7.503000e-002,1.141099e+000,6.573071e+000,         1P    46
-8.459000e-002,1.438900e+000,5.805691e+000,0.000000e+000,         1P    47
-1.103800e-001,5.847101e+000,-3.240000e-002,-1.011800e-001,       1P    48
5.889151e+000,-7.187000e-002,-6.825000e-002,5.942201e+000,        1P    49
-9.466000e-002,7.700000e-002,5.998721e+000,-1.213900e-001,        1P    50
3.721300e-001,6.068751e+000,-1.485700e-001,7.370100e-001,         1P    51
6.142151e+000,-1.753000e-001,1.119380e+000,6.200541e+000,         1P    52
-1.963400e-001,1.423600e+000,5.541961e+000,0.000000e+000,         1P    53
-1.760600e-001,5.541961e+000,-5.424000e-002,-1.691400e-001,       1P    54
5.543931e+000,-1.227100e-001,-1.272000e-001,5.556851e+000,        1P    55
-1.796900e-001,2.439000e-002,5.585511e+000,-2.305200e-001,        1P    56
3.270000e-001,5.620091e+000,-2.734700e-001,6.995000e-001,         1P    57
5.657451e+000,-3.164100e-001,1.089500e+000,5.686461e+000,         1P    58
-3.499000e-001,1.403000e+000,4.965691e+000,0.000000e+000,         1P    59
-3.039600e-001,4.965691e+000,-9.116000e-002,-2.871900e-001,       1P    60
4.965691e+000,-1.972100e-001,-2.238300e-001,4.965691e+000,        1P    61
-3.024000e-001,-4.723000e-002,4.965691e+000,-3.900400e-001,       1P    62
2.636700e-001,4.965691e+000,-4.540200e-001,6.460000e-001,         1P    63
4.965691e+000,-5.136300e-001,1.048999e+000,4.965691e+000,         1P    64
-5.618300e-001,1.375199e+000,3.845762e+000,0.000000e+000,         1P    65
-4.583700e-001,3.845762e+000,-1.554500e-001,-4.412500e-001,       1P    66
3.845762e+000,-3.339000e-001,-3.722400e-001,3.845762e+000,        1P    67
-5.194300e-001,-1.806500e-001,3.845762e+000,-6.635100e-001,       1P    68
1.630000e-001,3.845762e+000,-7.513800e-001,5.660000e-001,         1P    69
3.845762e+000,-8.257000e-001,9.859990e-001,3.845762e+000,         1P    70
-8.782500e-001,1.334999e+000,2.325691e+000,0.000000e+000,         1P    71
-5.770700e-001,2.325691e+000,-2.341900e-001,-5.704600e-001,       1P    72
2.325691e+000,-5.190300e-001,-4.987900e-001,2.325691e+000,        1P    73
-7.972500e-001,-3.005100e-001,2.325691e+000,-9.997600e-001,       1P    74
6.000000e-002,2.325691e+000,-1.118860e+000,4.760000e-001,         1P    75
2.325691e+000,-1.201740e+000,9.150000e-001,2.325691e+000,         1P    76
-1.263769e+000,1.286500e+000,6.456909e-001,0.000000e+000,         1P    77
-6.462000e-001,6.456909e-001,-3.142100e-001,-6.462000e-001,       1P    78
6.456909e-001,-6.750600e-001,-5.779500e-001,6.456909e-001,        1P    79
-1.037649e+000,-3.834700e-001,6.456909e-001,-1.326140e+000,       1P    80
-7.000001e-003,6.456909e-001,-1.441570e+000,4.140000e-001,        1P    81
6.456909e-001,-1.523040e+000,8.610000e-001,6.456909e-001,         1P    82
-1.583840e+000,1.243140e+000,-1.154308e+000,0.000000e+000,        1P    83
-6.528600e-001,-1.154308e+000,-3.619600e-001,-6.528600e-001,      1P    84
-1.154308e+000,-7.695700e-001,-5.861300e-001,-1.154308e+000,      1P    85
-1.177919e+000,-3.984500e-001,-1.154308e+000,-1.506119e+000,      1P    86
-2.526000e-002,-1.154308e+000,-1.635840e+000,3.890000e-001,       1P    87
```

101

```
-1.154308e+000,-1.712669e+000,8.300000e-001,-1.154308e+000,                1P     88
-1.760349e+000,1.207250e+000,-2.909988e+000,0.000000e+000,                 1P     89
-5.561800e-001,-2.909988e+000,-3.637500e-001,-5.561800e-001,               1P     90
-2.909988e+000,-7.713200e-001,-4.906100e-001,-2.909988e+000,               1P     91
-1.177919e+000,-3.266100e-001,-2.909988e+000,-1.500579e+000,               1P     92
2.200000e-002,-2.909988e+000,-1.627200e+000,4.130000e-001,                 1P     93
-2.909988e+000,-1.703029e+000,8.279400e-001,-2.909968e+000,                1P     94
-1.751240e+000,1.183859e+000,-4.653289e+000,0.000000e+000,                 1P     95
-3.257300e-001,-4.653289e+000,-3.181700e-001,-3.257300e-001,               1P     96
-4.653289e+000,-6.777500e-001,-2.804400e-001,-4.653289e+000,               1P     97
-1.042379e+000,-1.449700e-001,-4.653289e+000,-1.312019e+000,               1P     98
1.422500e-001,-4.653289e+000,-1.445559e+000,4.860000e-001,                 1P     99
-4.653289e+000,-1.533789e+000,8.540000e-001,-4.653269e+000,                1P    100
-1.588009e+000,1.170880e+000,-6.268039e+000,0.000000e+000,                 1P    101
2.100000e-002,-6.268039e+000,-2.542600e-001,2.100000e-002,                 1P    102
-6.268039e+000,-5.437000e-001,3.841000e-002,-6.268039e+000,                1P    103
-8.252100e-001,1.285900e-001,-6.268039e+000,-1.061149e+000,                1P    104
3.147200e-001,-6.268039e+000,-1.195199e+000,5.829800e-001,                 1P    105
-6.268039e+000,-1.291960e+000,8.900500e-001,-6.268039e+000,                1P    106
-1.355690e+000,1.164740e+000,-7.758219e+000,0.000000e+000,                 1P    107
2.830000e-001,-7.758219e+000,-1.826500e-001,2.830000e-001,                 1P    108
-7.758219e+000,-4.123300e-001,2.986300e-001,-7.758219e+000,                1P    109
-6.107300e-001,3.576400e-001,-7.758219e+000,-7.984000e-001,                1P    110
4.917700e-001,-7.758219e+000,-9.405000e-001,6.929700e-001,                 1P    111
-7.758219e+000,-1.041280e+000,9.346400e-001,-7.758219e+000,                1P    112
-1.113330e+000,1.163049e+000,0.0,1.0,0.0,1.0                               1P    113
128,7,12,4,5,0,0,0,0,0,0.000000e+000,0.000000e+000,                        3P    114
0.000000e+000,0.000000e+000,0.000000e+000,2.500000e-001,                   3P    115
5.000000e-001,7.500000e-001,1.000000e+000,1.000000e+000,                   3P    116
1.000000e+000,1.000000e+000,1.000000e+000,0.000000e+000,                   3P    117
0.000000e+000,0.000000e+000,0.000000e+000,0.000000e+000,                   3P    118
0.000000e+000,1.250000e-001,2.500000e-001,3.750000e-001,                   3P    119
5.000000e-001,6.250000e-001,7.500000e-001,8.750000e-001,                   3P    120
1.000000e+000,1.000000e+000,1.000000e+000,1.000000e+000,                   3P    121
1.000000e+000,1.000000e+000,1.000000e+000,1.000000e+000,                   3P    122
1.000000e+000,1.000000e+000,1.000000e+000,1.000000e+000,                   3P    123
1.000000e+000,1.000000e+000,1.000000e+000,1.000000e+000,                   3P    124
1.000000e+000,1.000000e+000,1.000000e+000,1.000000e+000,                   3P    125
1.000000e+000,1.000000e+000,1.000000e+000,1.000000e+000,                   3P    126
1.000000e+000,1.000000e+000,1.000000e+000,1.000000e+000,                   3P    127
1.000000e+000,1.000000e+000,1.000000e+000,1.000000e+000,                   3P    128
1.000000e+000,1.000000e+000,1.000000e+000,1.000000e+000,                   3P    129
1.000000e+000,1.000000e+000,1.000000e+000,1.000000e+000,                   3P    130
1.000000e+000,1.000000e+000,1.000000e+000,1.000000e+000,                   3P    131
1.000000e+000,1.000000e+000,1.000000e+000,1.000000e+000,                   3P    132
1.000000e+000,1.000000e+000,1.000000e+000,1.000000e+000,                   3P    133
1.000000e+000,1.000000e+000,1.000000e+000,1.000000e+000,                   3P    134
```

```
1.000000e+000,1.000000e+000,1.000000e+000,1.000000e+000,          3P    135
1.000000e+000,1.000000e+000,1.000000e+000,1.000000e+000,          3P    136
1.000000e+000,1.000000e+000,1.000000e+000,1.000000e+000,          3P    137
1.000000e+000,1.000000e+000,1.000000e+000,1.000000e+000,          3P    138
1.000000e+000,1.000000e+000,1.000000e+000,1.000000e+000,          3P    139
1.000000e+000,1.000000e+000,1.000000e+000,1.000000e+000,          3P    140
1.000000e+000,1.000000e+000,1.000000e+000,1.000000e+000,          3P    141
1.000000e+000,1.000000e+000,1.000000e+000,1.000000e+000,          3P    142
1.000000e+000,1.000000e+000,1.000000e+000,1.000000e+000,          3P    143
1.000000e+000,1.000000e+000,1.000000e+000,1.000000e+000,          3P    144
1.000000e+000,1.000000e+000,1.000000e+000,1.000000e+000,          3P    145
1.000000e+000,1.000000e+000,1.000000e+000,1.000000e+000,          3P    146
1.000000e+000,1.000000e+000,1.000000e+000,1.000000e+000,          3P    147
1.000000e+000,1.000000e+000,6.045691e+000,0.000000e+000,          3P    148
-4.700000e-002,6.170691e+000,0.000000e+000,-1.773000e-002,        3P    149
6.295691e+000,0.000000e+000,1.153000e-002,6.342841e+000,          3P    150
0.000000e+000,1.330000e-001,6.455401e+000,0.000000e+000,          3P    151
4.229300e-001,6.595171e+000,0.000000e+000,7.830000e-001,          3P    152
6.740551e+000,0.000000e+000,1.157480e+000,6.854371e+000,          3P    153
0.000000e+000,1.450670e+000,5.955691e+000,0.000000e+000,          3P    154
-7.128000e-002,6.031401e+000,1.753000e-002,-5.085000e-002,        3P    155
6.130661e+000,3.032000e-002,-2.267000e-002,6.185121e+000,         3P    156
3.848000e-002,1.115000e-001,6.270081e+000,4.926000e-002,          3P    157
4.020700e-001,6.375761e+000,6.223000e-002,7.637100e-001,          3P    158
6.486041e+000,7.503000e-002,1.141099e+000,6.573071e+000,          3P    159
8.459000e-002,1.438900e+000,5.805691e+000,0.000000e+000,          3P    160
-1.103800e-001,5.847101e+000,3.240000e-002,-1.011800e-001,        3P    161
5.889151e+000,7.187000e-002,-6.825000e-002,5.942201e+000,         3P    162
9.466000e-002,7.700000e-002,5.998721e+000,1.213900e-001,          3P    163
3.721300e-001,6.068751e+000,1.485700e-001,7.370100e-001,          3P    164
6.142151e+000,1.753000e-001,1.119380e+000,6.200541e+000,          3P    165
1.963400e-001,1.423600e+000,5.541961e+000,0.000000e+000,          3P    166
-1.760600e-001,5.541961e+000,5.424000e-002,-1.691400e-001,        3P    167
5.543931e+000,1.227100e-001,-1.272000e-001,5.556851e+000,         3P    168
1.796900e-001,2.439000e-002,5.585511e+000,2.305200e-001,          3P    169
3.270000e-001,5.620091e+000,2.734700e-001,6.995000e-001,          3P    170
5.657451e+000,3.164100e-001,1.089500e+000,5.686461e+000,          3P    171
3.499000e-001,1.403000e+000,4.965691e+000,0.000000e+000,          3P    172
-3.039600e-001,4.965691e+000,9.116000e-002,-2.871900e-001,        3P    173
4.965691e+000,1.972100e-001,-2.238300e-001,4.965691e+000,         3P    174
3.024000e-001,-4.723000e-002,4.965691e+000,3.900400e-001,         3P    175
2.636700e-001,4.965691e+000,4.540200e-001,6.460000e-001,          3P    176
4.965691e+000,5.136300e-001,1.048999e+000,4.965691e+000,          3P    177
5.618300e-001,1.375199e+000,3.845762e+000,0.000000e+000,          3P    178
-4.583700e-001,3.845762e+000,1.554500e-001,-4.412500e-001,        3P    179
3.845762e+000,3.339000e-001,-3.722400e-001,3.845762e+000,         3P    180
5.194300e-001,-1.806500e-001,3.845762e+000,6.635100e-001,         3P    181
```

103

```
1.630000e-001,3.845762e+000,7.513800e-001,5.660000e-001,          3P    182
3.845762e+000,8.257000e-001,9.859990e-001,3.845762e+000,          3P    183
8.782500e-001,1.334999e+000,2.325691e+000,0.000000e+000,          3P    184
-5.770700e-001,2.325691e+000,2.341900e-001,-5.704600e-001,        3P    185
2.325691e+000,5.190300e-001,-4.987900e-001,2.325691e+000,         3P    186
7.972500e-001,-3.005100e-001,2.325691e+000,9.997600e-001,         3P    187
6.000000e-002,2.325691e+000,1.118860e+000,4.760000e-001,          3P    188
2.325691e+000,1.201740e+000,9.150000e-001,2.325691e+000,          3P    189
1.263769e+000,1.286500e+000,6.456909e-001,0.000000e+000,          3P    190
-6.462000e-001,6.456909e-001,3.142100e-001,-6.462000e-001,        3P    191
6.456909e-001,6.750600e-001,-5.779500e-001,6.456909e-001,         3P    192
1.037649e+000,-3.834700e-001,6.456909e-001,1.326140e+000,         3P    193
-7.000001e-003,6.456909e-001,1.441570e+000,4.140000e-001,         3P    194
6.456909e-001,1.523040e+000,8.610000e-001,6.456909e-001,          3P    195
1.583840e+000,1.243140e+000,-1.154308e+000,0.000000e+000,         3P    196
-6.528600e-001,-1.154308e+000,3.619600e-001,-6.528600e-001,       3P    197
-1.154308e+000,7.695700e-001,-5.861300e-001,-1.154308e+000,       3P    198
1.177919e+000,-3.984500e-001,-1.154308e+000,1.506119e+000,        3P    199
-2.526000e-002,-1.154308e+000,1.635840e+000,3.890000e-001,        3P    200
-1.154308e+000,1.712669e+000,8.300000e-001,-1.154308e+000,        3P    201
1.760349e+000,1.207250e+000,-2.909988e+000,0.000000e+000,         3P    202
-5.561800e-001,-2.909988e+000,3.637500e-001,-5.561800e-001,       3P    203
-2.909988e+000,7.713200e-001,-4.906100e-001,-2.909988e+000,       3P    204
1.177919e+000,-3.266100e-001,-2.909988e+000,1.500579e+000,        3P    205
2.200000e-002,-2.909988e+000,1.627200e+000,4.130000e-001,         3P    206
-2.909988e+000,1.703029e+000,8.279400e-001,-2.909968e+000,        3P    207
1.751240e+000,1.183859e+000,-4.653289e+000,0.000000e+000,         3P    208
-3.257300e-001,-4.653289e+000,3.181700e-001,-3.257300e-001,       3P    209
-4.653289e+000,6.777500e-001,-2.804400e-001,-4.653289e+000,       3P    210
1.042379e+000,-1.449700e-001,-4.653289e+000,1.312019e+000,        3P    211
1.422500e-001,-4.653289e+000,1.445559e+000,4.860000e-001,         3P    212
-4.653289e+000,1.533789e+000,8.540000e-001,-4.653269e+000,        3P    213
1.588009e+000,1.170880e+000,-6.268039e+000,0.000000e+000,         3P    214
2.100000e-002,-6.268039e+000,2.542600e-001,2.100000e-002,         3P    215
-6.268039e+000,5.437000e-001,3.841000e-002,-6.268039e+000,        3P    216
8.252100e-001,1.285900e-001,-6.268039e+000,1.061149e+000,         3P    217
3.147200e-001,-6.268039e+000,1.195199e+000,5.829800e-001,         3P    218
-6.268039e+000,1.291960e+000,8.900500e-001,-6.268039e+000,        3P    219
1.355690e+000,1.164740e+000,-7.758219e+000,0.000000e+000,         3P    220
2.830000e-001,-7.758219e+000,1.826500e-001,2.830000e-001,         3P    221
-7.758219e+000,4.123300e-001,2.986300e-001,-7.758219e+000,        3P    222
6.107300e-001,3.576400e-001,-7.758219e+000,7.984000e-001,         3P    223
4.917700e-001,-7.758219e+000,9.405000e-001,6.929700e-001,         3P    224
-7.758219e+000,1.041280e+000,9.346400e-001,-7.758219e+000,        3P    225
1.113330e+000,1.163049e+000,0.0,1.0,0.0,1.0                       3P    226
S       1G      4D      4P      226                                T      1
```

Appendix B

Sample Input File

The following is an example of input file the the program uses.

The first line contains the name of the IGES file with the description of the geometry.
The following section has the number of surfaces that form the complete geometry
and the desired grid characteristics. The three logical operators set the use of the aft
end of the waterline condition and the presence of the wake for the keel and rudder.
Then the heel, yaw and rudder angle are read, with the displacement is sailing trim
and the waterline length next.

```
UssaM5App.igs                     ! Geometry input file name
6                       ! number of surfaces
Hull
47                      ! number of points in x-direction on 1st surface
12                       ! number of points in 2nd direction on 1st surface
1                       ! panel spacing in x-dir: 1=constant, 2=cosine, 3=geometric
1                       ! panel spacing in 2nd dir: 1=constant, 2=cosine, 3=geometric
Hull
47                      ! number of points in x-direction on 1st surface
5                       ! number of points in 2nd direction on 1st surface
1                       ! panel spacing in x-dir: 1=constant, 2=cosine, 3=geometric
1                       ! panel spacing in 2nd dir: 1=constant, 2=cosine, 3=geometric
Keel
21                       ! number of points in x-direction on 2nd surface
11                       ! number of points in 2nd direction on 2nd surface
2                       ! panel spacing in x-dir: 1=constant, 2=cosine, 3=geometric
3                       ! panel spacing in 2nd dir: 1=constant, 2=cosine, 3=geometric
Keel
21                       ! number of points in x-direction on 2nd surface
11                       ! number of points in 2nd direction on 2nd surfaceKeel
2                       ! panel spacing in x-dir: 1=constant, 2=cosine, 3=geometric
```

```
3                           ! panel spacing in 2nd dir: 1=constant, 2=cosine, 3=geometric
Rudder
25                          ! number of points in x-direction on 2nd surface
11                          ! number of points in 2nd direction on 2nd surface
2                           ! panel spacing in x-dir: 1=constant, 2=cosine, 3=geometric
3                           ! panel spacing in 2nd dir: 1=constant, 2=cosine, 3=geometric
Rudder
25                          ! number of points in x-direction on 2nd surface
11                          ! number of points in 2nd direction on 2nd surface
2                           ! panel spacing in x-dir: 1=constant, 2=cosine, 3=geometric
3                           ! panel spacing in 2nd dir: 1=constant, 2=cosine, 3=geometric
5                           ! number of points to use at intersections
31                          ! number of points on the free surface in the radial direction
.true.                      ! Transom condition
.true.                      ! wake from keel
.true.                      ! wake from rudder
15.0                        ! Heel Angle in degrees
0.0                         ! Leeway Angle in degrees
2.0                         ! Rudder Angle in degrees
9163.0                      ! Displacement in Sailing trim
12.3                        ! Design Waterline Length
```

Appendix C

Boundary Layer Empirical Closure Formulae

This appendix presents the empirical closure formulae used in the subroutines provided by Drela [7], used for the calculations of the viscous flow. These are here speciallized for an incompressible fluid. A more complete description of these relations can be found in [21] and [15].

Thicknesses

Displacement thickness

$$\delta^* = \int \left(1 - \frac{u}{q_e}\right) d\eta \tag{C.1}$$

Momentum thickness

$$\theta = \int \left(1 - \frac{u}{q_e}\right) \frac{u}{q_e} d\eta \tag{C.2}$$

Kinetic energy thickness

$$E = \int \left[1 - \left(\frac{u}{q_e}\right)^2\right] \frac{u}{q_e} d\eta \tag{C.3}$$

Shape Parameters

$$H = \frac{\delta^*}{\theta} \tag{C.4}$$

$$H^* = \frac{E}{\theta} \tag{C.5}$$

$$H_k = H \tag{C.6}$$

Kinetic Energy Shape Parameter

Laminar

$$H^* = \begin{cases} 0.0111\frac{(H_k-4.35)^2}{H_k+1.0} - 0.0278\frac{(H_k-4.35)^3}{H_k+1.0} + 1.528 - 0.0002\left[(H_k - 4.35)\,H_k\right]^2 & \text{if } H_k < 4.35 \\ 0.015\frac{(H_k-4.35)^2}{H_k+1.0} + 1.528 & \text{if } H_k \geq 4.35 \end{cases} \tag{C.7}$$

turbulent

$$
\begin{aligned}
H_0 &= \min\left(3.0 + \frac{400.0}{Re_\theta}, 4.0\right) \\
H_r &= \frac{H_0-H}{H_0-1.0} \\
H^* &= \begin{cases} \left(0.5 - \frac{4.0}{Re_\theta}\right)H_r^2\frac{1.5}{H+0.5} + 1.5 + \frac{4.0}{Re_\theta} & H < H_0 \\ (H - H_0)^2\left[0.007\frac{\log(Re_\theta)}{H-H_0+\frac{4.0}{\log(Re_\theta)}} + \frac{0.015}{H}\right] + 1.5 + \frac{4.0}{Re_\theta} & H \geq H_0 \end{cases}
\end{aligned} \tag{C.8}
$$

Boundary Layer Thickness estimate for Lag Equation

$$\delta = \left(3.15 + \frac{1.72}{H - 1.0}\right)\theta + \delta^* \tag{C.9}$$

Equilibrium Shear Stress Coefficient

$$
\begin{aligned}
C_0 &= \frac{0.5}{6.7^2 + 0.75} \\
U_s &= 0.5H^*\left(1.0 - \frac{h - 1.0}{0.75}\right) \quad \text{streamwise slip velocity} \\
C_\tau^{1/2} &= \sqrt{\frac{C_0 H^*\left(H - 1.0\right)^3}{(1.0 - U_s)\,H^3}}
\end{aligned} \tag{C.10}
$$

Skin Friction

laminar

$$C_f = \begin{cases} \frac{1}{Re_\theta}\left(0.0727\frac{(5.5-H)^3}{H+1.0} - 0.07\right) & H < 5.5 \\ \frac{1}{Re_\theta}\left[0.015\left(1.0 - \frac{1.0}{H-4.5} - 0.07\right)\right] & H \geq 5.5 \end{cases} \tag{C.11}$$

turbulent

$$\begin{aligned} C_{f0} &= 0.3\exp(-1.33H)\left(\frac{\log(Re_\theta)}{2.3026}\right)^{1.74-0.31H} \\ C_{f1} &= C_{f0} + 0.00011\left[\tanh\left(4.0 - \frac{H}{0.875}\right) - 1.0\right] \end{aligned} \tag{C.12}$$

Dissipation Wall Layer

$$C_D = C_{Dw} + \Delta C_{Dw} \tag{C.13}$$

laminar

$$\begin{aligned} D_1 &= \begin{cases} \frac{1}{Re_\theta}\left[0.207 + 0.00205\left(4.0 - H\right)^{5.5}\right] & H < 4.0 \\ \frac{1}{Re_\theta}\left[0.207 + 0.0016\frac{(H-4.0)^2}{1.0+0.2(H-4.0)^2}\right] & H \geq 4.0 \end{cases} \\ C_{Dw} &= \tfrac{1}{2}H^*D_1 \end{aligned} \tag{C.14}$$

turbulent

$$C_{Dw} = \frac{1}{2}C_f U_s \tag{C.15}$$

wake

$$\begin{aligned} \Delta C_{Dw} &= \int \tau\frac{\partial u}{\partial \eta}d\eta \\ &= C_\tau\left(1.0 - U_s\right) \end{aligned} \tag{C.16}$$

Bibliography

[1] C. W. Boppe, B. S. Rosen, J. P. Laiosa, and B. Chance Jr. *Stars and Stripes '87: Computational flow simulations for hydrodynamic design.* In *The Eighth Chesapeake Sailing Yacht Symposium*, Annapolis, MD, 1987.

[2] C. Cairoli. Analysis of the IMS velocity prediction program. Master's thesis, Massachusetts Institute of Technology, Department of Ocean Engineering, February 2002.

[3] A. Claughton. Developments in the IMS VPP formulations. In *Proceedings*, 14th Chesapeake Sailing Yacht Symposium. Society of Naval Architects and Marine Engineers, 1997.

[4] New York Yacht Club. Quote from the website. http://www.nyyc.org/AA_HTML_NEW/Olin_Stephens_profile_ACJ.html.

[5] C. W. Dawson. A practical computer method for solving ship-wave problems. *2nd International Conference on Numerical Ship Hydrodynamics*, 1977.

[6] M. Drela. *XFOIL: An Analysis and Design System for Low Reynolds Number Airfoils.*, volume 54 of *Low reynold Number Aerodynamics*. Springer-Verlag, New York, NY, 1989.

[7] M. Drela. Private conversation, 2005. Terry J. Kohler Professor of Fluid Dynamics, Dept. of Aeronautics and Astronautics, Massachusetts Institute of Technology.

[8] G. E. Gadd. A method for computing the flow and surface wave pattern around hull full forms. In *Transactions*, London, UK, 1976. Royal Institution of Naval Architects.

[9] J. Green, D. Weeks, and J. Brooman. Prediction of turbulent boundary layer and wakes in compressible flow by a lag-entrainment method. *R & M 3791*, 1977.

[10] G. S. Hufford. Viscous flow around propellers using boundary layer strip theory. Master's thesis, Massachusetts Institute of Technology, Department of Aeronautics and Astronautics, June 1992.

[11] J. Katz and A. Plotkin. *Low-Speed Aerodynamics*. Cambridge University Press, Cambridge, United Kingdom, second edition, 2001.

[12] J. E. Kerwin. Introduction to geometric modeling and computation. Lecture notes, Massachusetts Institute of Technology, 1994.

[13] D. C. Kring. *Time Domain Ship Motions by a Three-Dimensional Rankine Panel Method.* PhD dissertation, Massachusetts Institute of Technology, Department of Ocean Engineering, May 1994.

[14] M. M. D. Levadou, H. J. Prins, and H. C. Raven. Application of advanced computational fluid dynamics in yacht design. In *Proceedings*, HISWA, Delft, Netherlands, 1998.

[15] W. M. Milewski. *Three-Dimensional Viscous Flow Computations Using Integral Boundary Layer Equations Simultaneously Coupled with a Low Order Panel Method.* PhD dissertation, Massachusetts Institute of Technology, Department of Ocean Engineering, June 1997.

[16] B. H. Mughal. A calculation method for the three-dimensional boundary layer equations in integral form. Master's thesis, Massachusetts Institute of Technology, Department of Aeronautics and Astronautics, September 1992.

[17] D. E. Nakos and P. D. Sclavounos. Steady and unsteady ship wave patterns. *Journal of Fluid Mechanics*, 215, 1990.

[18] D. E. Nakos and P. D. Sclavounos. Kelvin wakes and wave resistance of cruiser- and transom-stern ships. *Journal of ship Research*, 38:9–29, March 1994.

[19] J. N. Newman. *Marine Hydrodynamics*. MIT Press, Cambridge, MA, 1977.

[20] J. N. Newman. Distribution of sources and normal dipoles over quadrilateral panels. *Journal of Engineering Mathematics*, 20:113–126, 1986.

[21] B. A. Nishida. *Fully Simultaneous Coupling of the Full Potential Equation and the Integral Boundary Layer Equations in Three Dimension.* PhD dissertation, Massachusetts Institute of Technology, Department of Aeronautics and Astronautics, February 1996.

[22] N. H. Norrbin. A panel method for lifting potential flows around three-dimensional surface piercing bodies. In *Proceedings*, 17th international Towing Tank Conference, Goteborg, Sweden, 1984.

[23] National Institute of Standards and Technology. The IGES project. www.nist.gov/iges.

[24] H. C. Raven. *A solution Method for the Nonlinear Ship Wave Resistance Problem.* PhD dissertation, Technische Universiteit Delft, Department of Naval Architecture, June 1996.

[25] D. F. Rogers. *An Introduction to NURBS: with hystorical perspective.* Morgan Kaufmann Publishers Co., San Francisco, CA, xvii edition, 2001.

[26] B. S. Rosen, J. P. Laiosa, W. H. Davis, and D. Stavetski. SPLASH free-surface flow code methodology for hydrodynamic design and analysis of IACC yachts. In *The Eleventh Chesapeake Sailing Yacht Symposium*, Annapolis, MD, 1993.

[27] B. S. Rosen, J. P. Laiosa, and W. H. Warren. CFD design studies for America's Cup 2000. *AIAA Paper 2000-4339*, 2000.

[28] P. D. Sclavounos. Private conversation, 2006. Professor of Mechanical Engineering and Naval Architecture, Dept. of Mechanical Engineering, Massachusetts Institute of Technology.

[29] P. D. Sclavounos and D. E. Nakos. Stability analysis of panel methods for free-surface flows with forward speed. In *Proceedings*, 17th Symposium on Naval Hydrodynamics, Den Hague, Netherlands, 1988.

[30] F. M. White. *Viscous Fluid Flow*. McGraw-Hill Book Co., New York, NY, 1991.

[31] J. Windt and H. C. Raven. A composite procedure for ship viscous flow with free surface. In *Proceedings*, 3rd Numerical Towing Tank Symposium, Tjarno, Sweden, 2000.

[32] Z. J. Zou and H. Söding. A panel method for lifting potential flows around three-dimensional surface piercing bodies. In *Proceedings*, 20th Symposium on Naval Hydrodynamics, pages 810–821, Santa Barbara, CA, 1994.